Fundamental Mechanism of THz Radiation from High-Temperature Superconductor $Bi_2Sr_2CaCu_2O_{8+\delta}$ and its Device Applications

Manabu Tsujimoto

February 2013

Fundamental Mechanism of THz Radiation from High-Temperature Superconductor $Bi_2Sr_2CaCu_2O_{8+\delta}$ and its Device Applications

Manabu Tsujimoto
Doctoral Program in Materials Science

Submitted to the Graduate School of
Pure and Applied Sciences
in Partial Fulfillment of the Requirements
for the Degree of Doctor of Philosophy in
Engineering

at the
University of Tsukuba

Contents

Chapter 1

Introduction

The intrinsic Josephson effect as a tunnelling of Cooper pairs between adjacent CuO_2 layers inside the highly anisotropic high-temperature superconductor has attracted much experimental and theoretical attention since the first experimental observation in 1992 [1]: In the c-axis (*i.e.*, perpendicular direction to the CuO_2 layer) current-voltage characteristics of $Bi_2Sr_2CaCu_2O_{8+\delta}$, we can see a number of quasiparticle branches that correspond to the individual switching of the intrinsic Josephson junction naturally formed in the crystal structure. This rather surprising consequence leads one to a new materially concept of the high-temperature superconductor as a stack of superconductor-insulator-superconductor Josephson junctions. This has made a considerable influence on the concept of the high-temperature superconductivity because it has revealed that the superconducting order parameter of the high-temperature cuprate superconductor is spatially modulated in the c-axis direction with a period of half the c-axis length. It is worthwhile mentioning here that a couple of good review articles on the intrinsic Josephson effect and on the present status of research regarding theoretical understanding have been published [2–4].

In 2007, Ozyuzer *et al.* successfully observed electromagnetic wave radiation from a stack of intrinsic Josephson junctions in single-crystalline $Bi_2Sr_2CaCu_2O_{8+\delta}$ with remarkably high intensity [5]. Since early times, the superconducting electrical circuit based on the Josephson junction has been considered to be a potential candidate of the sub-millimeter radiation source. The important point is that the observed radiation frequency fortuitously ranges in even the sub-THz region, which is still unexplored because of the lack of compact and convenient radiation sources [6]. Therefore, a great deal of interest has been drawn not only to the physical mechanism of the THz radiation but also to the possible variety of practical applications. The possible principle of the radiation based on the intrinsic Josephson effect is quite unique because the high-frequency Josephson plasma oscillation is derived from the quantum interference of the superconducting order parameter.

In this thesis, the author describes a study of the fundamental mechanism of THz radiation from the high-temperature superconductor $Bi_2Sr_2CaCu_2O_{8+\delta}$ and its device applications, which has been performed in the Doctoral Program in the Graduate School of Pure and Applied Sciences at the University of Tsukuba. Some research outcomes have been

published in scientific journals [7–11]. Also, the author contributed to the preparation of two review articles [12, 13] and other papers [14–18]. The content of this thesis is in the following:

Chapter 2 Research backgrounds on the experimental observation of THz radiation from intrinsic Josephson junctions in $Bi_2Sr_2CaCu_2O_{8+\delta}$ will be given. Starting from the introduction to the fundamental characteristics of the radiation, both the Josephson effect and the cavity resonance effect that triggers the intense radiation will be presented. At the end, the recent research topics on the frequency tunability and on the thermal non-equilibrium state will be introduced.

Chapter 3 In this chapter, the technical issues of the individual experiment; single crystal growth of $Bi_2Sr_2CaCu_2O_{8+\delta}$, microfabrication technique for the sample preparation, measurement setup, *etc.*, will be described.

Chapter 4 The author will focus on the discussion of the cavity resonance effect on the radiation from various geometrical mesa shapes. First, some theoretical formulations of the cavity resonance conditions will be derived from microstrip antenna theory. Then, the experimental results and discussion will be presented in sequence. Some new analytical methods for analyzing the spatial radiation pattern will be introduced.

Chapter 5 In this chapter, the author will investigate the THz radiation which takes place in the inner region of the multiply-branched current-voltage characteristics, where the number of active junctions is fixed but different for each branch. The author will show clear evidence that the mesas can emit radiation at many frequencies without strong interaction with an internal electromagnetic cavity resonance. Such a broadband tunability of the radiation frequency comes from the variation of the resistive states unique to the weakly-coupled intrinsic junction system. More importantly, the resulting radiation is considerably tunable over a broad range of frequencies, allowing for the construction of a powerful device that could fill the terahertz gap.

Chapter 6 THz imaging experiments using high-temperature superconducting THz source devices will be demonstrated as a potential application of the present device. As test examples, THz images of various objects (metal, paper, plastic, *etc.*) will be presented. Using a handmade interferometer quartz cell, we can investigate the interference patters to calibrate the radiation frequency. Also, by filling liquid samples into the cell and measuring the sample thickness dependence of the transmittance of the THz wave, the absorption coefficients of liquids can be measured with high accuracy.

Chapter 7 The author will summarize this thesis in this chapter.

Chapter 2

Backgrounds

2.1 Emission of coherent THz radiation

Fundamental characteristics

In 2007, Ozyuzer *et al.* demonstrated that coherent, intense, and continuous terahertz (THz) wave radiation can be extracted from intrinsic Josephson junctions [1] in the layered high transition temperature (T_c) superconductor $Bi_2Sr_2CaCu_2O_{8+\delta}$(Bi-2212) [5]. As Josephson predicted in 1962 [19], a conventional Josephson junction with two superconducting electrodes separated by a thin insulating layer naturally converts DC voltage, V, across the junction into electromagnetic radiation at the Josephson frequency, f_J, where f_J can be expressed by the following well-known Josephson relation [19]:

$$f_J = \frac{2e}{h}V, \tag{2.1}$$

with 1 mV corresponding to 0.4835979 THz. Although the high-frequency radiation from a single junction is very weak, it has been demonstrated that a huge number of junctions can possibly produce the electromagnetic wave at the same frequency with sufficient power [20–22]. On the other hand, Kleiner *et al.* discovered a natural stack of Josephson junctions with unsurpassed packing density in the layered high-T_c superconductor Bi-2212 in 1992 [1]. This compound, composed of superconducting CuO_2 double layers that are coupled through the intrinsic Josephson effect, can sustain high voltages across the junctions and holds the potential for intense radiation at the THz frequency region [23–25]. However, the key requirement for producing useful radiation from Bi-2212 has so far been a major challenge preventing the realization of this potential. Many approaches for synchronizing the intrinsic junctions have been proposed, such as applying a magnetic field to induce coherent Josephson vortex flow [26–31], or inserting the Bi-2212 crystal into a microwave cavity [32]. Nevertheless, the radiation power limited up to the pW range for over ten years [33].

In the paper by Ozyuzer *et al.* [5], the authors reported in their findings that THz radiation in the µW range can be produced by a standing electromagnetic wave that is formed by multiple reflections in the mesa structure shown in Fig. 2.1(a). Figure 2.1(b) shows the
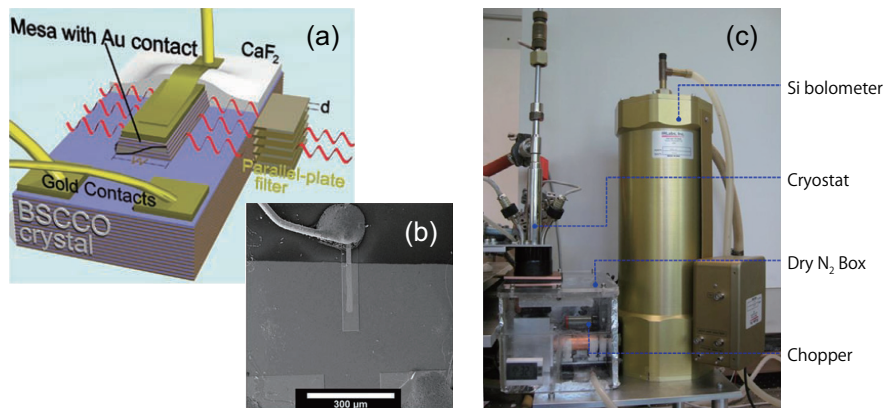
Figure 2.1: (a) Schematic view of the Bi-2212 mesa. (b) Scanning electron microscopy image of the mesa. (c) Experimental setup. (copied from [5, 37])
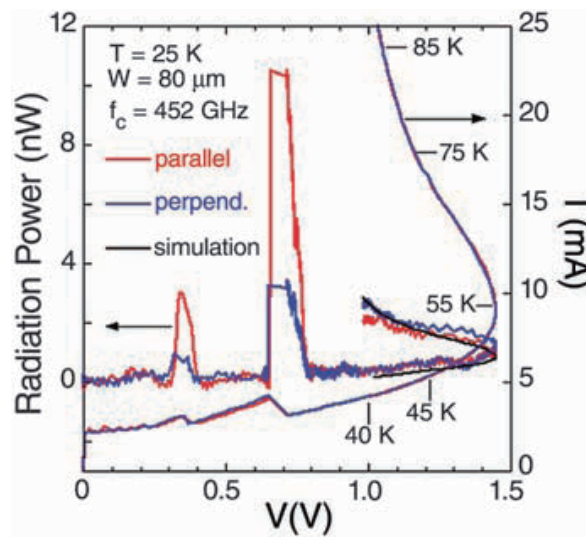

Figure 2.2: *I-V* characteristics and radiation intensity of the 80-µm mesa. (copied from [5])

scanning electron microscopy image of the mesa structure. In Fig. 2.1(c), the experimental setup including a sample-in-vacuum continuous flow cryostat, chopper, and Si bolometer, is presented. Figure 2.2 shows the current-voltage (I-V) characteristics and the radiation intensity detected by the Si bolometer. Both quantities are recorded simultaneously as a function of decreasing bias voltage for the parallel and perpendicular settings of a parallel-plate cut-off filter. We can see a couple of polarized radiation peaks near 0.37 V and 0.71 V, whose electric field is polarized perpendicularly to the CuO_2-planes, and can see unpolarized radiation in the high current region. The former is identified as Josephson radiation, whereas the latter is thermal radiation. The radiation power was estimated to be around 11 nW, which is more than 10^4 times as large as that which has been obtained previously [33].

An estimation of the radiation frequency f was given by the filter cut-off frequency and by far-infrared spectra as shown in Fig. 2.3. Both methods yield consistent results; namely, $f = 0.36$, 0.48, 0.59, and 0.85 THz for the 100-µm, 80-µm, 60-µm, and 40-µm wide mesas, respectively. As shown in the inset of Fig. 2.3, the observed frequencies are in good agreement with the fundamental cavity resonance frequency f_{10}^r given in the form:

$$f_{10}^r = \frac{c_0}{2nw},\tag{2.2}$$

where c_0 is speed of light in vacuum, w the width of the mesa, and $n \sim 3.5$ the c-axis far-infrared refractive index of Bi-2212 [34]. Then, the radiation power builds up as f_J comes into f_{10}^r with the bias current scan in the fully resistive state. Then, with decreasing V, some junctions may switch back from the resistive state to the zero-voltage state [35]. During such a jump, both V per active junction and f_J increase to satisfy the Josephson relation (2.1). Consequently, the system falls to match the cavity resonance, and then radiation stops. With further decreasing bias current, the resonance condition may be fulfilled again, yielding a radiation peak involving a smaller number of active junctions.

Figures 2.4(a) and 2.4(b) show a sequence of radiation peaks for positive and negative bias voltage on the 80-µm mesa and for the number of active junctions $n_{\rm rel}$, respectively, where $n_{\rm rel}$ can be determined directly from the resistance corresponding to the various quasiparticle branches shown in the I-V characteristics. As shown clearly, the observed radiation powers are proportional to $n_{\rm rel}^2$, demonstrating that the active junctions in the stack produce THz waves coherently. In their paper, the authors claimed that the cavity resonances that occur on the long dimension of the mesa do not contribute to the radiation because they incur sign changes of the electric field in the long side faces, and that the coherent superposition of the electromagnetic waves from each junction creates a microscopic coherent state in which the radiation power increases as the square of the number of active junctions.

After the first publication of THz radiation from Bi-2212, a couple of research groups individually revealed the fundamental characteristics of the radiation mostly from rectangular Bi-2212 mesas in more detail [14, 16, 36–41]. A huge number of theoretical studies have also been conducted to understand the mechanism of the radiation [15, 42–72], although in this thesis we do not go into all works in detail because of space limitations.

Kurter *et al.* presented a thermal analysis of the radiating Bi-2212 mesa in order to

investigate the accessible bias conditions for the radiation [39]. They estimated the average mesa temperature by equating the quasiparticle resistance to the ratio V/I over the entire I-V characteristic curve including the backbending region. Meanwhile, Minami *et al.* reported the total radiation power up to 5µW by considering both the anisotropic spatial radiation pattern and the detector sensitivity [40]. They also measured far-infrared radiation spectra by using the Fourier transform infrared (FT-IR) spectrometer and revealed that the emitted THz wave is linearly polarized with a polarization ratio of 50:1. It should be noted here that, in some cases, the higher harmonic radiation up to the fourth order was clearly distinguished from the fundamental one [36]. Kadowaki *et al.* pointed out the dual source mechanism [15, 59,60] in which the uniform and non-uniform parts of the AC Josephson current act as electric and magnetic current sources, respectively [14]. To obtain the relative amplitude and phase of these two sources, they investigated anisotropic radiation patterns from rectangular mesas in both the E and H planes.

Cavity resonance effect

According to the microstrip antenna theory, the cavity resonance frequencies for the rectangular transverse magnetic (TM) modes can be expressed in the form:

$$f_{mp}^r = \frac{c_0}{2n}\sqrt{\left(\frac{m\pi}{w}\right)^2 + \left(\frac{p\pi}{\ell}\right)^2}, \tag{2.3}$$

where m and p are integers, and w and ℓ denote the width and the length of the rectangular microstrip antenna, respectively. The geometrical cavity resonance conditions given by Eq.(2.3) for intense radiation will be discussed in detail in a later chapter. For the fundamental TM(1, 0) mode, Eq. (2.3) reduces to Eq. (2.2) with $m = 1$ and $p = 0$. In fact, as presented in the inset of Fig. 2.3, in all previous studies, a rectangular TM(1, 0) mode has been observed as a fundamental cavity mode with $f = f_{10}^r$, suggesting that the half-wavelength electromagnetic standing wave with $\lambda/2 = w$ is formed inside the mesa cavity.

With this background, Kashiwagi *et al.* have pointed out the possible excitation of the higher-order cavity resonance [12,17]. Figure 2.5(a) shows the scanning ion microscopy image of the rectangular mesa with a size of $80 \times 320 \times 1.6$ µm³, while Fig. 2.5(b) shows the cross-sectional profile curve along line A–A' indicated in Fig. 2.5(a). Note that the fabricated mesa has a non-ideal shape due to some accidental fabrication processes. Figure 2.5(c) shows the outermost I-V characteristic curve (left scale) together with the detected radiation intensity (right scale), while Fig. 2.5(d) shows FT-IR radiation spectra measured at bias points A (1.29 V) and B (0 V) indicated in Fig. 2.5(c) with different backgrounds for clarity. In Figs. 2.5(c) and 2.5(d), we can clearly see intense radiation peak at A at $f = 0.922$ THz, which is just twice as large as the value predicted from Eq. (2.2) for a 80-µm wide mesa. This can be naturally explained by the unexpected excitation of the rectangular TM(2, 0) mode, as is described by Eq. (2.3) with $m = 2$ and $p = 0$. Although the voltage at which the TM(1, 0) mode radiation takes place is calculated as 0.63 V from Eq. (2.1), however, the obtained I-V curve shown in Fig. 2.5(c) can never reach this voltage. This is consistent
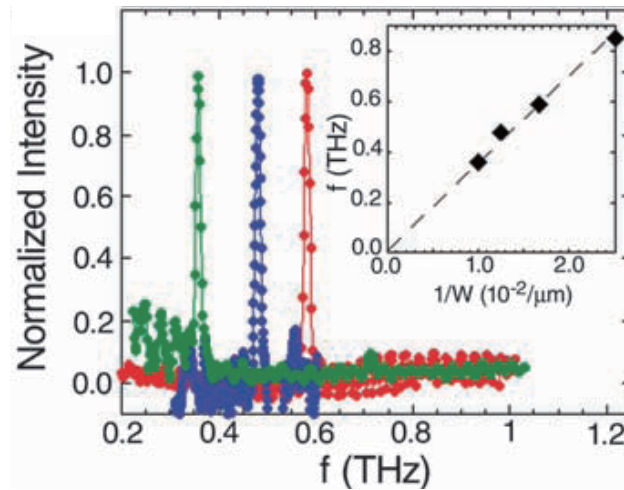
Figure 2.3: Far-infrared radiation spectra from 60-µm (red), 80-µm (blue), 100-µm (green) wide mesas. (copied from [5])
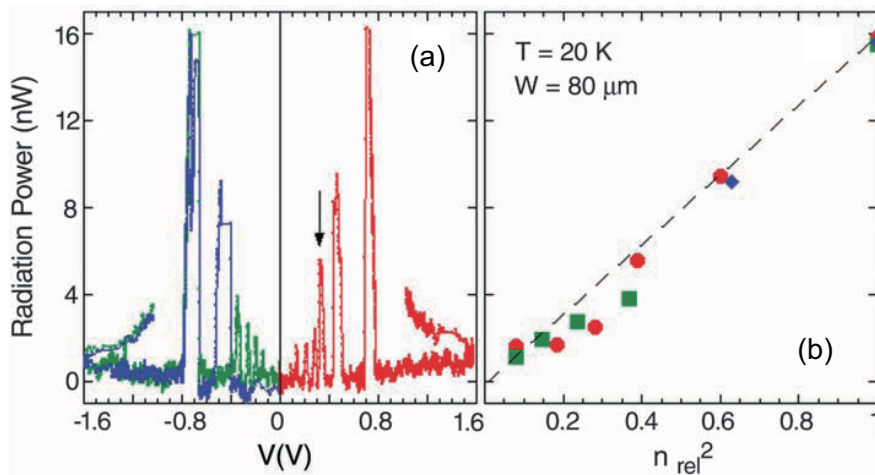

Figure 2.4: (a) Sequence of radiation peaks acquired on successive voltage scans. (b) Radiation intensity in the peaks as a function of n_{rel}^2. (copied from [5])

with the resonance condition of $f^r_{mp} = f_J$, suggesting that higher-order cavity modes other than TM(1, 0) and TM(2, 0) modes would also be excited if we could apply a suitable V to the mesa.

In order to further investigate the TM(2, 0) mode radiation, the authors measured the spatial radiation pattern from a 80-µm wide radiating mesa. Figure 2.6 shows the detection angular (θ) dependence of the radiation intensity [17]. Suppose the radiation comes from the TM(2, 0) cavity resonance, the original radiation pattern E_θ in the E plane can be expressed in the form:

$$E_\theta \propto \sin \left(k_0 \frac{w}{2} \sin \theta \right),\tag{2.4}$$

with $k_0 = 2\pi f/c_0$. Detailed descriptions of radiation patterns will be presented in a later chapter. The characteristic features of $|E_\theta|^2$ are as follows: The intensity in the vicinity of $\theta = 0°$ is zero, whereas it reaches a maximum at $\theta = 90°$. In Fig. 2.6, dashed and solid lines represent calculation results for $|E_\theta|^2$ and $|E_\theta \cos \theta|^2$, respectively, where a factor of $\cos \theta$ represents the effect of the superconducting Bi-2212 substrate [59]. As clearly shown in Fig. 2.6, calculated $|E_\theta \cos \theta|^2$ is in good agreement with the experimental result except for the region at $\theta \sim \pm 45°$, although the authors did not refer to this discrepancy in the theory and the experiment.

2.2   Recent topics

Frequency tunability

Recently, Wang *et al.* and Benseman *et al.* individually demonstrated that the radiation frequency can be varied by up to $\pm 20\%$ by changing bias current and bath temperature [73, 74], although the origin of such tunability is still not well understood. Figures 2.7(a) and 2.7(b) show the FT-IR radiation spectra measured at a range of bias voltage obtained from a $80 \times 300 \times 1$-µm^3 rectangular mesa [74] at bath temperatures $T = 20$ K and 30 K, respectively. With increasing T, the radiation band shifts to lower frequencies, which is consistent with other experimental results regarding $f(T)$ [73]. The envelope of the radiation peaks at each T tracks well the voltage dependence of the total radiation intensity separately measured by using the Si bolometer. Two arrows shown in Figs. 2.7(a) and 2.7(b) indicate the average frequencies used in Fig. 2.7(c).

Since electromagnetic waves in strongly layered superconductors such as Bi-2212 exist as Josephson plasma waves, N intrinsic junctions are expected to produce N different plasma modes for fixed in-plane wave vector k. The dispersion relation for such plasma modes is given by $\omega^2 = \omega^2_{pl} + c^2 k^2$, with $c^2 = c^2_0/\varepsilon_c \{2(1 - \cos(qs))\lambda^2_{ab}/s^2 + 1\}$. Here, q is the wave vector perpendicular to the CuO$_2$ planes that indexes each possible plasma mode, and $\omega_{pl} = c_0/\lambda_c\sqrt{\varepsilon_c}$ is the Josephson plasma frequency, which is on the order of $\sim$70 GHz. ε_c is the c-axis far-infrared dielectric constant of Bi-2212, λ_c and λ_{ab} the c-axis and ab-plane London penetration depths, respectively, and $s \sim 1.5$ nm the repeat distance of the CuO$_2$
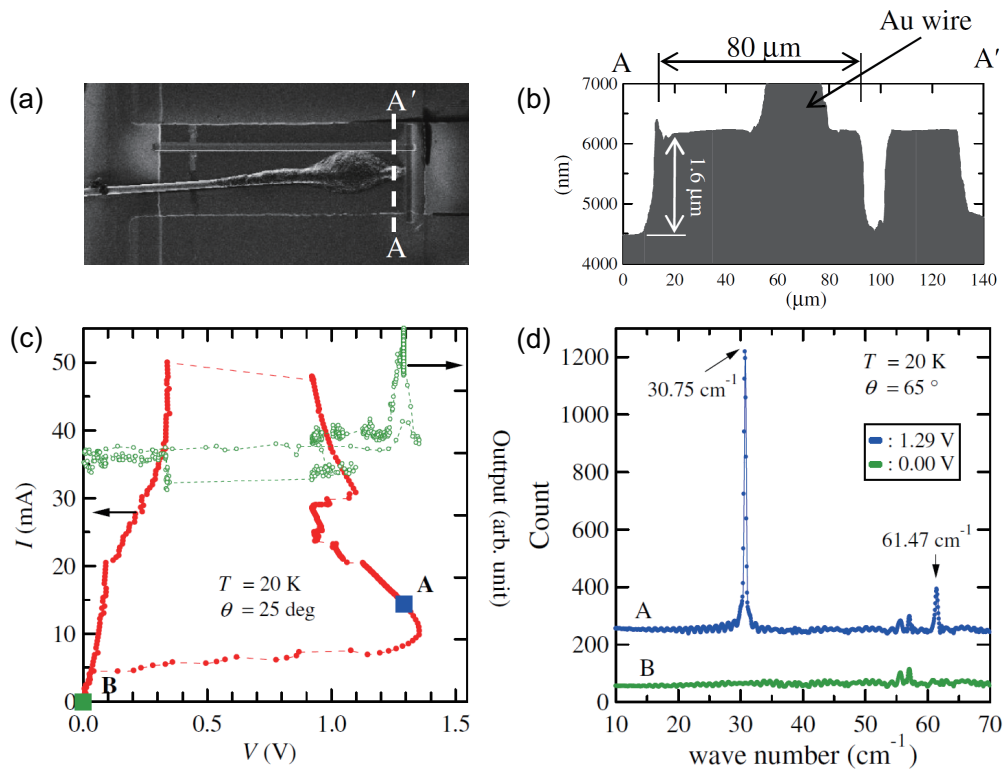
Figure 2.5: (a) Scanning ion microscopy image of the mesa. (b) Cross-sectional profile curve along line A–A' indicated in Fig. 2.5(a). (c) *I-V* characteristics and radiation intensity. (d) Far-infrared radiation spectra measured at bias points A and B indicated in Fig. 2.5(c). (copied from [17])
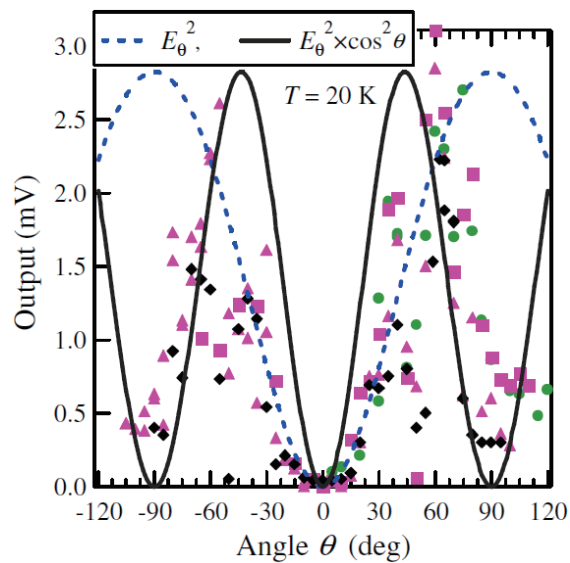

Figure 2.6: θ dependence of the radiation intensity. The different symbols indicate the data points taken by different runs. (copied from [17])

double layers in Bi-2212. In the resistive state, since the plasma gap (ω_{pl}) is suppressed to zero, the plasma mode that is uniform along the c-axis with $q = 0$ can be excited, producing in-plane oscillations of the electric field for all junctions. In this case, the wave speed reduces to the temperature-independent value of $c = c_0/n$. This model is not, however, sufficient to explain measured $f(T)$ shown in Figs. 2.7(a) and 2.7(b).

Figure 2.7(c) presents the measured T dependence of the average radiation frequency. Benseman *et al.* assumed that this peculiar $f(T)$ arises from the asymmetric geometry of the actual mesa [74]. They pointed out two asymmetric boundaries of the mesa: (1) the non-vertical side walls and (2) different boundary conditions at the top and bottom of the mesa. The allowed values of q are determined by the boundary conditions at the top and bottom surfaces of the mesa: Namely, in the present case, the lowest-order modes would have $q = \pi m/2t$, with $m = 1, 3 \cdots$. Hence, the dispersion relation of the Josephson plasma waves can yield a T-dependent wave speed of $c^2 = c_0^2/\varepsilon_c\{1 + (m\pi\lambda_{ab}/2t)^2\}$ and therefore a T-dependent frequency of $f^2 = f_0^2/\varepsilon_c\{1 + (m\pi\lambda_{ab}/2t)^2\}$. In Fig. 2.7(c), the expected $f(T)$ determined by scaling the data for λ_{ab} for the sample with a doping level δ of 0.124 by a factor 1.5, giving $\lambda_{ab}(0) \approx 550$ nm. As clearly shown, as the penetration depth increases with increasing temperature, the frequency decreases. Such a T dependence of λ_{ab} has been determined from microwave cavity measurements for optimally-doped Bi-2212 [75] and AC susceptibility measurements on powder samples with various doping levels [76]. The experimental result is well described by the variation of the $m = 1$ mode, whereas the data are also consistent with $m = 3, 5$ modes requiring unexpectedly small values of λ_{ab} to match the measured $f(T)$.

Thermal non-equilibrium state

As presented in Fig. 2.2, most workers have so far observed THz radiation in relatively lower current regions, where some part of the intrinsic junctions switch into the zero-voltage state. In this region with moderate DC input power, typically below 1 mW, since there is no severe self-heating of the mesa, the mechanism of the THz radiation should be described by the standard physics and electrodynamics of the Josephson junction. On the other hand, in some cases, we can also see the intense radiation in the high current region, where self-heating is inevitably severe because of the high DC input power of more than tens of milliwatts [73, 77]. It is worthwhile to mention that, in the high bias region, the resistive state is very stable and even reversible with the bias current scan, enabling us to tune the radiation frequency on the basis of the Josephson effect. By contrast, in the low current region, some of the intrinsic junctions can individually switch from the resistive state to the zero-voltage state, causing unstable jumps in the I-V characteristics.

In order to investigate the thermal non-equilibrium state of the radiating mesa, Wang *et al.* have measured the inhomogeneous spatial distribution of the mesa temperature by using the low-temperature scanning laser microscopy (LTSLM), and have succeeded in observing a hot spot region, which is a local region heated to a temperature T that can even exceed
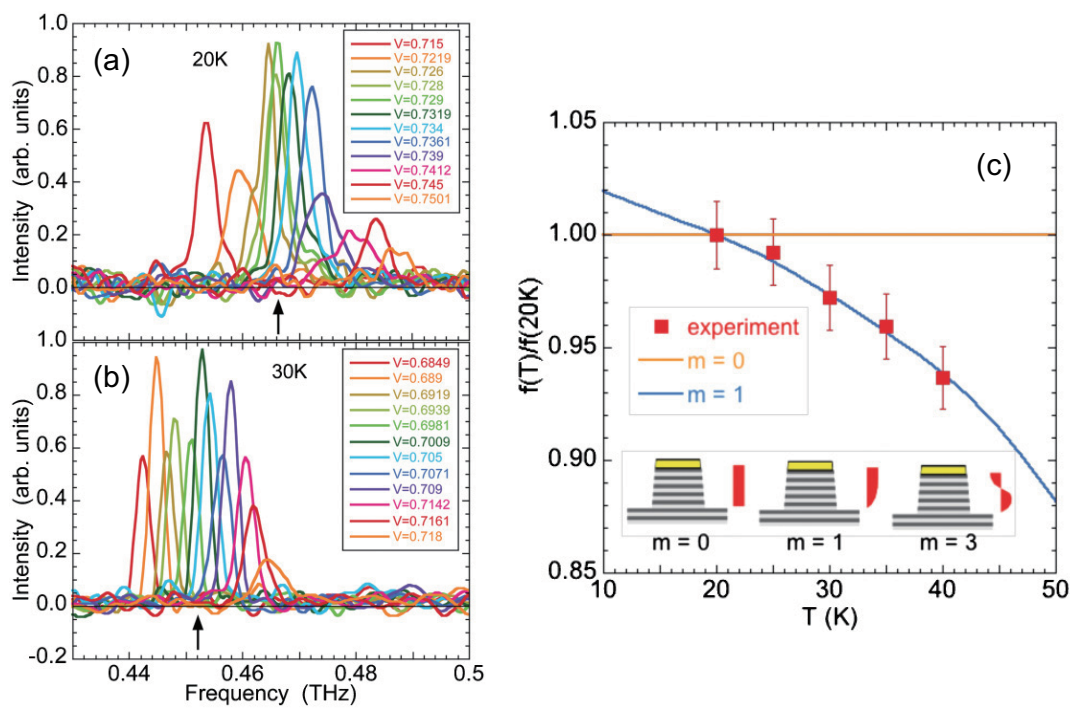
Figure 2.7: FT-IR radiation spectra taken at a range of mesa voltage V at (a) $T = 20$ K and (b) $T = 30$ K. (c) T dependence of the average radiation frequencies (red squares) and of the calculated radiation frequencies of the $m = 0$ and $m = 1$ modes. The inset shows schematics of the c-axis dependence of the cavity mode. (copied from [74])

T_c [78]. Figure 2.8 presents the principle of LTSLM: The beam from a diode laser is deflected and focussed onto the mesa surface. The spot size is typically 1–2 µm. Then, local heating by a few K causes a response ΔV serving as the contrast for the LTSLM image. In order to improve the signal-to-noise ratio, the laser beam is modulated at 10–80 kHz, so that ΔV can be detected by a lock-in amplifier. The local temperature in the cold region was roughly estimated to be in the order of 50–70 K, which is much higher than the bath temperature T because of self-heating.

Figure 2.9 shows the *I-V* characteristic at 50 K together with LTSLM images obtained from a 30 µm wide rectangular mesa. Red solid arrows on the left panel in Fig. 2.9 denote the switching process, while black arrows in the center indicate nine bias points at which LTSLM images A–K have been taken. At $I < 16$ mA, the LTSLM images show a broad response, being strongest near the contact electrode (cf. image A), whereas slightly above 16 mA, two bright stripes appear right of the contact electrode (cf. image B). With further increasing I, these two stripes move away from each other until 22 mA (cf. Image E): The right stripe joins the edge signal, while the left stripe continues to move toward the left mesa edge. The feature seen here is very indicative of a hot spot, as observed for superconducting thin-film microbridges [79]. Such hot spots under the influence of the in-plane current flow have also been imaged by LTSLM [80, 81].

Recently, simultaneous observation of LTSLM images and THz radiation has been successfully performed [73, 82]. As an important result, the authors succeeded in observing a series of peculiar standing wave patterns of the LTSLM signal from the rectangular, cylindrical disk, and arrow-shaped mesas in the high current region, pointing to the importance of cavity resonances for synchronization. Thus, they proposed a new mechanism that explains the frequency tunability: The hot spot allows one to vary the cavity resonance frequency by changing the mode velocity as well as the area of the cold part of the mesa. They also stressed that the considerably narrow spectral linewidth of the radiation arises from a novel independent synchronization mechanism based on the hot spot dynamics [83].

Meanwhile, Kakeya *et al.* claimed that the local temperature rise inside the mesa is a key phenomenon to induce the synchronization of the Josephson plasma oscillation [84]. They prepared and measured four mesas with different thicknesses of the electrode layer, so that the release of the Joule heat can be controlled. The intense radiation was then observed from mesas having a thickness less than 100 nm, in which remarkable temperature inhomogeneity is expected to occur. This suggests an intriguing possibility that the formation of the dynamical phase variation along the mesa edge (π-kink) yields intense radiation, as numerically simulated by some workers [44, 46, 54].
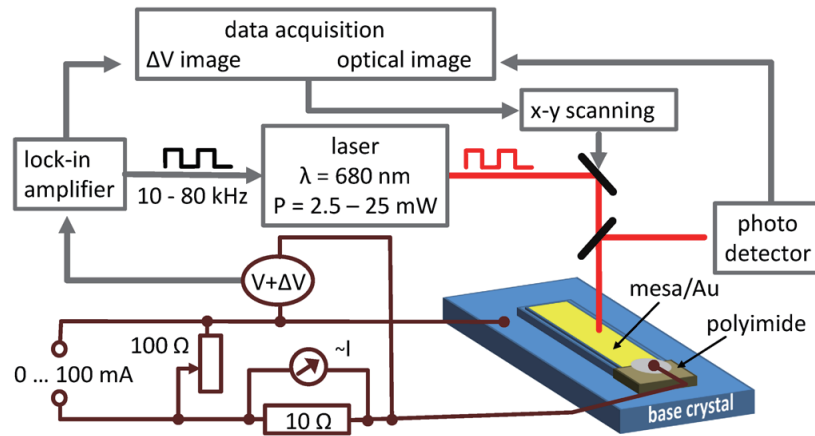
Figure 2.8: Principle of LTSLM. (copied from [78])
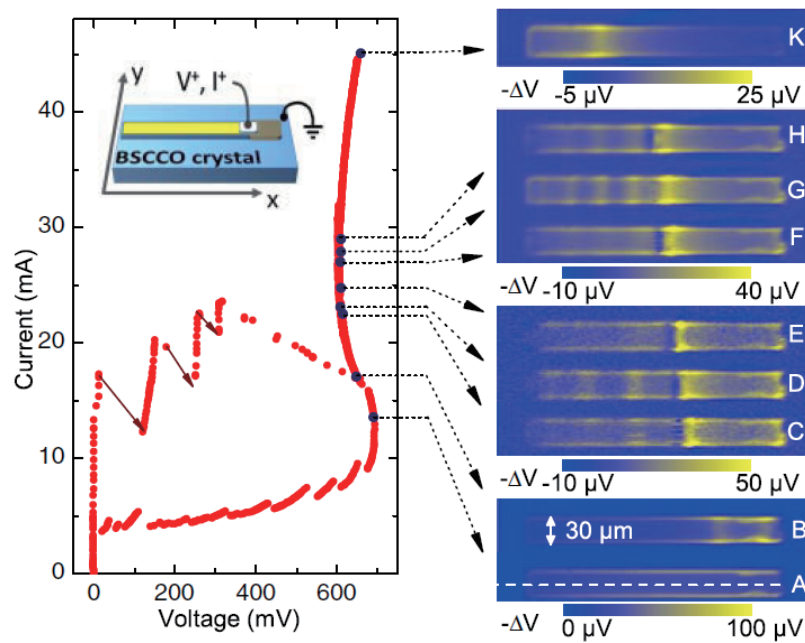
Figure 2.9: *I-V* characteristics and LTSLM data of a 30×330µm² mesa. (copied from [78])

Chapter 3

Experimental

3.1 Sample preparation

Single crystal growth of Bi$_2$Sr$_2$CaCu$_2$O$_{8+\delta}$

Single crystals of Bi$_2$Sr$_2$CaCu$_2$O$_{8+\delta}$ (Bi-2212) [85] used in this study have been prepared by a traveling solvent floating zone (TSFZ) technique [86] appropriate for growing incongruent melting materials, such as a series of high transition temperature (T_c) cuprate superconductors. The TSFZ technique has some advantages in comparison with other techniques, *e.g.*, top seeded solution growth, flux method, *etc.*, which are often used for growing the single crystalline oxides. For instance, the TSFZ method makes it possible to generate a spatially extreme thermal gradient to form the local melting zone. Also, since no container or crucible is used, high purity crystals can be obtained.

All single crystals of Bi-2212 were grown in air at the growth rate of 0.5–1.0 mm/h using an infrared convergence type floating zone furnace [87]. Figure 3.1(a) show the schematic view of the operation principle of the TSFZ technique, while Fig. 3.1(c) presents a photo of the mirror furnace. A molten zone forming between the crystal and the feed rod shown in Fig. 3.1(b) was placed at the center of the ellipsoidal mirrors, where the infrared light from two halogen lamps is focused as shown in Fig. 3.1(a). In order to achieve homogeneous heating and to promote the zone mixture, both crystal and feed rod were counter rotated. The single crystal of Bi-2212 then grows as they move down simultaneously. Figure 3.1(d) shows an as-grown single crystal boule of Bi-2212. We can easily cut and cleave the boule into thin slabs by using a knife and Scotch tape.

Before fabricating the sample, as-grown Bi-2212 crystals were annealed at 650°C for 24 hours in the tube furnace filled with argon gas and 0.1% oxygen in order to obtain the underdoped crystals. The superconducting transition temperature of 80–85 K is typical of slightly underdoped Bi-2212 [88], as discussed in detail later.
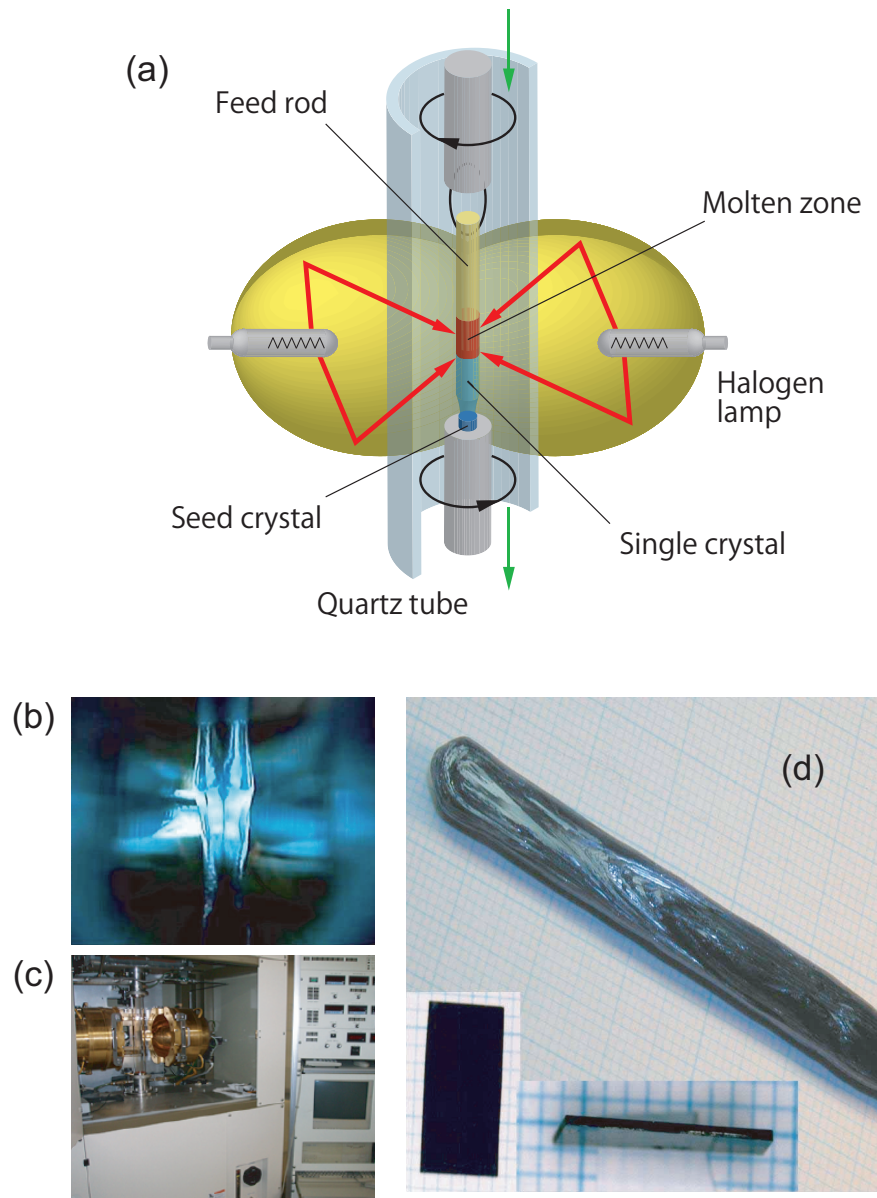
Figure 3.1: (a) Schematic view of the operation principle of the TSFZ technique. (b) Snapshot picture of the molten zone of Bi-2212. (c) A photo of the mirror furnace. (d) As-grown single crystalline Bi-2212 boule and two pieces of the cleaved single crystal.

Microfabrication technique

The samples used for the present studies were fabricated into mesas with various geometrical shapes by combining focused ion beam (FIB) milling and argon ion milling techniques. First, a piece of a cleaved Bi-2212 crystal ($1 \times 1 \times 0.01$ mm^3) was glued onto a sapphire substrate and silver and gold thin layers were evaporated onto it. Next, a thin mesa structure was fabricated onto the crystal surface by several microfabrication techniques. In this study, we attempted to make three types of samples: "groove type", "terrace type", and "stand-alone (SA) type", as presented in Figs. 3.2(a), 3.2(b), and 3.2(c), respectively.

For making a groove-type sample, a groove of width of 5–10 µm was patterned around the mesa by using the FIB milling technique. For the terrace-type sample, a conventional photolithography and an argon ion milling technique were used. The SA type sample was made by depositing a narrow gold strip on a single crystal, argon ion milling, and cleavage from the milled Bi-2212 substrate. Then, a thin gold layer was attached to the mesa. In all cases, as electrodes, thin gold wires 10 µm in diameter were finally fixed onto the top surface of these mesas and onto the underlying Bi-2212 substrate by using silver paste.

In order to fabricate the groove-type samples with various mesa shapes, we used the option "Bitmap Patterning" of the FIB milling system. This option is superior to other fabrication methods in easily designing the geometrical mesa shape. First, a black-and-white bitmap image was generated by using an image-editing software such as Adobe Illustrator. Figures 3.3(a), 3.3(b), and 3.3(c) show examples of the generated bitmap images of disk, square, and rectangular grooves. A 800×800-pixel bitmap image corresponds to the full-scale pattern in the present FIB system. The available patterning scales are as follows: 80 µm, 60 µm, 40 µm, 24 µm, 15 µm, 12 µm, 8 µm, 6 µm, *etc.* In this study, we used only the Mid FIB (1318 pA) with consideration for the required fabrication accuracy. Figures 3.4(a), 3.4(b), and 3.4(c) present the scanning ion microscope (SIM) images of disk, square, and rectangular mesas taken after the milling process. In the course of my Ph.D. work, 13 samples with different types, geometries, and dimensions as summarized in Table 3.1 have been prepared.

Figure 3.2: Schematic views of the Bi-2212 mesa samples: (a) groove-type, (b) terrace-type, and (c) stand-alone type.
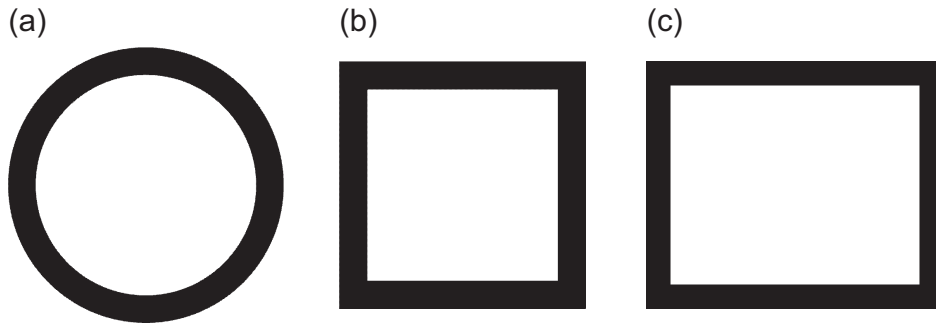
Figure 3.3: Bitmap images for fabricating (a) disk, (b) sqare and (c) rectangular groove-type mesa samples.
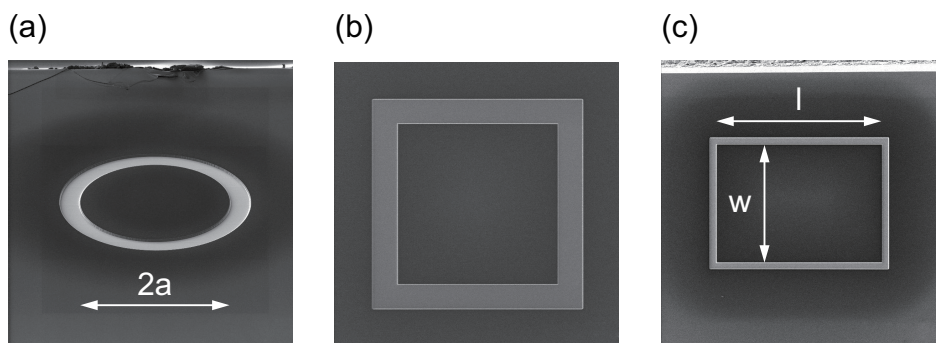
Figure 3.4: SIM images of (a) disk, (b) square, and (c) rectangular mesas.
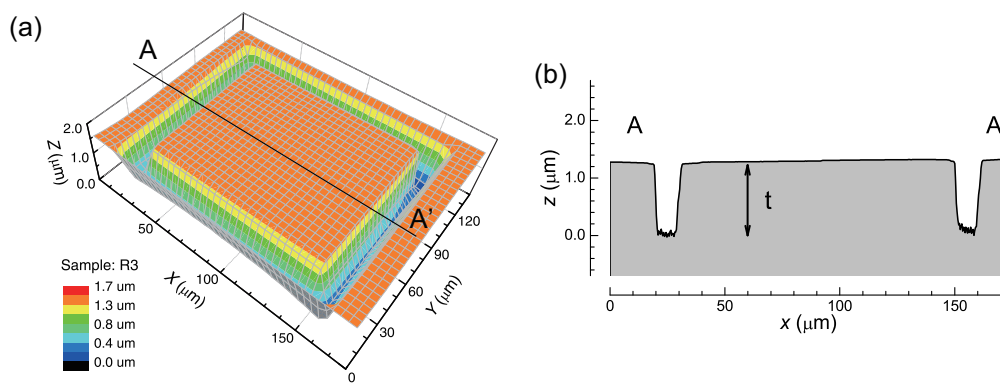
Figure 3.5: (a) Three-dimensional plot of sample R1 measured by the AFM. (b) Profile curve at line A–A' indicated in Fig. 3.5(a).
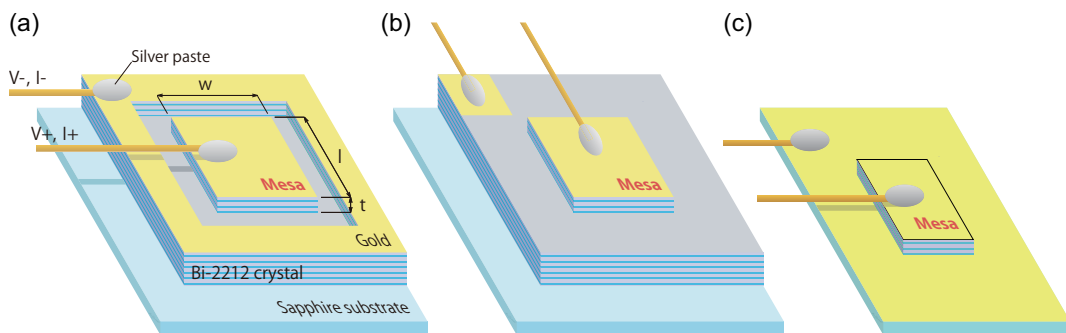
AFM analysis

The dimensions of all samples used for the present experiment are measured by using the atomic force microscope (AFM, KEYENCE Co., VN-8000) and are summarized in Table 3.1. Since the mesa height t is typically 1 µm, "Contact Mode" analysis with a maximum measurement area of 200×200 µm^2 was selected. By using provided software "VN Analyzer", the accumulated data set was converted into the comma separated value (CSV) format. Figure 3.5(a) shows the three-dimensional image of groove-type R1 sample, while Fig. 3.4(b) represents the profile curve at a line A–A' indicated in Fig. 3.5(a). The top cross-section length is typically approximately 5–10% smaller than the bottom one.

Table 3.1: List of the parameters of the samples used for the present study.

No.	Geometry	type	a [µm]	w [µm]	ℓ [µm]	t [µm]	$T_c(\Delta T_c)$
D1	Disk	groove	33.9–38.9			1.4	88.3 (1.9)
D2	Disk	groove	48.9–51.5			1.5	88.5 (2.0)
D3	Disk	groove	61.5–65.0			1.6	85.9 (4.0)
S1	Square	groove		66.7–75.7	70.9–81.6	1.7	87.7 (1.1)
S2	Square	groove		144–155	152–162	1.6	85.8 (3.1)
R1	Rectangle	groove		99.2–102	137–140	1.3	81.1 (6.6)
R2	Rectangle	SA		61.1–63.7	331–333	1.5	83.3 (6.7)
R3	Rectangle	groove		96.8–103	118–123	1.2	80.5 (1.7)
R4	Rectangle	groove		59.7–64.4	200	1.5	85.9 (3.6)
R5	Rectangle	terrace		54.6–70.7	300	1.9	82.3 (2.5)
R6	Rectangle	terrace		72.9–81.9	400	1.2	80.6 (6.3)
R7	Rectangle	groove		88.7–92.2	145.7–151.6	0.9	80.9 (1.7)
R8	Rectangle	terrace		62.4–78.6	400	1.9	83.6 (2.3)

3.2   Measurement system

Electronics and detection system

Figure 3.6(a) shows the circuit diagram for the current-voltage (I-V) characteristic measurement used in the present study. The load resistance R_{LO}, the standard resistor $R_{\mathrm{S}} = 10$ Ω, and the mesa sample are connected in series to the constant voltage source. The current through the mesa sample is obtained by the voltage drop at R_{S}. The voltage appearing in the mesa sample is measured directly by using the DC differential amplifier. Before starting each I-V measurement, we adjust R_{LO} appropriately in order to select either the current-bias mode or the voltage-bias mode: $R_{\mathrm{LO}} = 0$ corresponds to the voltage sweep, while a large R_{LO} (typically $R_{\mathrm{LO}} > 1$ kΩ) corresponds to the current sweep.
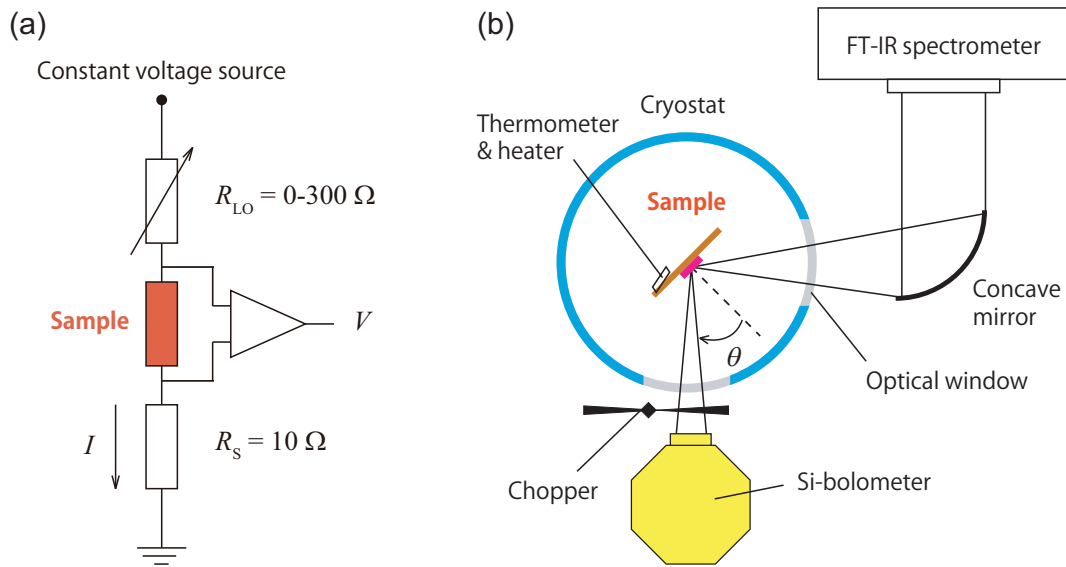
Figure 3.6: (a) Electric circuit diagram. (b) Top view of the optical system.

Figure 3.6 shows the optical system for detecting the terahertz (THz) waves emitted from the sample. The radiation intensity is measured by using the Si-bolometer (IR Laboratory Co., Ltd.). According to the specifications of the bolometer, it allows us to detect the far-infrared electromagnetic wave with the wavelength between 15 to 2,000 μm, corresponding to approximately 0.15–20 THz. A liquid ^{4}He-flow type cryostat with two optical polyethylene windows (Oxford Instruments, CF1104) was used for cooling the mesa sample. The sample was mounted on the cooled copper finger plate, and the bath temperature was monitored by the RhFe thermometer attached close to the sample. The detection angle θ indicated in Fig. 3.6 can be adjusted by rotating the inserted sample holder with respect to the cryostat and the other measuring equipment. The optical chopper revolving at a frequency of 70–100 Hz was placed in the optical path between the cryostat and the bolometer in order to modulate the THz wave for the lock-in detection. The radiation spectrum was analyzed by the Fourier transform infrared (FT-IR) spectrometer (JASCO Co., FARIS-1), which was placed in the direction of another window as shown in Fig. 3.6.

Collecting optical system

Figure 3.7 shows the top view of the collecting optical system used for measuring the total radiation power. In order to collimate the diverging THz waves emitted from the mesa, then to make it parallel and to focus it on the target, a hemispherical Si lens, plastic lenses (PAX Co., Terahertz-Super Lens "Tsurupica"), and off-axis parabolic mirror were used. Here, we note that the estimated solid angle to the detector window is 0.6 sr, which is about 20 times larger than the value that has been used in the previous experiments without collimation. This allows us to directly measure the total radiation power from the radiating sample without considering the spatial distribution of the radiation intensity.
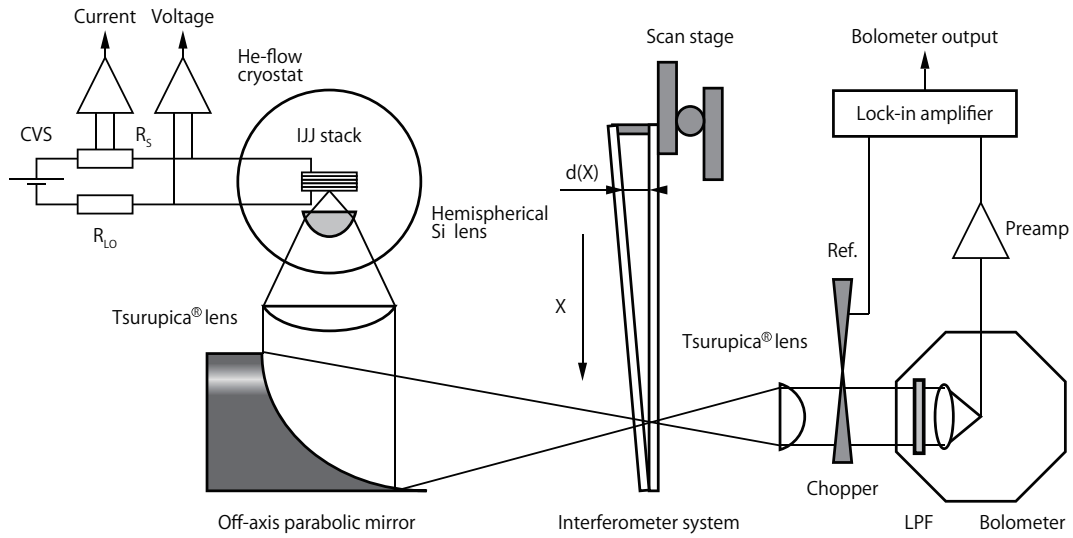
Figure 3.7: Top view of the collecting optical system.
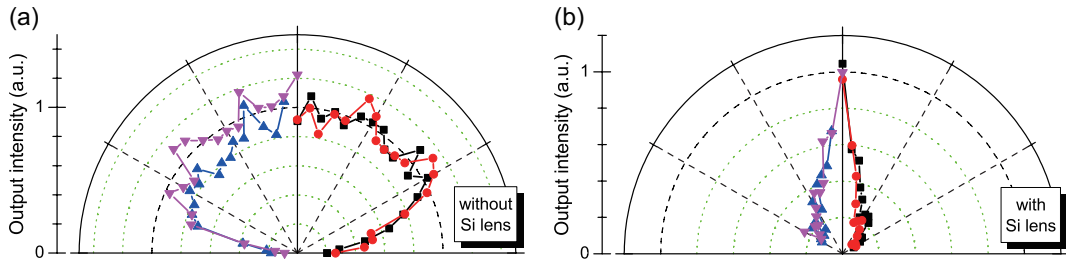
Figure 3.8: Collimation effect by the Si lens put immediately above the radiating sample.

We could indeed check on and confirm the collimation effect of the widely spreading radiation by the Si lens attached immediately in front of the radiating sample by measuring the radiation patterns. Figures 3.8(a) and 3.8(b) show the radiation patterns without and with using the Si lens, respectively. These results clearly demonstrate that the Si lens works as a collimater and makes the pattern more unidirectional. Since the collecting angle of the plastic lens is estimated to be about $\pm 30°$, we can monitor the total radiation power from the radiating sample with the present collecting system.

Interferometer system

At the focal point of the parabolic mirror in the collecting optical system shown in Fig. 3.7, an interferometer system to calibrate the radiation frequency is constructed. Figure 3.9(a) shows the handmade wedge type of device composed of two flat quartz plates and stainless-steel insert. This wedge is fixed on the 1D scan stage as shown in Fig. 3.7, and the raster scan is then performed in a horizontal (X) direction, where the interspace distance of the wedge d linearly increases with X. Since the THz wave is monochromatic, one can see

the interference pattern of the transmittance with X as shown in Fig. 3.9(b).

Figure 3.9(c) shows the data cut out of Fig. 3.9(b), showing the beautiful oscillation of the transmittance with an approximately 20% magnitude. The negligible drift due to the focus shift is subtracted in Fig. 3.9(c). The inset of Fig. 3.9(c) presents the schematic view of the handmade wedge. From a least-square analysis with a sinusoidal wave, the radiation frequency f_{cal} can be calculated, for example, $f_{cal} = 0.619$ THz ($\sigma = 0.0004$ THz, $R^2 = 0.958$), which is in good agreement with the value of 0.620 THz separately measured by the FT-IR spectrometer. In Fig. 3.9(c), an appropriate fitting curve is also presented along with the experimental data. For the data acquisition, a homemade LabVIEW (National Instruments Co.) program is used. By using this interferometer system, the radiation power and the frequency can be monitored simultaneously much faster than by the FT-IR spectrometer.
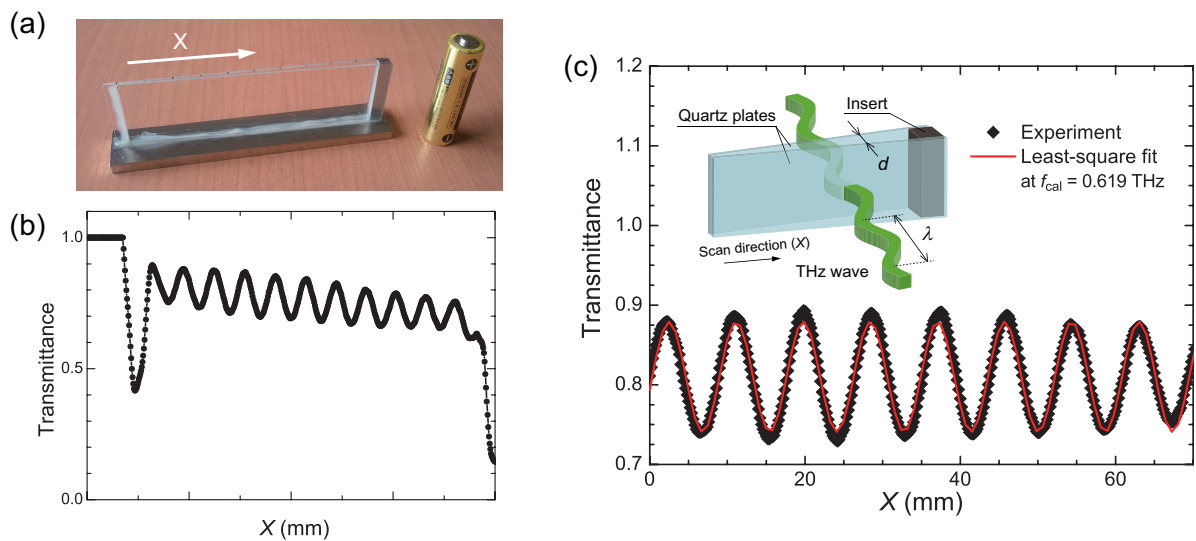
Figure 3.9: (a) A photo of a handmade wedge-shaped interferometer. (b) Transmittance of the incident THz wave versus X. (c) The interference pattern obtained from Fig. 3.8(b). The solid line overlaid on the data points presents a least-square fitting curve based on a sinusoidal wave. The inset presents the schematic view of the interferometer.

Chapter 4

Cavity resonance conditions

4.1 Introduction

After the first report of THz radiation from the intrinsic Josephson junctions in the high transition temperature superconductor $Bi_2Sr_2CaCu_2O_{8+\delta}$ with remarkably high intensity [5], it was pointed out that the mesa structure constructed on a cleaved $Bi_2Sr_2CaCu_2O_{8+\delta}$ thin crystal was important to generate the THz wave, since it can definitely act as a microstrip antenna that gives rise to the geometrical cavity resonance. At that time, long rectangular mesas which typically have a size of $60 \times 300 \times 1$ μm^3 were studied, so that we could observe the linear relation between the radiation frequency and the inverse of the mesa width as expected from the microstrip antenna model. This experimental fact demonstrated that the cavity resonance with a half-wavelength standing electromagnetic wave inside the mesa was excited. Although it is very interesting to examine the THz radiation from other geometrical mesa shapes, such as cylindrical disk, square, triangle, and so on, the conventional fabrication techniques mostly using a photolithography and argon ion milling machine have little flexibility to control the geometrical shape of the mesa.

In this chapter, we will make a point of improving the facility of the sample preparation technique by using the focused ion beam machine, and will focus our discussion mainly on the cavity resonance effect on the radiation from various geometrical mesa shapes. First, some theoretical formulations of the cavity resonance conditions will be derived from the conventional microstrip antenna model. Next, the experimental results and discussion will be presented in sequence. Some new analytical methods for analyzing the data for the spatial radiation pattern will be introduced. Finally, we will summarize this chapter in the conclusions.

4.2 Theoretical formulation

4.2.1 Fundamentals of the antenna

Maxwell equations

The electric field $\boldsymbol{E}$ and the magnetic flux density $\boldsymbol{B}$ in the uniform medium as a function of space coordinates $\boldsymbol{r}$ and time t obey the Maxwell equations in the form:

$$\nabla \cdot \boldsymbol{D}(\boldsymbol{r},t) = \rho(\boldsymbol{r},t) \tag{4.1}$$

$$\nabla \cdot \boldsymbol{B}(\boldsymbol{r},t) = 0 \tag{4.2}$$

$$\nabla \times \boldsymbol{H}(\boldsymbol{r},t) - \frac{\partial \boldsymbol{D}(\boldsymbol{r},t)}{\partial t} = \boldsymbol{J}(\boldsymbol{r},t) \qquad \text{(Ampere's law)} \tag{4.3}$$

$$\nabla \times \boldsymbol{E}(\boldsymbol{r},t) + \frac{\partial \boldsymbol{B}(\boldsymbol{r},t)}{\partial t} = 0. \qquad \text{(Faraday's law)} \tag{4.4}$$

where $\rho(\boldsymbol{r},t)$ is the electric charge, $\boldsymbol{J}(\boldsymbol{r},t)$ the electric current density, and $\boldsymbol{M}(\boldsymbol{r},t)$ the magnetic current density, respectively. If the amplitude of $\boldsymbol{E}(\boldsymbol{r},t)$ in the uniform medium is not so large, then the electric flux density $\boldsymbol{D}(\boldsymbol{r},t)$ and the magnetic field $\boldsymbol{H}(\boldsymbol{r},t)$ can be expressed as

$$\boldsymbol{D}(\boldsymbol{r},t) = \varepsilon \boldsymbol{E}(\boldsymbol{r},t) \qquad \text{and} \qquad \boldsymbol{H}(\boldsymbol{r},t) = \frac{1}{\mu} \left[\boldsymbol{B}(\boldsymbol{r},t) - \boldsymbol{M}(\boldsymbol{r},t) \right], \tag{4.5}$$

where ε is the dielectric constant and μ is the magnetic permeability, respectively. ε and μ are also expressed as $\varepsilon = \varepsilon_0 \, \varepsilon_r$ and $\mu = \mu_0 \, \mu_r$ with $\varepsilon_0 = 8.854 \times 10^{-12}$ [F/m] and $\mu_0 = 4\pi \times 10^{-7}$ [H/m] in the vacuum, where ε_r and μ_r denote the relative permittivity and the magnetic permeability, respectively. Equation (4.1) implies that the electric field $\boldsymbol{E}$ exists due to the electric charge ρ as shown in Fig. 4.1(a), while Eq. (4.2) guarantees the non-existence of the monopole magnetic charge as shown in Fig. 4.1(b). Equation (4.3) suggests that the electric current $\boldsymbol{J}$ can generate the magnetic field $\boldsymbol{H}$ around the electric current in the right-hand screw direction as shown in Fig. 4.1(c), while Eq. (4.4) suggests that the magnetic current $\boldsymbol{M}$ can develop the electromotive field $\boldsymbol{E}$ in the left-hand screw direction as shown in Fig. 4.1(d).

In order to deal with the AC fields $(\boldsymbol{E}(\boldsymbol{r},t), \boldsymbol{H}(\boldsymbol{r},t))$, we substitute the complex electric field $\boldsymbol{E}^t(\boldsymbol{r},t) = \boldsymbol{E}(\boldsymbol{r}) \, e^{j\omega t}$ and magnetic field $\boldsymbol{H}^t(\boldsymbol{r},t) = \boldsymbol{H}(\boldsymbol{r}) \, e^{j\omega t}$ into the Maxwell equations, where j denotes $\sqrt{-1}$ in engineering notation. Then, we obtain

$$\begin{aligned} \nabla \times \boldsymbol{H}(\boldsymbol{r}) &= j\omega\varepsilon \, \boldsymbol{E}(\boldsymbol{r}) + \boldsymbol{J}(\boldsymbol{r}) \\ -\nabla \times \boldsymbol{E}(\boldsymbol{r}) &= j\omega\mu \, \boldsymbol{H}(\boldsymbol{r}) + \boldsymbol{M}(\boldsymbol{r}). \end{aligned} \tag{4.6}$$

It is clear that $(\boldsymbol{E}, \boldsymbol{H})$ in Eqs. (4.6) naturally satisfy the time-independent Maxwell equations. Note that on the place of $\boldsymbol{J}$, in some cases, we use $\boldsymbol{M}$ (an unmeasurable quantity) to analyze the electrodynamics of the antenna, so that we can include the discontinuity of the electric field component parallel to the open-edge boundary of the antenna.
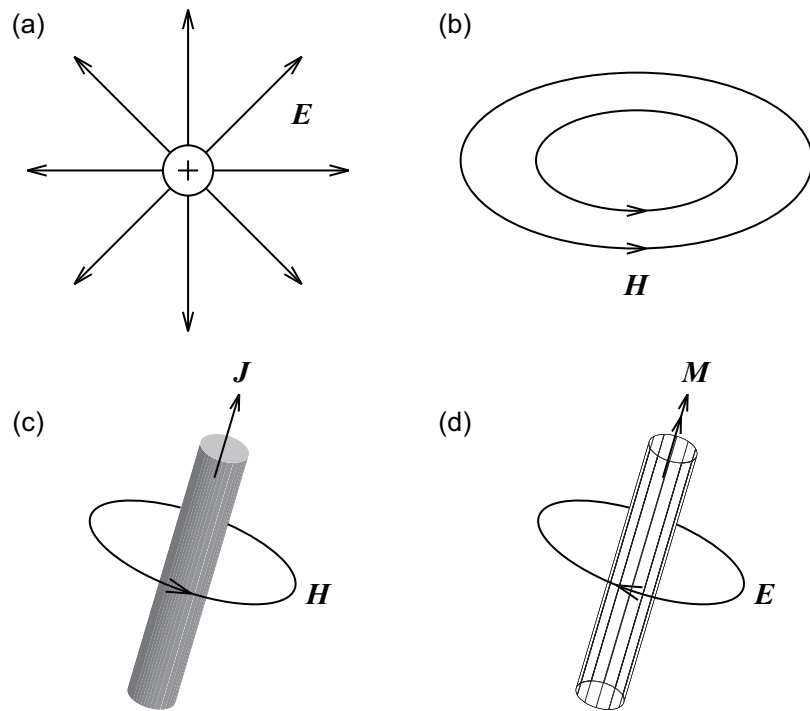
Figure 4.1: Maxwell equations.
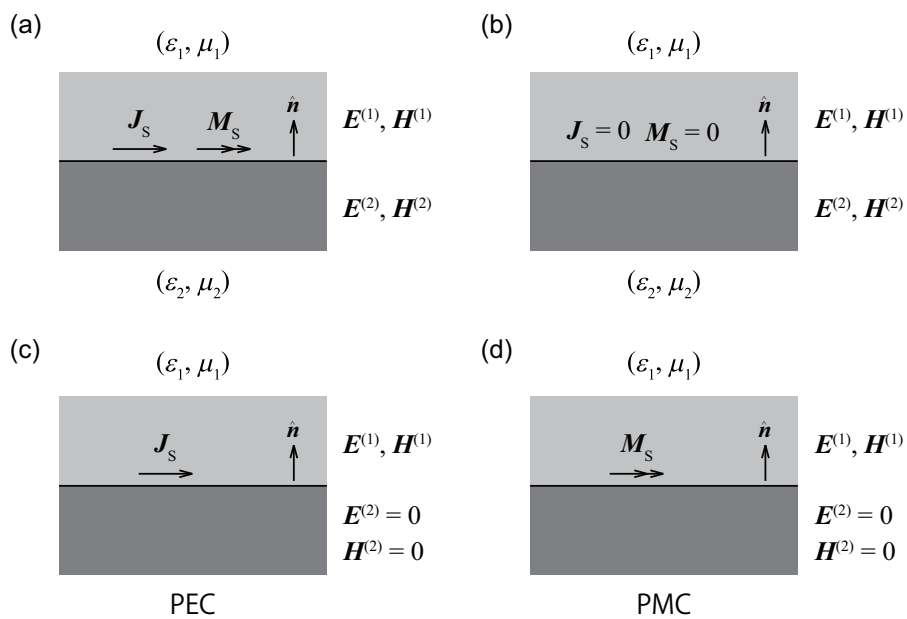
Figure 4.2: Boundary conditions.

Boundary conditions

The boundary conditions at the surface between media 1 (ε_1, μ_1) and 2 (ε_2, μ_2) can be expressed by the following equations:

$$
\begin{aligned}
\hat{\boldsymbol{n}} \times (\boldsymbol{H}^{(1)} - \boldsymbol{H}^{(2)}) &= \boldsymbol{J}_S \\
(\boldsymbol{E}^{(1)} - \boldsymbol{E}^{(2)}) \times \hat{\boldsymbol{n}} &= \boldsymbol{M}_S
\end{aligned}
\tag{4.7}
$$

where $\boldsymbol{J}_S$ ($\boldsymbol{M}_S$) represents the surface electric (magnetic) current, and $\hat{\boldsymbol{n}}$ is a unit vector normal to the boundary (see Fig. 4.2). The superscripts (i) denote the respective uniform media i; $i = 1, 2$. When ε and μ are finite values, the surface currents $\boldsymbol{J}_S$ and $\boldsymbol{M}_S$ should equal zero as shown in Fig. 4.2(b).

Suppose medium 2 is the perfect electric conductor (PEC), the surface electric current $\boldsymbol{J}_S$ flows for satisfying $\boldsymbol{E}^{(2)} = \boldsymbol{H}^{(2)} = 0$ as shown in Fig. 4.2(c), and the boundary conditions are modified as follows:

$$
\hat{\boldsymbol{n}} \times \boldsymbol{H}^{(1)} = \boldsymbol{J}_S \qquad \text{and} \qquad \boldsymbol{E}^{(1)} \times \hat{\boldsymbol{n}} = 0.
\tag{4.8}
$$

When the $\boldsymbol{H}$ component parallel to the boundary is not zero, its amplitude is equal to $|\boldsymbol{J}_0|$ and the $\boldsymbol{E}$ component parallel to the boundary is zero. This suggests that $\boldsymbol{E}$ is always polarized in the surface direction. In another case, if medium 2 is the perfect magnetic conductor (PMC), the surface magnetic current $\boldsymbol{M}_S$ flows over the surface as shown in Fig. 4.2(d), and the boundary conditions are again modified as follows:

$$
\hat{\boldsymbol{n}} \times \boldsymbol{H}^{(1)} = 0 \qquad \text{and} \qquad \boldsymbol{E}^{(1)} \times \hat{\boldsymbol{n}} = \boldsymbol{M}_S.
\tag{4.9}
$$

Equivalence theorem

Figure 4.3(a) shows the closed domain which contains the first order wave sources, such as the antenna, transmitter, *etc.*, and shows the surrounding infinite domain d. These domains are separated by the closed curve C. Figure 4.3(b) shows another closed domain with no electromagnetic fields inside it ($\boldsymbol{E} = \boldsymbol{H} = 0$) and the infinite domain d with the same electromagnetic fields as d shown in Fig. 4.3(a). In Fig. 4.3(b), since $\boldsymbol{E}$ and $\boldsymbol{H}$ are discontinuous on C, the spontaneous surface currents $\boldsymbol{J}_S = \hat{\boldsymbol{n}} \times \boldsymbol{H}$ and $\boldsymbol{M}_S = \boldsymbol{E} \times \hat{\boldsymbol{n}}$ (second order wave sources) have to flow over C in order to satisfy the boundary conditions of Eqs. (4.7). As a result, we can assume that $\boldsymbol{J}_S$ and $\boldsymbol{M}_S$ intrinsically exist in the infinite uniform domain d, and that Fig. 4.3(a) and 4.3(b) are equivalent to each other.

By using this equivalent theorem, we can make the problem with the uncertain wave sources much simple. As a typical example, we consider the equivalent problem with the dipole antenna presented in Fig. 4.3(c). By taking the closed curve C immediately lateral to the antenna pole, we can remove the metal pole and replace it with the vacuum, and can assume the surface currents $\boldsymbol{J}_S$ and $\boldsymbol{M}_S$ which give rise to $\boldsymbol{E} = \boldsymbol{H} = 0$ inside C. Since $\boldsymbol{E} \times \hat{\boldsymbol{n}} = 0$ at the surface boundary as expected from Eqs. (4.7), $\boldsymbol{M}_S$ exists only at the
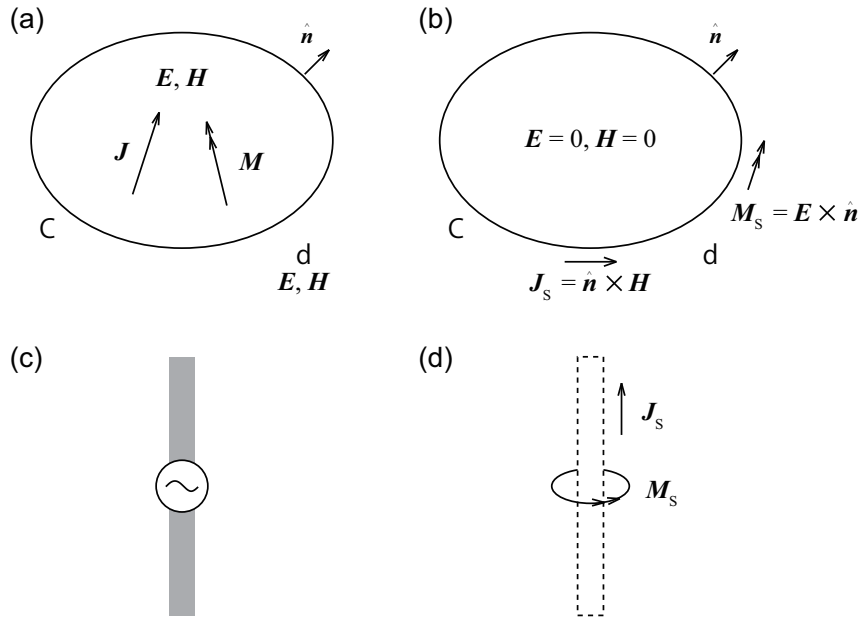
Figure 4.3: Equivalence theorem.

feed edge, whereas $\boldsymbol{J}_S$ acts as the source of the dipole radiation. Figure 4.3(d) shows the equivalent antenna to Fig. 4.3(c). Since the $\boldsymbol{J}_S$ and $\boldsymbol{M}_S$ can be chosen at the convenience of the problem, in some case we can use the Green function method to obtain the differential equations for $\boldsymbol{J}_S$ and $\boldsymbol{M}_S$, and solve them by the most efficient method, such as the moment method.

Vector potential

If there is an electric current $\boldsymbol{J}$ in the uniform medium $(\varepsilon,\ \mu)$ without a magnetic current $(\boldsymbol{M}=0)$, the symmetric equations (4.6) can be rewritten in the form:

$$\nabla \times \boldsymbol{H} = j\omega\varepsilon\boldsymbol{E} + \boldsymbol{J} \qquad \text{and} \qquad -\nabla \times \boldsymbol{E} = j\omega\mu\boldsymbol{H}. \tag{4.10}$$

By calculating the divergence of Eq. (4.10) with considering that $\nabla \cdot \nabla \times \boldsymbol{E} = 0$ leads to $\nabla \cdot \boldsymbol{H} = 0$, the magnetic field $\boldsymbol{H}$ can be represented by the magnetic vector potential $\boldsymbol{A}$ as

$$\boldsymbol{H} = \frac{1}{\mu}\left[\nabla \times \boldsymbol{A}\right]. \tag{4.11}$$

Hence, the electric field $\boldsymbol{E}$ can be represented by introducing $\boldsymbol{A}$ in the form:

$$\boldsymbol{E} = -j\omega\mu\boldsymbol{A} + \frac{\nabla(\nabla \cdot \boldsymbol{A})}{j\omega\varepsilon} \tag{4.12}$$

$$\boldsymbol{A}(\boldsymbol{r}) = \int \frac{\boldsymbol{J}(\boldsymbol{r}')\exp(-jk|\boldsymbol{r}-\boldsymbol{r}'|)}{4\pi|\boldsymbol{r}-\boldsymbol{r}'|}\,dv', \tag{4.13}$$

where $k = 2\pi/\lambda$, $\exp(-jk|\boldsymbol{r}-\boldsymbol{r}'|)/(4\pi|\boldsymbol{r}-\boldsymbol{r}'|)$ is the Green function in the free space, and

$$\boldsymbol{r} = \hat{\boldsymbol{x}}x + \hat{\boldsymbol{y}}y + \hat{\boldsymbol{z}}z \qquad \text{and} \qquad \boldsymbol{r}' = \hat{\boldsymbol{x}}x' + \hat{\boldsymbol{y}}y' + \hat{\boldsymbol{z}}z' \tag{4.14}$$

are radius vectors from the origin to the observation point P and to the radiation source point, respectively. In another case, if there is a magnetic current $\boldsymbol{M}$ without an electric current ($\boldsymbol{J} = 0$), Eqs. (4.6) can be rewritten in the form:

$$\nabla \times \boldsymbol{H} = j\omega\varepsilon\boldsymbol{E} \qquad \text{and} \qquad -\nabla \times \boldsymbol{E} = j\omega\mu\boldsymbol{H} + \boldsymbol{M}. \tag{4.15}$$

By considering the symmetry in Eqs. (4.10) and (4.15), ($\boldsymbol{E}$, $\boldsymbol{H}$) can be described by introducing the electric vector potential $\boldsymbol{A}_m$ in the form:

$$\begin{aligned} \boldsymbol{A}_m(\boldsymbol{r}) &= \int \frac{\boldsymbol{M}(\boldsymbol{r}')\exp(-jk|\boldsymbol{r} - \boldsymbol{r}'|)}{4\pi|\boldsymbol{r} - \boldsymbol{r}'|}\,dv' \\ \boldsymbol{H} &= -j\omega\varepsilon\boldsymbol{A}_m + \frac{\nabla(\nabla \cdot \boldsymbol{A}_m)}{j\omega\mu} \\ \boldsymbol{E} &= -\nabla \times \boldsymbol{A}_m. \end{aligned} \tag{4.16}$$

4.2.2 Cavity resonance conditions

Microstrip antenna

The microstrip antenna (MSA) element known to be a typical compact planar antenna is composed of a thin dielectric plate sandwiched by two metal plates as the radiating plate and the ground plate. Since the commercially available MSA element provides the dominant (fundamental) mode radiation with the open-edge boundary condition, the size of the element is typically below a half wavelength of the standing electromagnetic wave inside the cavity. It is also convenient that the MSA has usually the unidirectional radiation pattern without using any kind of reflectors. The unload Q-value (Q_0) of typically 10–100, which is a very important parameter for designing and constructing MSAs, exhibits an inverse correlation with the radiation efficiency (η).

In previous studies, it has been pointed out that the mesa structure, which will be introduced in a later section, can act as the MSA for giving rise to the intense THz radiation from $Bi_2Sr_2CaCu_2O_{8+\delta}$ (Bi-2212). Although several analytical methods have so far been validated to analyze the characteristics of the MSA, in this study, we use the open-edge cavity model which derives accurate analytical solutions for the electrodynamics of the MSA in a relatively simple manner.

Disk MSA

Figure 4.4 shows the schematic view of the disk MSA. When the substrate thickness t is much smaller than the wavelength λ_0 ($= 2\pi/k_0$) in the free space ($k_0 t \ll 1$), the transverse magnetic (TM) standing wave that has only the z-component of $\boldsymbol{E}$ can be favorably excited with $H_z = 0$. Inside the disk patch cavity, the wave equations for E_z in the cylindrical coordinate system can be obtained from the wave equations in the form:

$$\frac{1}{\rho} \cdot \frac{\partial}{\partial\rho}\left(\rho\frac{\partial}{\partial\rho}E_z\right) + \frac{1}{\rho^2} \cdot \frac{\partial^2}{\partial\phi^2}E_z + k^2 E_z = 0. \tag{4.17}$$
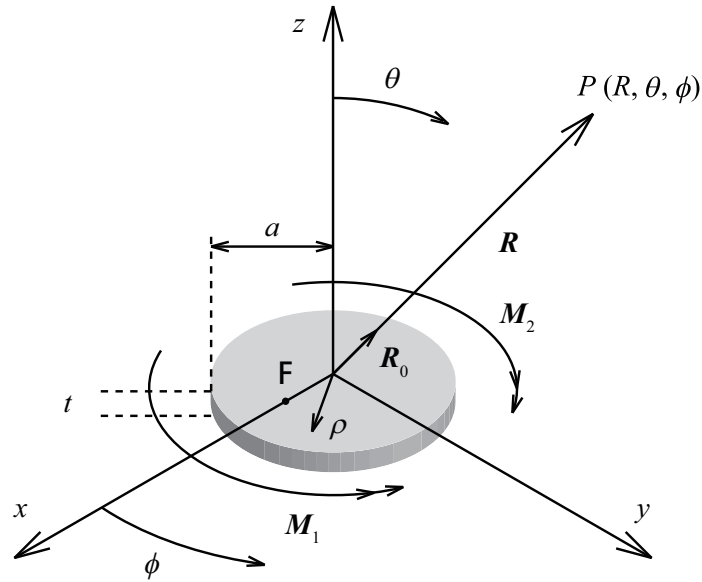
Figure 4.4: Disk MSA.
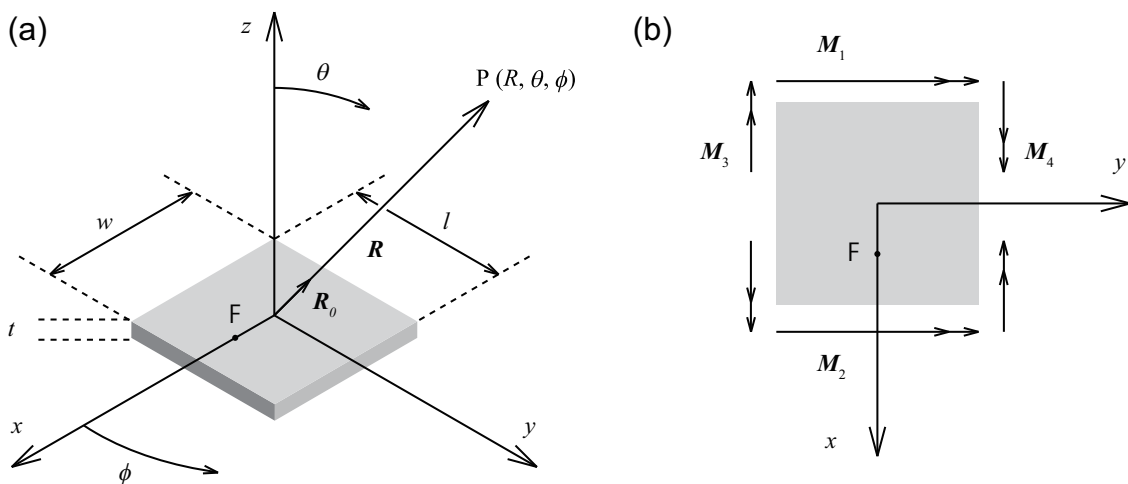
Figure 4.5: (a) Rectangular MSA. (b) Four magnetic currents $\boldsymbol{M}_i$ $(i = 1, 2, 3, 4)$ for the dominant TM(1, 0) mode.

With the separation of the variables as $E_z = R(\rho)\Phi(\phi)$, we can rewrite Eq. (4.17) as

$$\left(\frac{\rho^2}{R} \cdot \frac{d^2 R}{d\rho^2} + \frac{\rho}{R} \cdot \frac{dR}{d\rho} + k^2 \rho^2 \right) + \frac{1}{\Phi} \cdot \frac{d^2 \Phi}{d\phi^2} = 0, \tag{4.18}$$

where $R(\rho)$ and $\Phi(\phi)$ are for radial and angular components, respectively. Then, Eq. (4.18) can be separated into the following two differential equations:

$$\frac{\rho^2}{R} \cdot \frac{d^2 R}{d\rho^2} + \frac{\rho}{R} \cdot \frac{dR}{d\rho} + k^2 \rho = m^2 \tag{4.19}$$

$$\frac{1}{\Phi} \cdot \frac{d^2 \Phi}{d\phi^2} = -m^2 \qquad (m : \text{integer}). \tag{4.20}$$

By transforming Eq. (4.19), we obtain Bessel's differential equation

$$\frac{d^2 R}{d\rho^2} + \frac{1}{\rho} \cdot \frac{dR}{d\rho} + \left(k^2 - \frac{m^2}{\rho^2} \right) R = 0 \tag{4.21}$$

and obtain its exact solution:

$$R = A_1 J_m(k\rho) + A_2 Y_m(k\rho), \tag{4.22}$$

where A_1 and A_2 are constants. Since the Neumann function $Y_m(k\rho)$ in the right-hand side in Eq. (4.22) approaches minus infinity when $\rho \to 0$, suggesting that it becomes an improper solution, the physically-meaningful solution can be expressed in the form:

$$R = A J_m(k\rho), \tag{4.23}$$

where A is a constant which can be different from A_1.

For another equation (4.20), the harmonic wave solution can be expressed with constants B_i $(i = 1, 2)$ and B in the form:

$$\Phi = B_1 \cos(m\phi) + B_2 \sin(m\phi) = B \cos\{m(\phi - \phi_f)\}, \tag{4.24}$$

where ϕ_f reflects the feed point as indicated by F in Fig. 4.4. Here, we put F on the x-axis, so that $\phi_f = 0$. Thus, the wave solution of Eq. (4.17) can be obtained in the form:

$$E_z = E_0 J_m(k\rho) \cos(m\phi) \qquad (E_0 : \text{constant}). \tag{4.25}$$

As expected from Eq. (4.7), the boundary condition for the disk MSA at the open-edge boundary $(\rho = a)$ should be given in the form:

$$(\partial E_z / \partial \rho)|_{\rho=a} = 0. \tag{4.26}$$

By using Eqs. (4.25) and (4.26), we can obtain the resonance condition of $J'_m(\chi_{mp}) = 0$, where χ_{mp} is the p-th zero of the first derivative of $J_m(ka)$. For the disk TM(m, p) mode, $k = k_{mp} = \chi_{mp}/a$ is the characteristic wavenumber, and

$$E_z = E_0 J_m(k_{mn}\rho) \cos(m\phi), \tag{4.27}$$

is the z-component of $\boldsymbol{E}$ inside the cavity. Other components of $(\boldsymbol{E}, \boldsymbol{H})$ can also be given by the Maxwell equations in the form:

$$H_\rho = \frac{j}{\omega\mu} \cdot \frac{1}{\rho} \cdot \frac{\partial E_z}{\partial \phi}$$

and   (4.28)

$$H_\phi = -\frac{j}{\omega\mu} \cdot \frac{\partial E_z}{\partial \rho}.$$

Therefore, we obtain a set of equations for the internal $(\boldsymbol{E}, \boldsymbol{H})$ inside the patch cavity as follows:

$$E_z = E_0 J_m(k_{mp}\rho) \cos(m\phi)$$

$$H_\rho = -\frac{jm}{\omega\mu\rho} E_0 J_m(k_{mp}\rho) \sin(m\phi)$$ (4.29)

$$H_\phi = -\frac{jk}{\omega\mu} E_0 J'_m(k_{mp}\rho) \cos(m\phi),$$

Figure 4.6(a) shows the three-dimensional plots of the internal electric field E_z for disk TM(1, 1), TM(2, 1), TM(0, 1), and TM(3, 1) modes.

For the dominant disk TM(1, 1) mode, the internal $(\boldsymbol{E}, \boldsymbol{H})$ and the radiation frequency f_{11}^d can be calculated from Eq. (4.29) with $m = p = 1$ in the form:

$$E_z = E_0 J_1(k_{11}\rho) \cos(\phi)$$

$$H_\rho = -\frac{j}{\omega\mu\rho} E_0 J_1(k_{11}\rho) \sin(\phi)$$

$$H_\phi = -\frac{jk}{\omega\mu} E_0 J'_1(k_{11}\rho) \cos(\phi)$$ (4.30)

$$E_\rho = E_\phi = H_z = 0$$

and

$$f_{11}^d = \frac{\chi_{11} c_0}{2\pi a \sqrt{\varepsilon_r}} \qquad (\chi_{11} = 1.841).$$ (4.31)

Rectangular MSA

Figure 4.5(a) shows the schematic view of the rectangular MSA. As for the disk MSA, the following analysis can be applied only with the assumption of $k_0 t \ll 1$. The internal electric field E_z inside the rectangular cavity can be obtained from the following wave equations:

$$\left(\nabla_t^2 + k^2\right) E_z = 0 \qquad \text{(cavity)}$$ (4.32)

and

$$\frac{\partial E_z}{\partial \hat{\boldsymbol{n}}} = 0, \qquad\qquad \text{(open edge)}$$ (4.33)

where $\hat{\boldsymbol{n}}$ denotes the normal unit vector and $\nabla_t^2 = \partial^2/\partial x^2 + \partial^2/\partial y^2$. By the same method of separation of variables used for the disk MSA, by considering the boundary condition of Eq. (4.33), we obtain

$$E_z = E_0 \cos\left(\frac{m\pi}{w}x + \frac{m\pi}{2}\right)\cos\left(\frac{p\pi}{\ell}y + \frac{p\pi}{2}\right), \tag{4.34}$$

and the radiation frequency

$$f_{mp}^r = \frac{c_0}{2\sqrt{\varepsilon_r}}\sqrt{\left(\frac{m\pi}{w}\right)^2 + \left(\frac{p\pi}{\ell}\right)^2}, \tag{4.35}$$

where E_0 is the constant. By substituting E_z into the Maxwell equations, we obtain other components of $(\boldsymbol{E}, \boldsymbol{H})$ inside the cavity in the form:

$$
\begin{aligned}
E_z &= \frac{V_0}{t}\cos\left(\frac{m\pi}{a}x + \frac{m\pi}{2}\right)\cos\left(\frac{p\pi}{b}y + \frac{p\pi}{2}\right) \\
H_x &= -\frac{j\omega\varepsilon}{k^2}\cdot\frac{p\pi}{b}\cdot\frac{V_0}{t}\cos\left(\frac{m\pi}{a}x + \frac{m\pi}{2}\right)\sin\left(\frac{p\pi}{b}y + \frac{p\pi}{2}\right) \\
H_y &= \frac{j\omega\varepsilon}{k^2}\cdot\frac{m\pi}{a}\cdot\frac{V_0}{t}\cos\left(\frac{m\pi}{a}x + \frac{m\pi}{2}\right)\cos\left(\frac{p\pi}{b}y + \frac{p\pi}{2}\right)
\end{aligned}
\tag{4.36}
$$

and

$$E_x = E_y = H_z = 0.$$

where V_0 is the peak voltage at the magnetic wall $(V_0 = tE_0)$. Figure 4.6(b) shows the three-dimensional plots of the internal electric field E_z for rectangular TM(1, 0), TM(1, 1), TM(2, 0), and TM(2, 1) modes.

$(\boldsymbol{E}, \boldsymbol{H})$ and the radiation frequency for the dominant rectangular TM(1, 0) mode can be then calculated from Eq. (4.36) in the form:

$$
\begin{aligned}
E_z &= -\frac{V_0}{t}\sin\left(\frac{\pi}{w}x\right) \\
H_y &= \frac{j\omega\varepsilon}{k^2}\cdot\frac{\pi}{w}\cdot\frac{V_0}{t}\cos\left(\frac{\pi}{w}x\right) \\
E_x &= E_y = H_x = H_z = 0,
\end{aligned}
\tag{4.37}
$$

and

$$f_{10}^r = \frac{c_0}{2\sqrt{\varepsilon_r}w}. \tag{4.38}$$

4.2.3 Spatial radiation pattern

Radiation pattern for the disk TM(m, p) mode

The equivalent magnetic currents $\boldsymbol{M}$ as the radiation source can be calculated from E_z at the open edge $(\rho = a)$ in the form:

$$
\begin{aligned}
\boldsymbol{M} &= (\hat{\boldsymbol{z}}E_z)\times\hat{\boldsymbol{n}}|_{\rho=a} = \hat{\boldsymbol{\phi}}E_z|_{\rho=a} \\
&= \hat{\boldsymbol{\phi}}E_0 J_m(\chi_{mp})\cos m\phi,
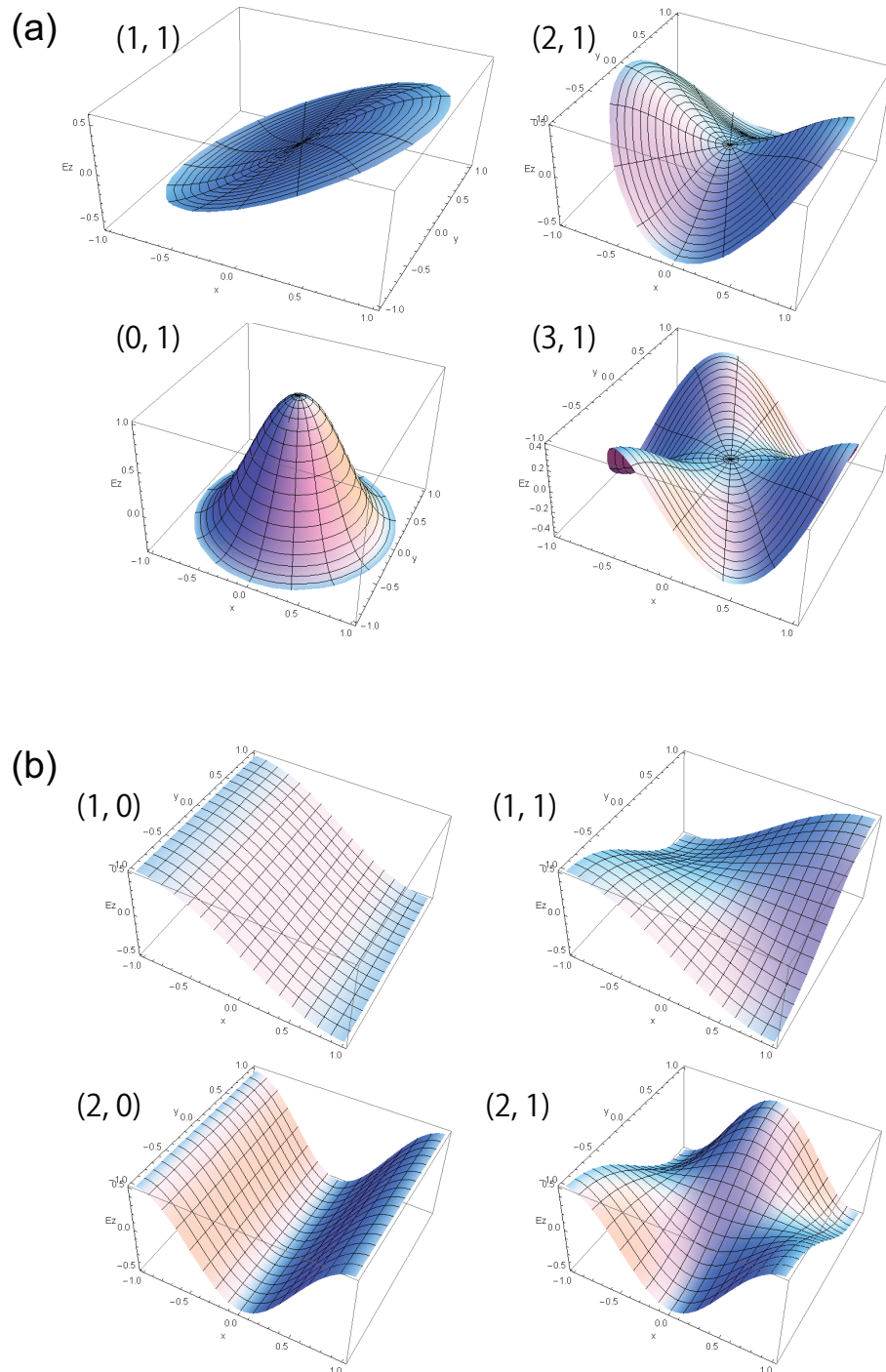\end{aligned}
\tag{4.39}
$$

Figure 4.6: Three-dimensional plots of the snapshots of the internal electric fields E_z for the disk MSA (a) and for the rectangular MSA (b).

where $\hat{\boldsymbol{n}}$ is the normal unit vector, $\hat{\boldsymbol{z}}$ and $\hat{\boldsymbol{\phi}}$ are the unit vectors in the z- and ϕ-directions, respectively. In Fig. 4.4, two $\boldsymbol{M}$ for the disk TM(1, 1) mode are presented. Then, we can calculate the far-field vector potential $\boldsymbol{A}_m$ by using Eq. (4.16) as follows:

$$\boldsymbol{A}_m = \frac{\varepsilon \exp(-jk_0R)}{4\pi R} \iint_S \boldsymbol{M} \exp(jk_0\Delta d) \, dS, \tag{4.40}$$

where $\Delta d = \hat{\boldsymbol{R}}_0 \cdot \boldsymbol{\rho}$ is the relative displacement of $\boldsymbol{M}$ from the origin with $\boldsymbol{R}_0$ of a unit vector (from the origin to the observation point) and $\boldsymbol{\rho}$ of a distance vector (from the origin to the source point):

$$\begin{aligned} \boldsymbol{R}_0 &= \sin\theta(\hat{\boldsymbol{x}}\cos\phi_0 + \hat{\boldsymbol{y}}\sin\phi_0) + \hat{\boldsymbol{z}}\cos\theta \\ \boldsymbol{\rho} &= \hat{\boldsymbol{x}}x + \hat{\boldsymbol{y}}y + \hat{\boldsymbol{z}}z = \hat{\boldsymbol{x}}a\cos\phi + \hat{\boldsymbol{y}}a\sin\phi + \hat{\boldsymbol{z}}z, \end{aligned} \tag{4.41}$$

where ϕ_0 is an arbitrary phase angle. Hence, Δd can be rewritten in the form:

$$\Delta d = a\cos(\phi - \phi_0)\sin\theta + z\cos\theta. \tag{4.42}$$

By substituting Eq. (4.42) into Eq. (4.40) and integrating it from $-t$ to t, the magnetic vector potential $\boldsymbol{A}_m$ can be calculated in the form:

$$\begin{aligned} \boldsymbol{A}_m = {} & \frac{\varepsilon}{4\pi}\left(\frac{\exp(-jk_0R)}{R}\right) \\ & \times \int_{-t}^{t}\int_0^{2\pi} \boldsymbol{M} \exp\left[jk_0\{a\cos(\phi - \phi_0)\sin\theta + z\cos\theta\}\right] a \, d\phi \, dz. \end{aligned} \tag{4.43}$$

With the transformation from the cylindrical coordinates (ρ, ϕ, z) to the polar coordinates (R, θ, ϕ_0), Eq. (4.43) can be rewritten again as

$$\begin{aligned} A_{m\theta} = {} & -\left(\frac{t\varepsilon a E_0 J_m(\chi_{mp})}{2\pi}\right)\left(\frac{\exp(-jk_0R)}{R}\right)\cos\theta \\ & \times \int_0^{2\pi} \sin(\phi - \phi_0)\cos(m\phi)\exp\{jk_0a\cos(\phi - \phi_0)\sin\theta\} \, d\phi \end{aligned}$$

and

$$\begin{aligned} A_{m\phi_0} = {} & \left(\frac{t\varepsilon a E_0 J_m(\chi_{mp})}{2\pi}\right)\left(\frac{\exp(-jk_0R)}{R}\right) \\ & \times \int_0^{2\pi} \cos(\phi - \phi_0)\cos(m\phi)\exp\{jk_0a\cos(\phi - \phi_0)\sin\theta\} \, d\phi, \end{aligned} \tag{4.44}$$

where we used the transform relationship:

$$\hat{\boldsymbol{\theta}} = -\hat{\boldsymbol{\phi}}\sin(\phi - \phi_0)\cos\theta$$

and

$$\hat{\boldsymbol{\phi}}_0 = \hat{\boldsymbol{\phi}}\cos(\phi - \phi_0) \tag{4.45}$$

and the integral approximation with the assumption of $k_0 t \ll 1$:

$$\int_{-t}^{t} \exp(j k_0 z \cos\theta) \, dz = 2t \left[\frac{\sin(k_0 t \cos\theta)}{k_0 t \cos\theta} \right] \cong 2t. \tag{4.46}$$

The far-field E_θ and E_{ϕ_0} are then calculated from $\boldsymbol{E} = -(1/\varepsilon)\nabla \times \boldsymbol{A}_m$ and $\boldsymbol{H} = -j\omega \boldsymbol{A}_m = (1/\eta_0)\hat{\boldsymbol{R}}_0 \times \boldsymbol{E}$ to be

$$E_\theta = -j\omega\eta_0 A_{m\phi_0}$$

and $\tag{4.47}$

$$E_{\phi_0} = j\omega\eta_0 A_{m\theta},$$

where $\eta_0 = \sqrt{\mu_0/\epsilon_0} = 120\pi$ is the characteristic impedance in the free space. By using the integral formula of the Bessel function

$$J_m(z) = \frac{1}{2\pi j^m} \int_0^{2\pi} \exp(j z \cos\Phi) \cdot \cos m\Phi \, d\Phi, \tag{4.48}$$

we can calculate the radiation patterns E_θ and E_ϕ from Eqs. (4.47) in the form:

$$E_\theta = j^m B_c \left(\frac{\exp(-j k_0 R)}{R} \right) \cos(m\phi_0)$$
$$\times \{ J_{m+1}(k_0 a \sin\theta) - J_{m-1}(k_0 a \sin\theta) \} \tag{4.49}$$

and

$$E_\phi = j^m B_c \left(\frac{\exp(-j k_0 R)}{R} \right) \cos\theta \sin(m\phi)$$
$$\times \{ J_{m+1}(k_0 a \sin\theta) + J_{m-1}(k_0 a \sin\theta) \}, \tag{4.50}$$

where $B_c = (V_0 a k_0/2)$ is the constant, and $V_0 = t E_0 J_m(\chi_{mp})$.

E_θ and E_ϕ for the dominant TM(1, 1) mode can be calculated from Eqs. (4.49) and (4.50) with $m = 1$ as follows:

$$E_\theta = -j(V_0 k_0 a) \left(\frac{\exp(-j k_0 R)}{R} \right) \cos\phi \, J_1'(k_0 a \sin\theta)$$

and $\tag{4.51}$

$$E_\phi = jV_0 \left(\frac{\exp(-j k_0 R)}{R} \right) \sin\phi \left(\frac{\cos\theta}{\sin\theta} \right) J_1(k_0 a \sin\theta),$$

where we used the following recurrence formulae of the Bessel function:

$$2J_m'(x) = J_{m-1}(x) - J_{m+1}(x) \tag{4.52}$$

and

$$\left(\frac{2m}{x} \right) J_m(x) = J_{m-1}(x) + J_{m+1}(x). \tag{4.53}$$

Figure 4.7(a) shows the spherical plot of the radiation pattern for the dominant disk TM(1, 1).

Radiation pattern for the rectangular TM(m, p) mode

Similar to the disk TM(m, p) mode, we can obtain the far-field radiation patterns E_θ and E_ϕ for the rectangular TM(m, p) mode from the contour integral of the magnetic currents $\boldsymbol{M}$ in the form:

$$E_\theta = j \left(\frac{V_0 F_1 F_2}{\lambda_0 R} \right) \exp(-jk_0 R) \left[\frac{f_1 \sin \phi}{f_m} + \frac{f_2 \cos \phi}{f_p} \right]$$

and

$$E_\phi = j \left(\frac{V_0 F_1 F_2}{\lambda_0 R} \right) \exp(-jk_0 R) \left[\frac{f_1 \cos \theta \cos \phi}{f_m} - \frac{f_2 \cos \theta \sin \phi}{f_p} \right],$$

(4.54)

where f_1, f_2, F_1, F_2, f_m, and f_p are defined as follows:

$$f_1 = jk_0 \sin \theta \cos \phi, \qquad f_2 = jk_0 \sin \theta \sin \phi$$

$$F_1 = \cos(m\pi) \exp\left(f_1 \frac{w}{2} \right) - \exp\left(-f_1 \frac{w}{2} \right)$$

$$F_2 = \cos(p\pi) \exp\left(f_2 \frac{\ell}{2} \right) - \exp\left(-f_2 \frac{\ell}{2} \right)$$

$$f_m = f_1^2 + \left(\frac{m\pi}{w} \right)^2, \qquad f_p = f_2^2 + \left(\frac{p\pi}{\ell} \right)^2.$$

(4.55)

For the dominant rectangular TM(1, 0) mode, four $\boldsymbol{M}$ are presented in Fig. 4.5(b), and the far-field radiation patterns can be obtained from Eqs. (4.54) and (4.55) with $m = 1$ and $p = 0$ in the form:

$$E_\theta = -jKf(\theta, \phi) \cos \phi \left[\frac{\varepsilon_r - \sin^2 \theta}{\varepsilon_r - (\sin \theta \cos \phi)^2} \right]$$

and

$$E_\phi = jKf(\theta, \phi) \cos \theta \sin \phi \left[\frac{\varepsilon_r}{\varepsilon_r - (\sin \theta \cos \phi)^2} \right],$$

(4.56)

where $f(\theta, \phi)$ and K are given by the following definitions:

$$f(\theta, \phi) = \left(\frac{\sin(u)}{u} \right) \cos(v)$$

$$u = \left(\frac{k_0 \ell}{2} \right) \sin \theta \sin \phi, \qquad v = \left(\frac{k_0 w}{2} \right) \sin \theta \cos \phi$$

$$K = \left(\frac{V_0 k_0 \ell}{\pi} \right) \frac{\exp(-jk_0 R)}{R}.$$

(4.57)

Figure 4.7(b) and 4.7(c) show the spherical plots of the radiation pattern for the rectangular TM(1, 0) and TM(2, 0) modes, respectively.
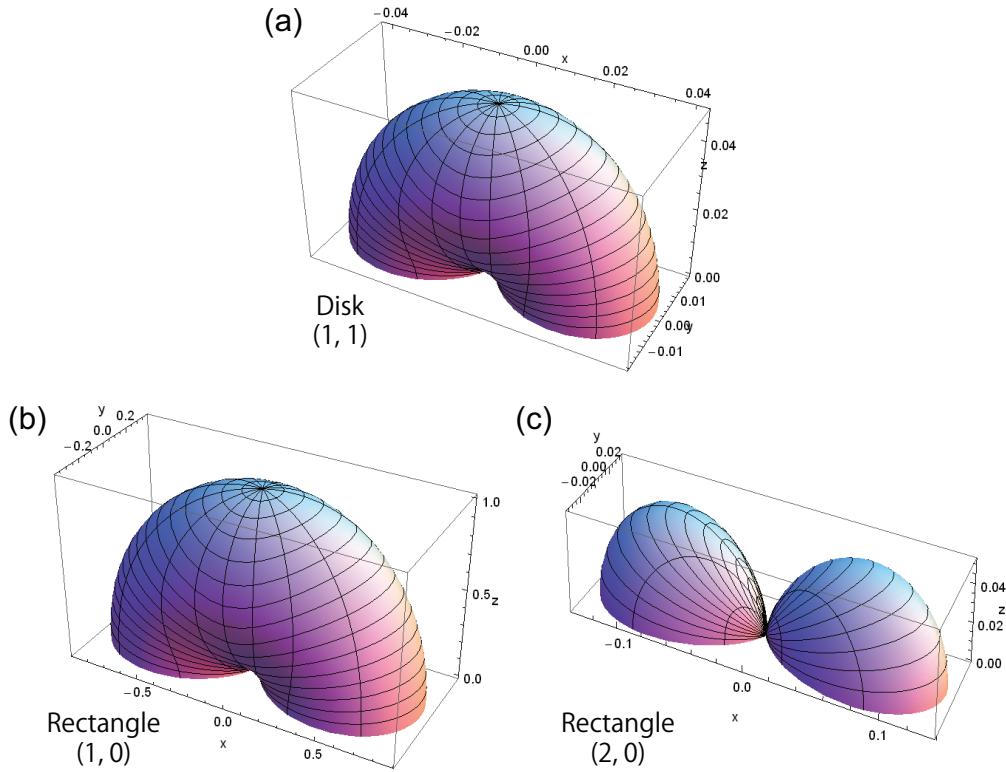
Figure 4.7: Spherical plot of the radiation patterns for the disk TM(1, 1) mode (a), rectangular TM(1, 0) mode (b) and rectangular TM(2, 0) mode (c).

4.3   Experimental results

4.3.1   Temperature dependence of the c-axis resistance

Figures 4.8(a) and 4.8(b) shows the bath temperature T dependence of the c-axis resistance for disk mesas D1, D2, and D3, and for rectangular (square) mesas S1, R1, and R4. For the measurement of these R-T curves, a DC current of 100 µA was applied to the mesa while cooling the sample holder at a rate of approximately 0.1 K per second. The obtained upturn curve suggests that the doping level of Bi-2212 adjusted by the annealing process is slightly underdoped. The superconducting critical temperature (T_c) and the transition width ΔT_c for each sample is summarized in Table 3.1. The c-axis resistivity ρ_c of Bi-2212, which can be estimated from the mesa dimensions: $R(\pi a^2/t)$ for disk mesas and $\rho_c = R(w\ell/t)$ for rectangular mesas, are consistent with the expected values for underdoped Bi-2212 [88].

It is interesting to note that the residual resistance exponentially increases as T decreases below T_c especially for D1, D2, S1, and R4, which have relatively small mesa areas. This tendency was also observed for other samples used in this study, especially for the groove-type samples fabricated by using the FIB milling technique. Although the contact resistance cannot be completely removed from the obtained R-T data in the two-terminal measurement, the strong T dependence of R below T_c has to be avoided.

Here, the author proposes another model to explain the peculiar behaviors of R below T_c. Figure 4.9 shows the cross-sectional view of the groove-type sample. As can been clearly seen in Figs. 4.8(a) and 4.8(b), the exponential T dependence of R below T_c is quite similar to that above T_c, which implies that the residual resistance comes from the non-superconducting Bi-2212 part connected in series with the superconducting mesa. Hence, the author hypothesizes that a thin insulating barrier layer, which has almost the same composition as Bi-2212 but has different conduction property, was accidentally formed by the Gallium ion irradiation during the FIB milling process. Since the widths of the milled grooves were almost the same for each sample, the smaller the mesa area, the more the damaged layer affects its R-T property, resulting in the distinct upturn behavior of R below T_c for smaller mesa samples.
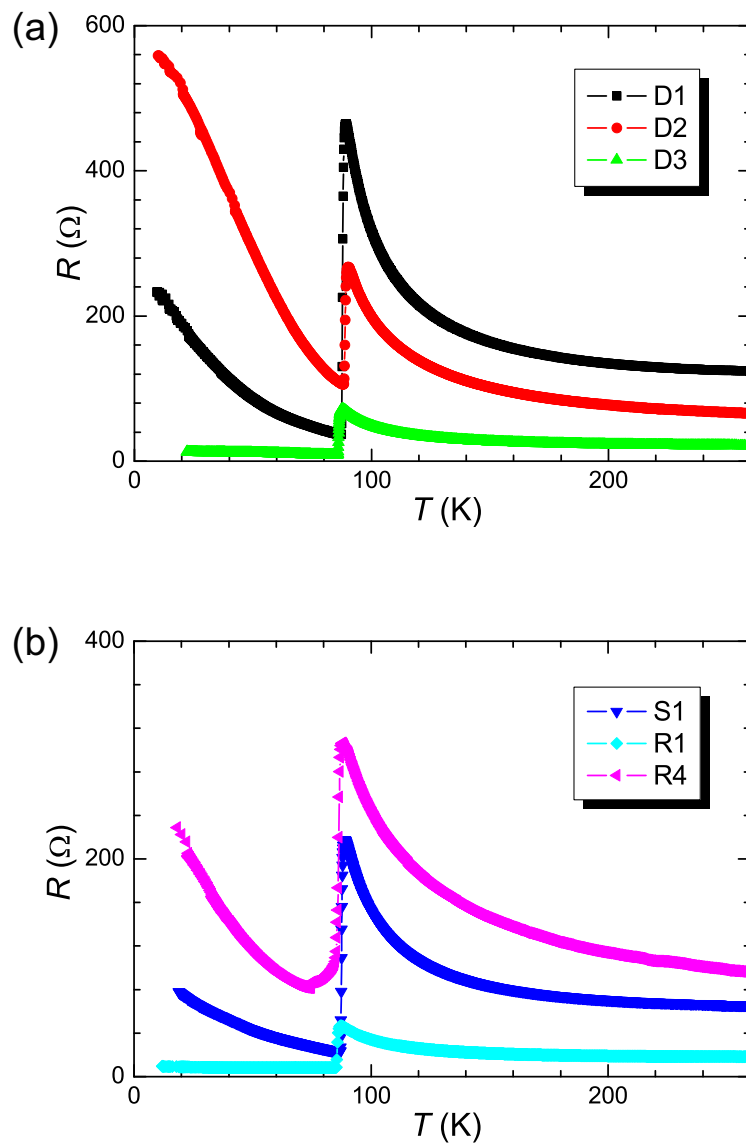
Figure 4.8: T dependence of the c-axis resistance.
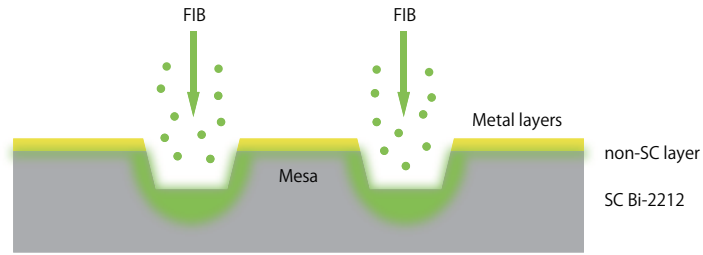
Figure 4.9: Cross-sectional view of the groove-type sample. A shaded green area indicates the non-superconducting (non-SC) part damaged by the Gallium ion irradiation.

4.3.2   Current-voltage characteristics and radiation property

Figure 4.10 shows a typical current-voltage (I-V) characteristics and radiation property for rectangular mesa R5. The bath temperature was set to be $T = 30.0$ K. As can be clearly seen, the intense radiation occurs in the return branch of the outermost I-V curve. Then, with decreasing the bias current, the radiation suddenly stops after an unexpected jump to another I-V branch.
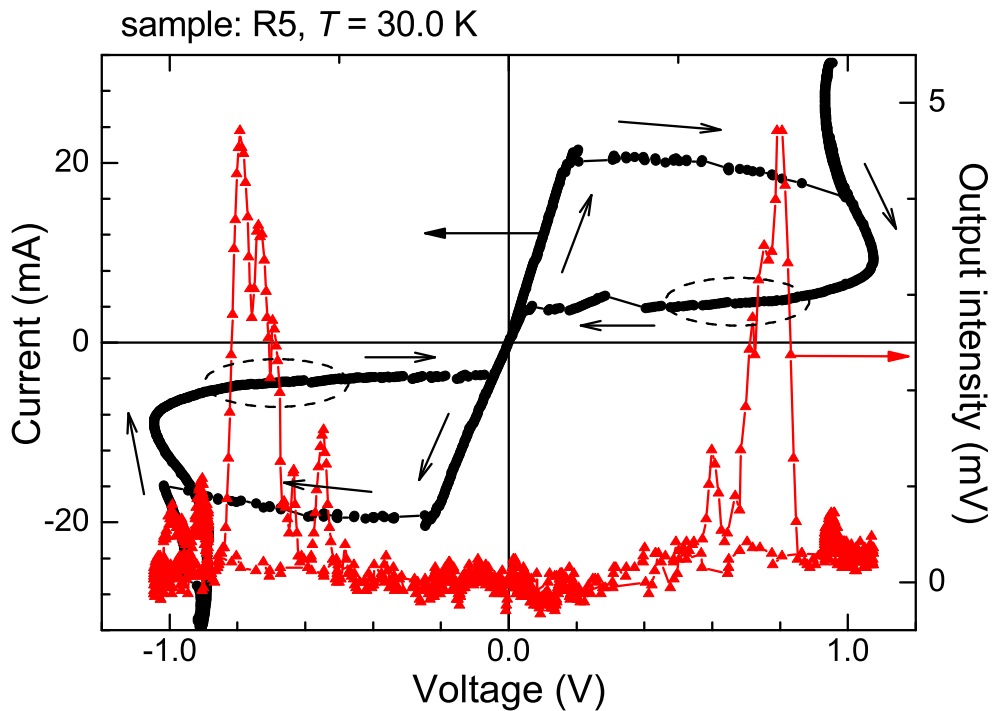
Figure 4.10: I-V characteristic (black symbol) and the detected radiation intensity from rectangular mesa R5 (red symbol) at $T = 30.0$ K.

Eight panels displayed in Fig. 4.11 also show the *I-V* characteristics and the radiation intensity for various samples. In Figs. 4.11(a-2), 4.11(b-2), and 4.11(c-2), the radiation regions are displayed in detail in an expanded scale. In most cases, the radiation was observed in a narrow *V* range, whereas in some cases, several intense emissions took place in a relatively wider *V* range at lower *I*. All samples that emit THz waves have a critical current density ranging between 50 and 200 A/cm^2.
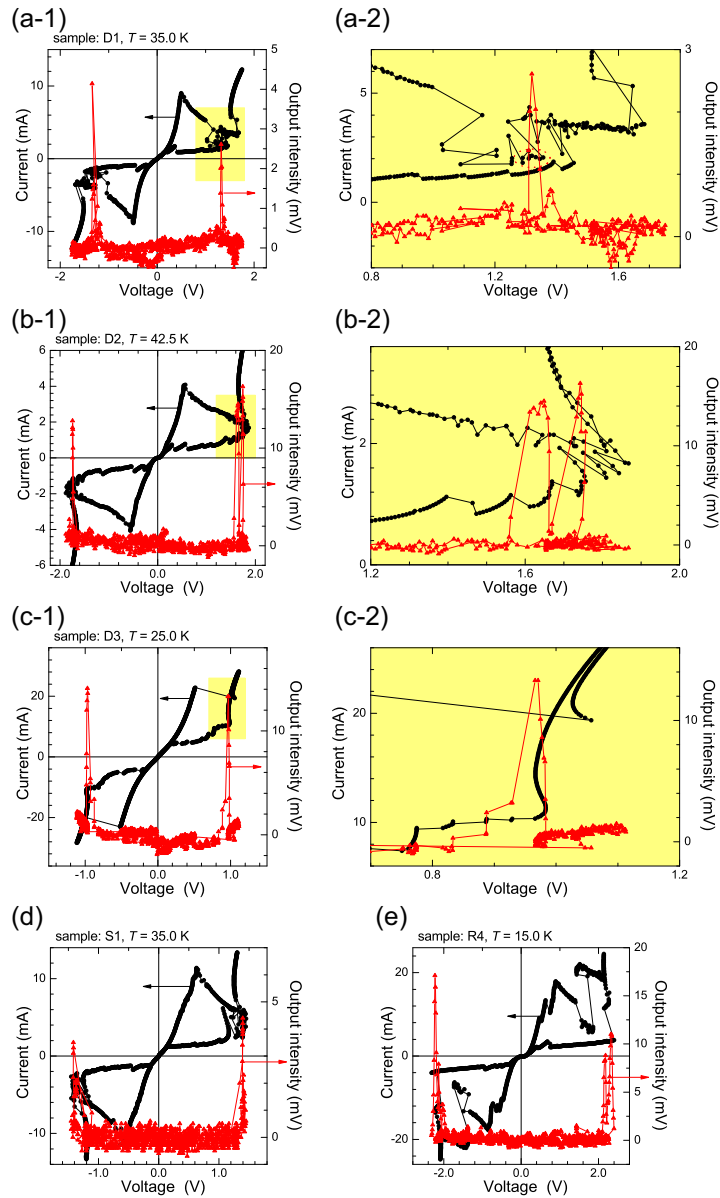
Figure 4.11: *I-V* characteristic and the detected radiation intensity for (a-1) D1, (b-1) D2, (c-1) D3, (d) S1, (e) R4, respectively. The shaded regions are displayed in detail in an expanded scale in Figs. 4.11(a-2), 4.11(b-2), and 4.11(c-2).

It is also interesting to note that the radiation usually occurs within a sample-dependent range of the bath temperature T. Figures 4.12(a) and 4.12(b) show the T-dependence of the normalized radiation intensity. The point we should emphasize is that the mesa temperature is much higher than the bath temperature T. For example, in the case of D3, since the constant $I \approx 11$ mA is fed into the mesa during the radiation, it is inevitably heated at a rate of about 11 mW, corresponding to the enormous heating power density of 8.3 kW/cm^3. This huge heating power cannot be removed quickly enough from the mesa, resulting in a considerable rise of the mesa temperature. This local heating may induce a chaotic nonequilibrium state and may adversely affect the THz radiation [73, 78, 82]. Also, since the heat conduction gets progressively worse at lower temperatures [89, 90] and the gap vanishes at T_c, this may account for the peculiar temperature dependence of the radiation intensity.
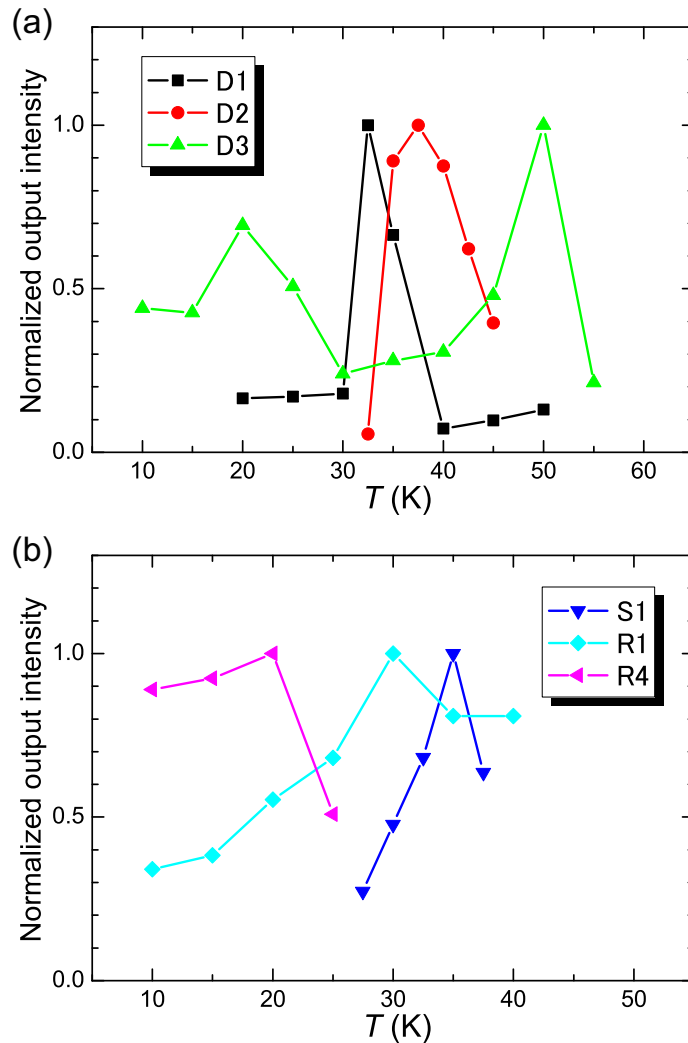
Figure 4.12: T dependence of the detected radiation intensity.

4.3.3 Far-infrared radiation spectrum

Figures 4.13(a) and 4.13(b) show the far-infrared radiation spectra obtained from three disk mesas and three rectangular mesas, respectively. Since the *I-V* ranges for obtaining radiation are almost invariant under the changes of T, all spectra presented here are particular to each radiating sample. The spectra clearly suggest that the radiation is monochromatic and quite stable over time. Although the spectral resolution of $\sim$7 GHz of the FT-IR spectrometer is not enough to discuss the radiation linewidth, in the previous study [12] the linewidth of below 0.5 GHz was separately obtained by a mixing technique.
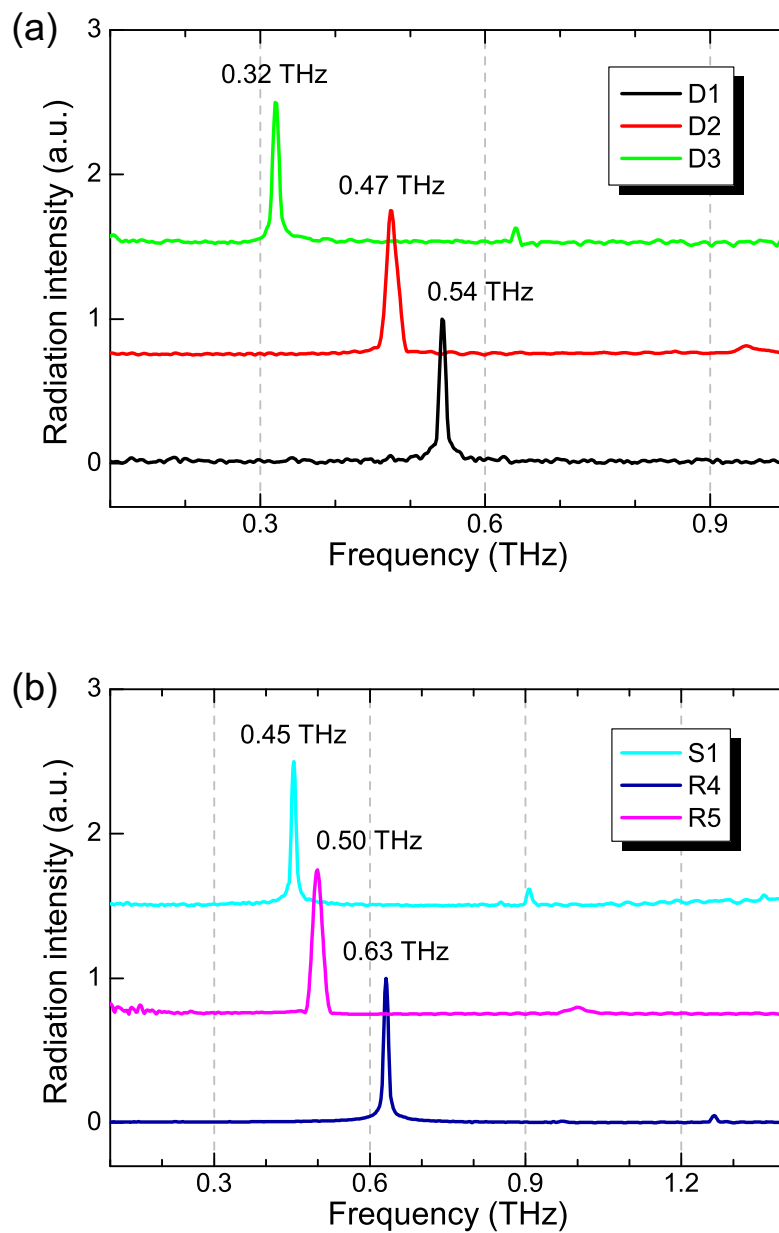
Figure 4.13: Far-infrared radiation spectra for disk mesas (a) and for rectangular mesas (b).

In this paper, the radiation frequency f is defined as the central frequency of the spectral peak. It is interesting to note that the second harmonic radiations at $2f$ are clearly visible. Theoretically, the second harmonic radiation from the disk mesa is easily distinguishable from that of the nearest higher disk cavity mode as discussed in detail later, providing unambiguous experimental evidence that the uniform part of the AC Josephson current is the primary radiation source.

4.3.4   Radiation from nearly-square mesas

The solid curve shown in Fig. 4.14(a) represents the outermost I-V characteristic branch at $T = 30$ K for R1 that has a nearly-square mesa geometry. In Fig. 4.14(a), the contact resistance mainly due to the two-terminal measurement is subtracted. Figure 4.14(b) shows the radiation power detected with the collecting optical system (see Fig. 3.7) as a function of I common to that of Fig. 4.14(a). In this particular sample, several radiation peaks are clearly observed between $I = 20$ mA and 5 mA. As indicated by the red and blue colors in Fig. 4.14(b), the bias current was scanned from $I = 35$ mA to 5 mA and in the opposite direction in order to confirm the reproducibility of the radiation.
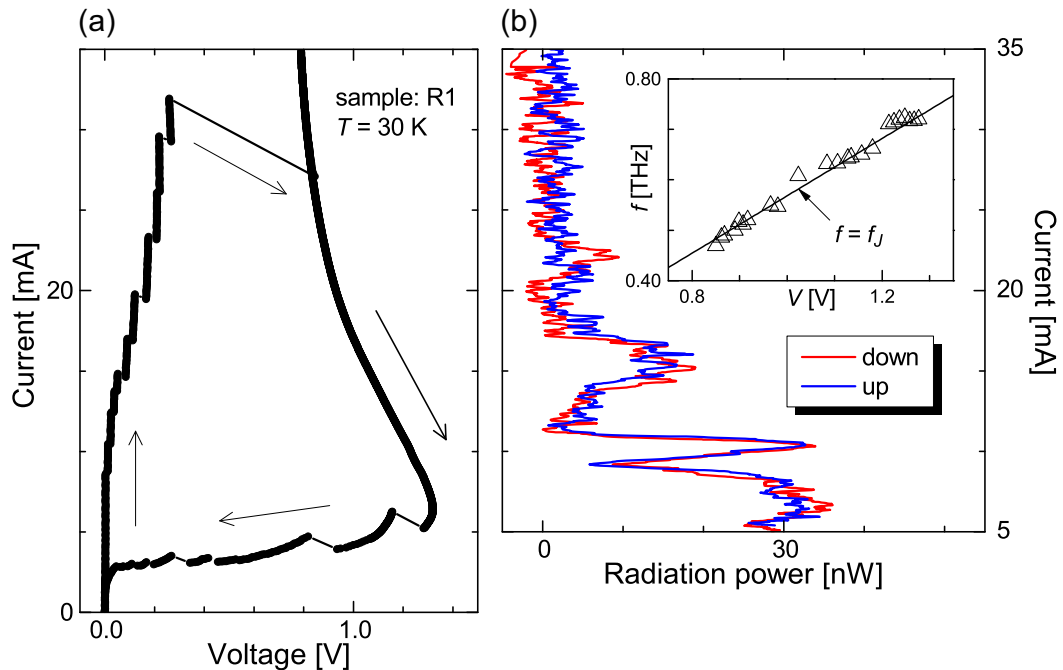
Figure 4.14: (a) I-V characteristics curve for sample R1 at $T = 30$ K. (b) Current I common to Fig. 4.14(a) versus the radiation power measured with the collecting optical system. The inset shows f measured by using the interferometer system versus V. The solid line represents the Josephson relation $f = f_J$ with $N_{\text{fit}} = 851$.

The inset of Fig. 4.14(b) displays the radiation frequency f measured by using the interferometer system. The solid line in the inset represents the Josephson relation: $f = f_J = (2e/h)V/N$, where $N = N_{\text{fit}} = 851$ is obtained by the least-squares fit to the experimental data. This N_{fit}-value is in good agreement with the value of $N_{\text{max}} = 850$, which can be separately estimated from the mesa height $t = 1.3$ µm of R1.

Figure 4.15 shows the bath temperature T dependence of the outermost I-V characteristic curve for sample R1. Since the c-axis tunnel resistance of Bi-2212 depends strongly on T (see Fig. 4.8), the hysteresis of the outermost I-V curve tends to be drastically suppressed as T increases.

Figures 4.16(a) and 4.16(b) show the T dependence of the radiation power as a function of V and I, respectively. In the figures, appropriate constant offset values are added to the experimental data for clarity. Note that the data presented here are cut out from the overall data obtained from the one-way I-V scan. It is interesting here to note that the radiation peak structures shown in Fig. 4.16(a) with respect to V are likely not to be sensitive to the change of T. We will discuss such a peak structure in more detail later.

Figure 4.17 shows the interference patterns for calibrating the radiation frequency f at each I-V point indicated by arrows in Fig. 4.16(a). In Fig. 4.17, the radiation intensities are normalized and aligned with different backgrounds. The solid lines represent the sinusoidal waves at the best fitted f_{cal} from the least-square fitting.
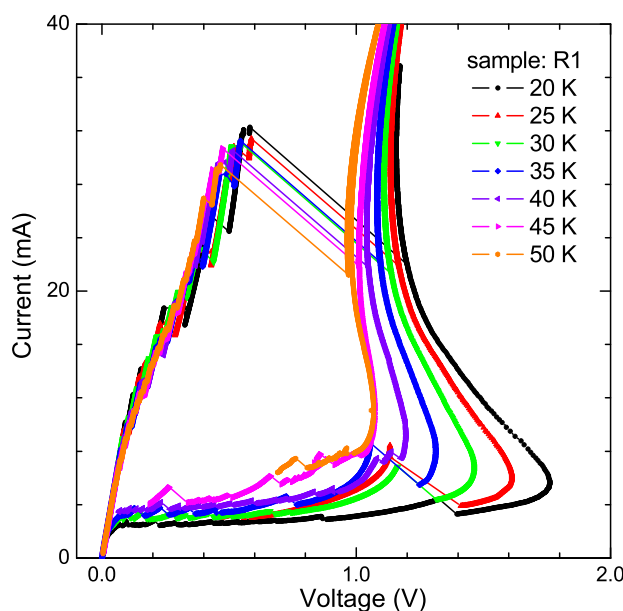
Figure 4.15: T dependence of the outermost I-V characteristic curve for sample R1.
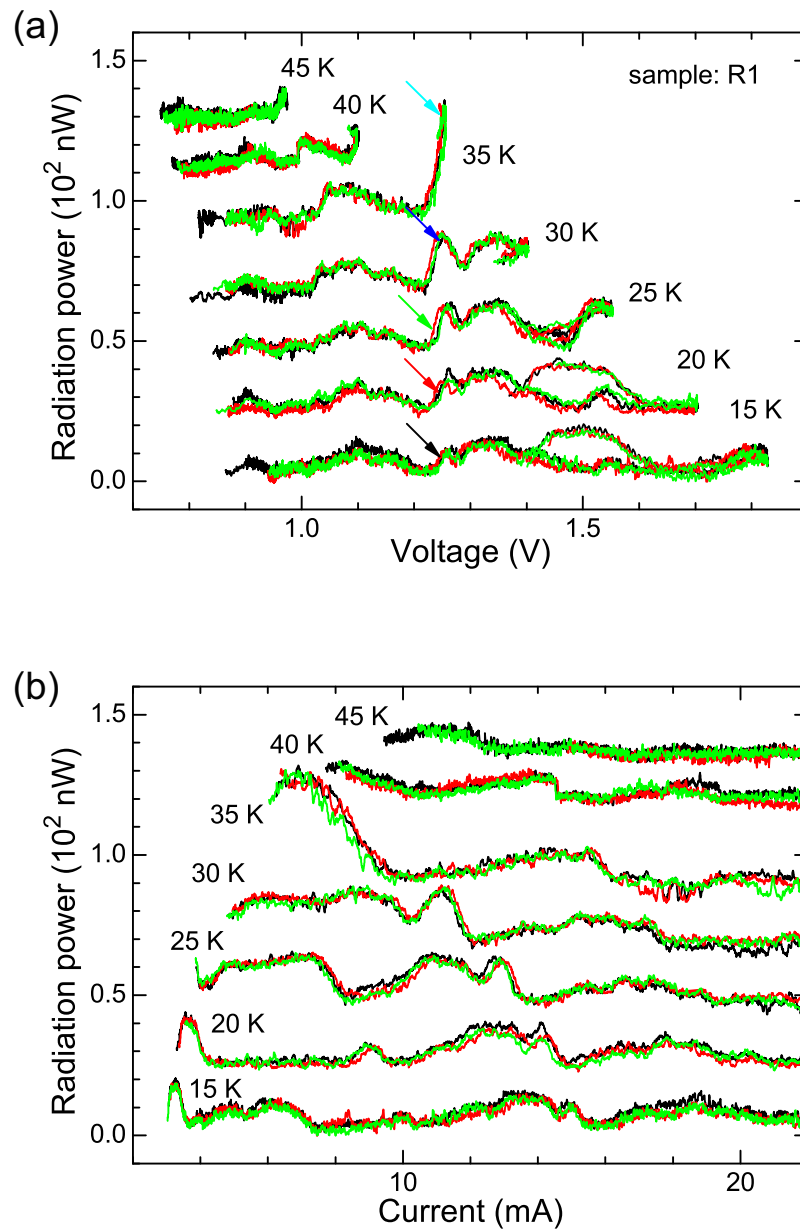
Figure 4.16: T dependence of the collected radiation power versus V (a) and I (b).
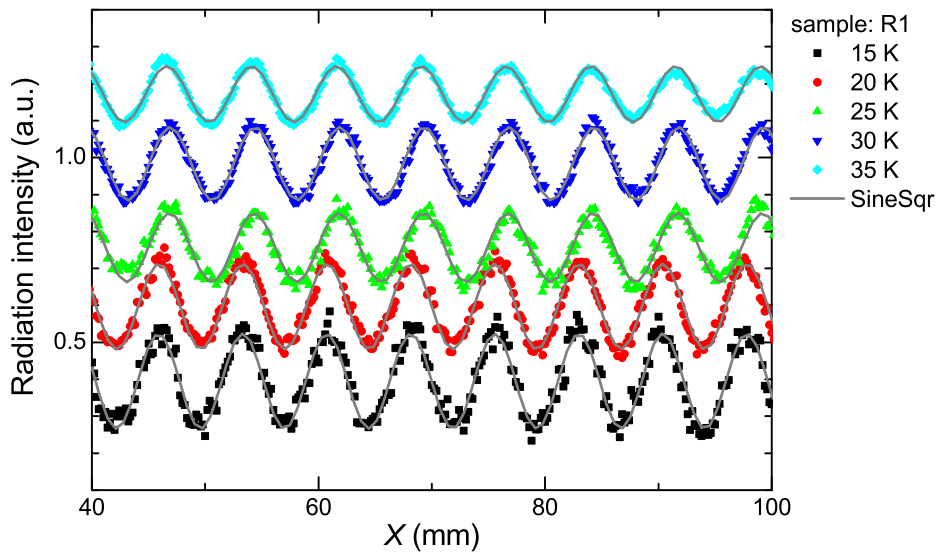
Figure 4.17: Interference patterns at the *I-V* points indicated by arrows in Fig. 4.16(a) measured by the interferometer system shown in Fig. 3.7. The solid lines represent appropriate fitting curves to the experimental data with $f_{\text{cal}} = 0.600$ THz (15 K), 0.603 THz (20 K), 0.603 THz (25 K), 0.570 THz (30 K), and 0.545 THz (35 K), respectively.

4.3.5 Spatial radiation pattern

Radiation pattern for the disk TM(1, 1) mode

Figures 4.18(a) and 4.18(b) show the spatial radiation patterns $P(\theta)$ for disk mesa D3 in two arbitrarily fixed planes, where θ denotes the detection angle (see Fig. 4.13). In order to confirm the reproducibility of the radiation, the bias current was cycled several times at each θ, as indicated by different symbol colors. Note that although the E and H planes are not able to be identified due to the axial symmetry of the disk geometry, the measured planes for Figs. 4.18(a) and 4.18(b) are perpendicular to each other. Since the radiation frequency of $f = 0.32$ THz was separately measured by the FT-IR spectrometer, it is confirmed that the disk TM(1, 1) mode is dominant and is excited during the radiation pattern measurement. The shadowing effect from the superconducting Bi-2212 crystal wall outside the groove is expected to be negligibly small in the first approximation.

In Fig. 4.18(a), the following characteristic features are noted: firstly, the radiation is strongly anisotropic, having a maximum around $\theta = \theta_{\text{max}} = 20$–$35°$ from the top ($\theta = 0°$), where a local minimum occurs with intensity ratio $P(20°)/P(0°) \sim 1.5$–2.0. This shallow minimum feature at $\theta = 0°$ is almost the same as for rectangular mesas as discussed later, although θ_{max} is somewhat less than the corresponding rectangular mesa value. Secondly, $P(\theta)$ rapidly diminishes as θ approaches $\pm 90°$. Clearly, the radiation pattern calculated by assuming the disk TM(1, 1) mode (see Fig. 4.7(a)) does not fit the experimental data, especially near to $\theta = 0°$, where $P(\theta)$ is a minimum. This disagreement can be removed by introducing a superposition of the radiation from the uniform AC Josephson current source

with the same Josephson frequency, or the influence of the finite Bi-2212 ground plane, as described in detail later.
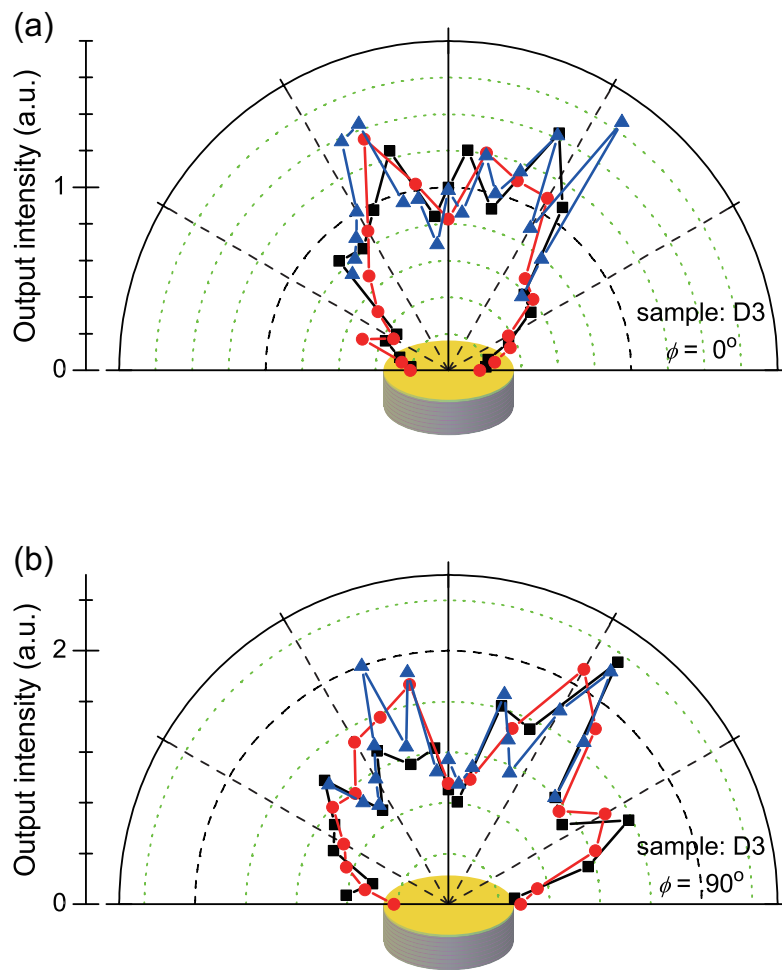
Figure 4.18: Spatial radiation patterns from disk mesa D3 in two arbitrarily fixed planes perpendicular to each other.

Radiation pattern for the rectangular TM(1, 0) mode

The radiation pattern $P(\theta)$ from rectangular mesas R5 and R6 in the E plane are displayed in Figs. 4.19(a) and 4.19(b), respectively. From the spectral measurements, the rectangular TM(1, 0) mode is confirmed to be excited similar to D3. The detected intensities $P(\theta)$ in these figures are normalized by the radiation intensity at $\theta = 0°$.

Similar to the radiation patterns from the disk mesa, the obtained patterns have considerable anisotropic characteristics in comparison with the ideal rectangular MSA. In Fig. 4.19(b), small but clear minor lobes are noticeable at $\theta \sim \pm75°$. These lobes might be caused by the higher harmonic radiation, though it seems to hardly contribute to $P(\theta)$ because of its weak power (see Fig. 4.13(b)). The MSA model predicts that the radiation intensity $P(\theta)$ for the rectangular TM(1, 0) mode should reach a certain maximum value at $\theta = 0°$, as presented in Figs. 4.7(b-1). This contradiction between the theory and the experiment will be discussed in detail later in this chapter.
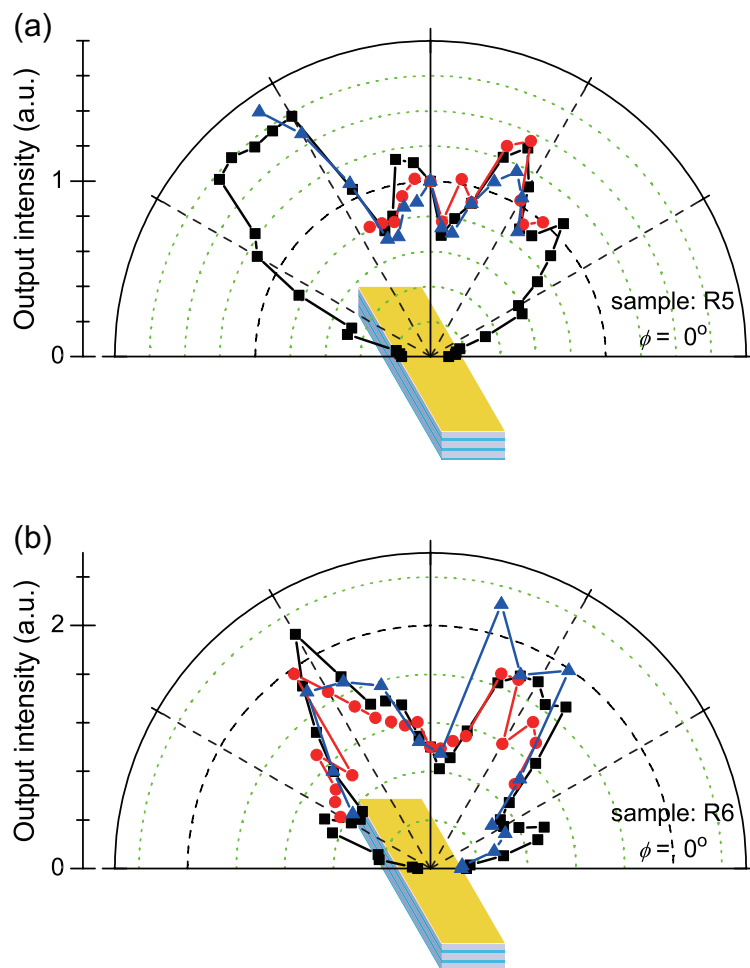
Figure 4.19: Spatial radiation patterns from rectangular mesas R5 and R6 in the E plane.
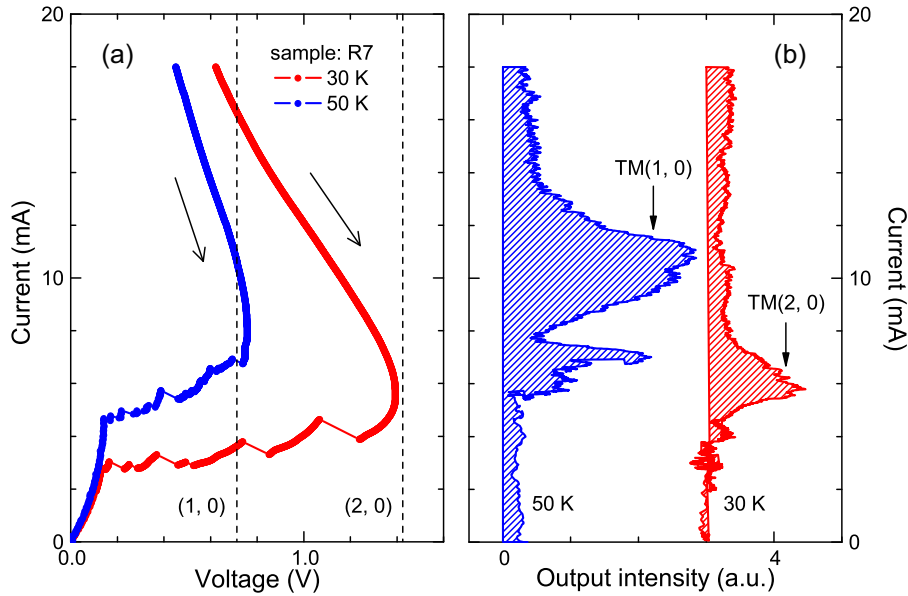
Figure 4.20: (a) *I-V* characteristic curves and (b) the radiation output intensity at $T = 30$ K (red) and 50 K (blue) for rectangular mesa R7. The vertical dashed lines in Fig. 4.20(a) indicate the calculated resonance voltage for the TM(1, 0) and TM(2, 0) mode.

TM mode dependence of the radiation pattern

Figure 4.20(a) shows the *I-V* characteristic for R7 at $T = 30$ K (red) and 50 K (blue), while Fig. 4.20(b) represents the detected radiation intensity versus I. The radiation frequencies f of 0.40 THz (30 K) and 0.79 THz (50 K) are separately obtained by the spectral measurements, suggesting that the TM(1, 0) and TM(2, 0) modes are observed at 30 K and 50 K, respectively. From the least-square theoretical fit in the same manner as the inset of Fig. 4.14(b), the number of the resistive junctions N during the radiation was estimated to be $N_{\mathrm{fit}} = 873$. Then, the resonance voltages for TM(1, 0) and TM(2, 0) modes can be calculated to be 0.713 V and 1.425 V, respectively, as indicated by the vertical dashed lines in Fig. 4.20(a).

As clearly shown in Fig. 4.20(b), the intense TM(1, 0) mode radiation can be observed at the calculated resonance voltage. Although the radiation power decreased with decreasing I below 10.6 mA, the *I-V* point again reached the TM(1, 0) voltage and reentered into the radiation state. Then, in the low current region below 6.7 mA, the system suddenly jumped to the inner branch regions, where N decreases. Hence, the *I-V* condition for the radiation was altered and the radiation stopped with poor reproducibility.

On the other hand, since the resonance voltage for the TM(2, 0) mode radiation is slightly greater than the maximum voltage at $T = 30$ K, the intensity of the TM(2, 0) mode radiation reached its peak at the maximum voltage, and was almost symmetrical with respect to I. The observed TM(2, 0) mode radiation seems to be the same as a full-wavelength radiation [17], while in the present study we can switch from TM(1, 0) to TM(2, 0) modes and vice versa only by changing T.

In order to further investigate the TM(1, 0) and TM(2, 0) mode radiations, their spatial radiation patterns were measured in the E plane. Figures 4.21(a) and 4.21(b) show the radiation patterns for TM(1, 0) and TM(2, 0) modes in the E plane, respectively. The cyclic bias current was scanned twice at each detection angle θ in order to confirm the reproducibility of the radiation. The solid angle of the detector window was limited to be 2.4×10^{-2} sr for better angular resolution.
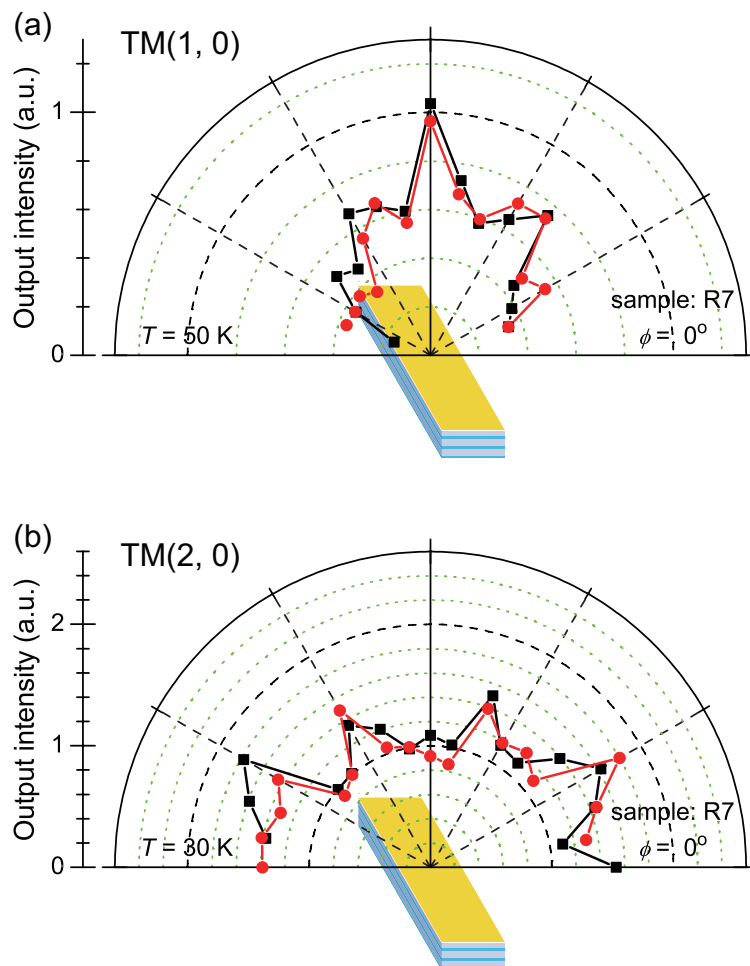
Figure 4.21: Spatial radiation patterns from R7 for rectangular TM(1, 0) and TM(2, 0) modes in the E plane.

4.3.6   Polarization property

A wire grid polarizer (Mutsumi Co., MWG40) which acts as a high-pass filter with a cutoff frequency of 0.75 THz was used in order to investigate the polarization property of the emitted THz wave. Figure 4.22 shows the detected radiation intensity from R1 versus the polarizer angle from 0° to 90°, where the polarizer angle is defined as the angle between the grid direction and the x axis, as sketched in the inset of Fig. 4.22. For example, when the polarizer angle is set to be 0°, the wire grid polarizer is placed parallel to the x axis. The detection angle θ was set to be $\theta = 60°$ in this measurement. From the spectral measurement, the rectangular TM(2, 0) mode at $f = 0.77$ THz is confirmed to be excited.

A dashed line in Fig. 4.22 represents the theoretical expectation given by the squared sinusoidal function with the assumption that the emitted THz wave is linearly polarized [5]. Then, the observed attenuation behavior of the radiation intensity is in good agreement with the expected situation that the emitted THz waves are linearly polarized with their electric field perpendicular to the CuO_2 planes. Theoretically, the radiation from the rectangular MSA is indeed expected to be linearly polarized.
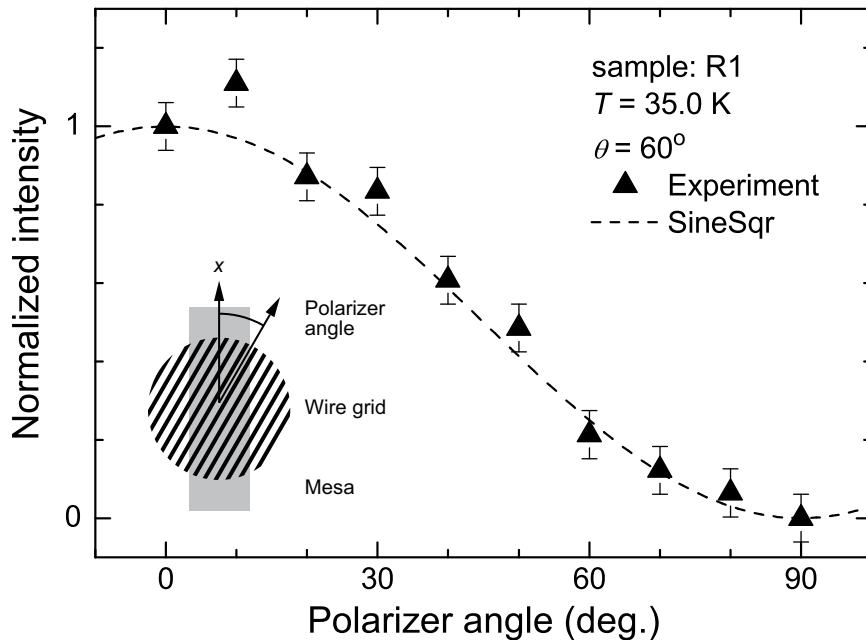
Figure 4.22: Polarization property of the emitted THz wave from R1. The inset presents the arrangement of the radiating mesa and the wire grid polarizer.

4.4 Discussion

4.4.1 Geometrical cavity resonance effect

Figures 4.23(a) and 4.23(b) show the mesa size dependence of the radiation frequencies f for the disk and rectangular mesas, respectively. The dashed lines represent the calculated cavity resonance frequencies given by Eqs. (4.27) and (4.43) in the form:

$$f = f_{11}^d = \frac{\chi_{11}c_0}{2\pi a \sqrt{\varepsilon_r}}, \qquad \text{(disk)} \tag{4.58}$$

and

$$f = f_{10}^r = \frac{c_0}{2\sqrt{\varepsilon_r}w} \qquad \text{(rectangle)} \tag{4.59}$$

Some extra data published in our previous studies [5, 36, 91] are also plotted in Fig. 4.23(b) for comparison.

In both mesa geometries, the data are in good agreement with the MSA model, suggesting that the Bi-2212 mesa structure can act as a MSA. Also, the dielectric constant $\varepsilon = 17.6$ can be obtained from a least-squares fitting and is consistent with the value that has been obtained in the previous studies [36]. Note that this ε-value is about 50% larger than that obtained from infrared spectroscopy [92]. It is also interesting to note that the second harmonic radiation at $2f$ seen in the radiation spectrum shown in Fig. 4.13(a) is easily distinguishable from those of the nearest higher disk cavity modes [15, 59, 60]. This experimental fact implies that the higher harmonic radiation may come from the non-linearity of the AC Josephson effect.

Theoretically, the fundamental TM modes with the lowest frequency are the TM(1, 1) and TM(0, 1) modes for disk and rectangular MSAs, respectively. Nevertheless, the rectangular TM(0, 1) mode was never observed in this experiment, whereas the disk TM(1, 1) mode is consistent with the experimental result. Since the mesa may be considerably heated by the DC current, it is very likely that the inhomogeneous heat distribution inside it prevents standing electromagnetic wave formation, particularly along the longer rectangular dimension. However, such hot spots with T even exceeding T_c first observed by Wang *et al.* [78] do not seem to be a problem for the geometrical cavity resonance conditions, since the fundamental frequencies of the disk and nearly-square mesas excellently obey the linear relation of the cavity frequencies with $1/a$ and $1/w$, respectively. Hence, the formation of electromagnetic standing waves may be restricted by other as yet undetermined reasons, and may not be excited below some cutoff frequency. The author proposes that this cutoff frequency may be the Josephson plasma frequency $f_p = c_0/(2\pi\sqrt{\varepsilon}\lambda_c)$, where λ_c is the c-axis superconducting penetration depth.

Figure 4.23: Size dependence of the radiation frequency f: (a) f versus $1/(2a)$ for three disk mesas. (b) f versus $1/w$ for rectangular (square) mesas, where some extra data published in previous studies [5,91] are plotted for comparison. The da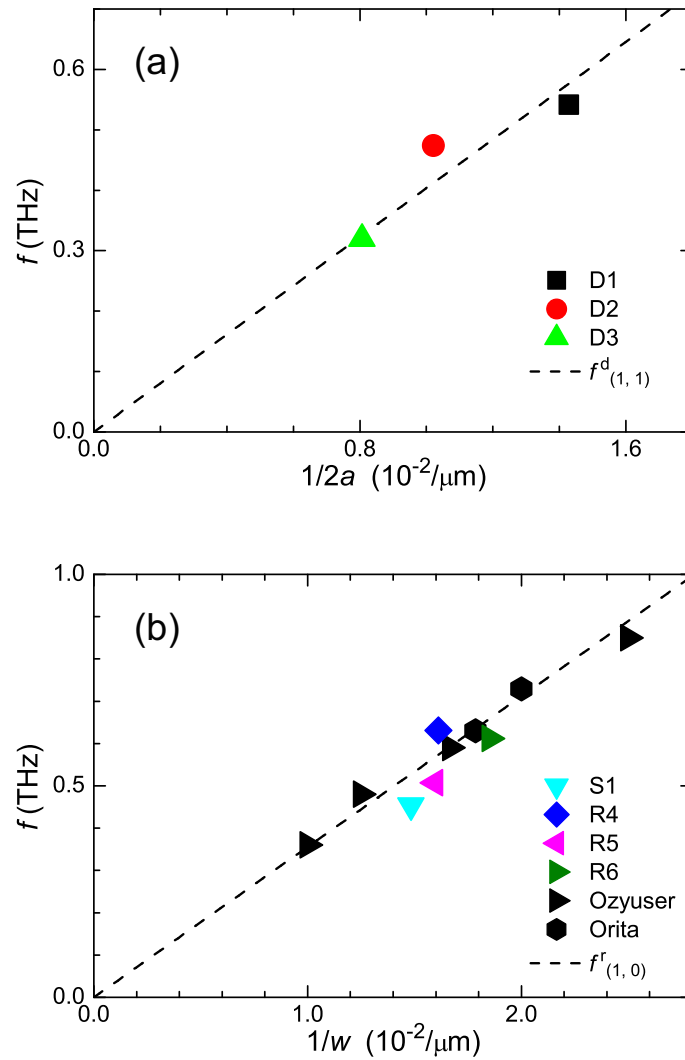shed lines represent the resonance frequencies f_{11}^d and f_{10}^r expected from the MSA model with $\varepsilon = 17.6$ as a least-square fitting parameter.

4.4.2 Higher-order cavity resonances

Figure 4.24 shows the detected radiation power from nearly-square mesa R1 measured at every 5 K from $T = 15$ K to 30 K. The data presented here are the same as that shown in Fig. 4.16(a). In order to confirm the reproducibility of the radiation, the bias current was decreased from $I \sim 35$ mA to 0 mA two times and increased once, as indicated by three different colors. Since the emitted TM waves were collected with the collecting optical system, the radiation power plotted here almost reflects the total radiation power, though the light losses due to the Fresnel reflections especially at the surface of the Si lens are not negligible. Although, in some cases, the intense radiation was observed in the low current region near $I \sim 10$ mA, where the number of resistive junctions N is inevitably reduced, we cut the data to make the figure clear. Note that there was no small step or excess current on the *I-V* curve during the radiation, which has been pointed out by some workers [5, 37, 84].

On the outermost *I-V* branch, we can estimate N from the Josephson relation: $f = f_J = (2e/h)V/N$, to be $N = N_{fit} = 851$. Then, by using this N_{fit}-value, we can again calculate the Josephson frequency f_J as indicated in the lower abscissa axis on Fig. 4.24. Here, six vertical dashed lines in Fig. 4.24 represent the cavity resonance frequencies f_{mp}^r for each rectangular TM(m, p) mode calculated from Eq. (4.35). As can be clearly seen, the radiation power has local maxima when $f = f_{mp}^r$, and their peak values vary depending on the excited TM mode; for instance, 33 nW for TM(2, 0) mode at $T = 30$ K. The TM(2, 0) radiation has a largest intensity among other modes, whereas its intensity diminishes as f_J becomes higher and lower. Also, each peak has a nearly symmetric shape with width δf that may reflect the quality of the cavity resonance, which is often represented by a Q-value ($Q = f/\delta f$). For instance, the Q-value for the TM(2, 0) mode at $T = 30$ K can be roughly estimated to be $Q = Q_c = f/\delta f = 710$ [GHz]$/26.1$ [GHz] $= 27$. Note that this value is much larger than that expected from the difference in top and bottom lengths of the actual mesa cavity due to the trapezoidal cross-section, typically $\sim 5\%$. This broadening effect of f strongly suggests that the fabricated Bi-2212 mesa structure acts as an imperfect MSA with a low Q-value. On the other hand, the radiation linewidth of the emitted EM wave has been separately measured by a mixing technique, which led to at least $\Delta f \sim 0.5$ GHz at 0.64 THz [12, 83]. Thus, another Q-value can be roughly calculated to be $Q_J = f/\Delta f = 640$ [GHz]$/0.5$ [GHz] ~ 1300, which is considerably larger than Q_c ($Q_J \gg Q_c$). This large Q_J-value giving rise to the narrower linewidth in spite of the imperfection of the internal mesa cavity is naturally interpreted by the synchronization effect in the intrinsic junction system. Further studies of the coherence of the system could provide supporting information.

In contrast to the long rectangular mesas, the calculated cavity frequencies f_{mp}^r of the nearly-square mesa ($w/L \sim 1$) lie close to each other. Indeed, in Fig. 4.24, at least five higher-order cavity resonances were clearly observed from a single *I-V* scan, enabling us to tune f in a wide range of approximately 30%. Hence, it can be simply said that the nearly-square mesa has an advantage in its broad tunability. In fact, the TM(1, 0) mode radiation that many workers have so far observed from the long rectangular mesas was a particular one among other possible modes observed from R1, and it has happened to be excited due

to the satisfaction of $f_J = f_{mp}^r$. Actually, we did not observe TM(1, 0) mode radiation from R1. Also, we emphasize that the primary mechanism of the radiation is nothing but the AC Josephson effect, because the radiation frequency never fails to satisfy the Josephson relation, even if the radiation takes place at an off-cavity frequency due to its low Q.

It is also interesting to notice that the peak structures shown in Fig. 4.24 are insensitive to the change of T. With increasing T, the *I-V* hysteresis was distinctly suppressed, because the gap voltage V/N of Bi-2212 considerably decreases with T as the quasiparticle tunnel resistance decreases [93]. Since the maximum voltage immediately decreases with increasing T, the higher-order resonances accordingly tend to disappear as T increases. This experimental fact implies that the effective sizes of the Bi-2212 cavity and the dielectric constant ε are not altered at all by changing T, which is inconsistent with the previous studies that point out the reduction of the effective size of the cavity with T [73, 78, 82]. Although the backbending *I-V* curves clearly indicate thermal nonequilibrium state due to considerable self-heating effect, it is unlikely that such nonequilibrium states, especially the hot spot, would have significant importance for the geometrical resonance conditions.
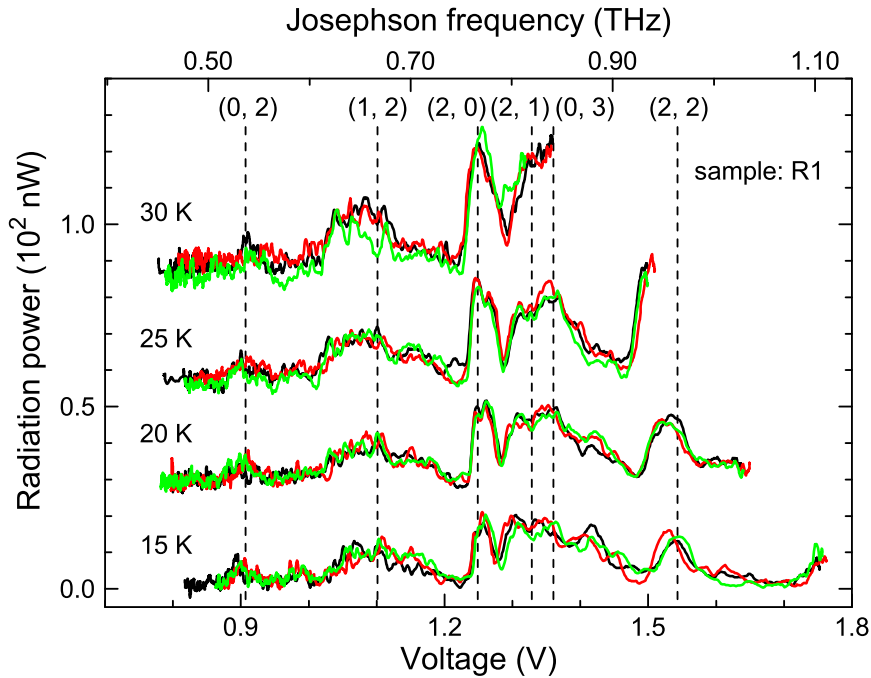

Figure 4.24: Higher-order TM radiations from nearly-square mesa R1. The Josephson frequency f_J on the upper abscissa is calculated from the Josephson relation with $N = N_{\text{fit}} = 851$. The vertical dashed lines represent the calculated cavity frequencies f_{mp}^r.

4.4.3 Dual-source mechanism

Figure 4.25 shows the radiation pattern for the disk TM(1, 1) mode from D3, which is the same data as that shown in Fig. 4.18(a). The dashed line in Fig. 4.25 indicates the calculated pattern from Eq. (4.56) by assuming radiation from the disk TM(1, 1) mode alone. Clearly, the calculated patterns do not fit the experimental data, especially near to $\theta_{\max} = 20$–$35°$. This disagreement can be removed by introducing a superposition of the radiation from the uniform AC Josephson current source with the same Josephson frequency [15, 59, 60]. A sketch of a disk mesa with a uniform $\boldsymbol{J}_S$ and a non-uniform $\boldsymbol{M}_S$ corresponding to the disk TM(1, 1) mode is presented in Fig. 4.26. Then, the experimental data are better fitted by this dual-source model with mixing parameter $\alpha = 1.44$ [15, 59, 60], corresponding to 58% of the radiation arising from the uniform AC Josephson current source, as shown by the solid orange curve in Fig. 4.25.

It is significant that the intensity from the uniform source is comparable to that of the fundamental cavity mode source, as in rectangular mesas [14]. Since the fundamental cavity mode radiation is enhanced by the cavity quality Q-value, a similar enhancement must occur for the uniform source radiation [53]. This suggests that the radiation from the uniform part of the AC Josephson current in the N junctions is coherent, amplifying the output by a factor of order N^2 [22]. This interpretation is strongly supported by the observation of only integral higher harmonics of the fundamental frequencies shown in Fig. 4.13(a). Neither higher disk cavity excitation frequencies of the Bessel type nor subharmonics were observed. The higher harmonics are naturally present in the entire AC Josephson current, the uniform part of which radiates coherently, but the nonuniform part of which can excite only one disk cavity mode. Hence, the radiation at higher harmonics arises solely from the uniform AC Josephson current source, but the larger intensity radiation at the fundamental frequency arises from both the uniform AC Josephson and nonuniform cavity sources. This experimental evidence clarifies unambiguously that the THz radiation is mainly generated by the uniform part of the AC Josephson current. Further studies of the polarization, coherence, and spatial radiation patterns of the higher harmonics could provide supporting information for these conclusions.

4.4.4 Influence of the finite ground plane

Figures 4.27(a) and 4.27(b) show the radiation patterns for the TM(1, 0) and TM(2, 0) modes from rectangular mesa R7, respectively. These data are the same as that already presented in Figs. 4.21(a) and 4.21(b). The dashed lines shown in 4.27(a) and 4.27(b) represent the radiation patterns for each TM mode in the E plane ($\phi = 0°$) calculated from the MSA model, while their three-dimensional plots are presented in Figs. 4.7(b-1) and 4.7(b-2).

The far-field electromagnetic fields ($\boldsymbol{E}, \boldsymbol{H}$) can be calculated by integrating the output fields emitted from the equivalent magnetic currents $\boldsymbol{M}$ along the open edge of the mesa. This assumption of linear $\boldsymbol{M}$ is reasonable when the mesa height t is much smaller than

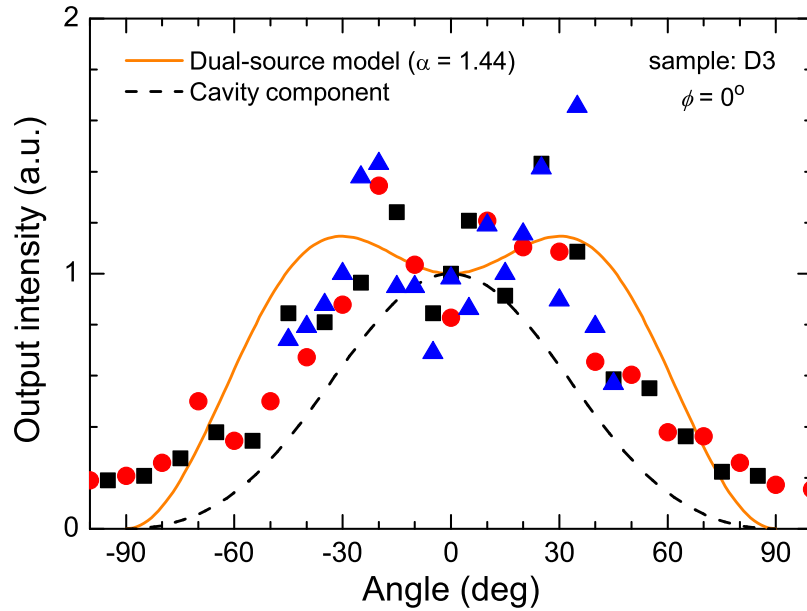Figure 4.25: Spatial radiation pattern for the disk TM(1, 1) mode from D3. The solid orange and dashed black curves are the best fits to the dual-source model and its cavity component, respectively.
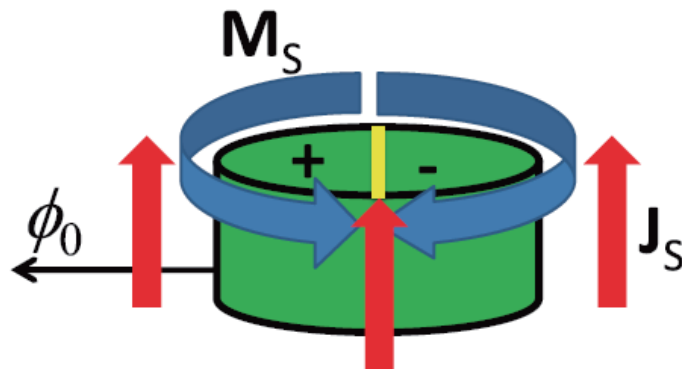

Figure 4.26: Sketch of a disk mesa with a surface electric current density $\boldsymbol{J}_S$ (red vertical arrows) and a magnetic current density $\boldsymbol{M}_S$ (blue horizontal azimuthal arrows). (copied from [60])

the wavelength λ: $k_0 t \ll 1$. Then, for the rectangular TM(1, 0) mode, since two in-phase magnetic currents $\boldsymbol{M}$ are the radiation sources (see Fig. 4.5(b)), the emitted electromagnetic field reaches a maximum at $\theta = 0°$. As to the E plane ($\phi = 0°$), the radiation power decreases only by 0.6 dB from the top to the lateral direction ($\theta = \pm 90°$), whereas it completely diminishes in the H plane ($\phi = 90°$). For the TM(2, 0) mode, since two antiparallel $\boldsymbol{M}$ act as radiation sources, the radiation power in the E plane ($\phi = 90°$) has the maximum at $\theta = 90°$ and zero at $\theta = 0°$, whereas there is no radiation in the H plane ($\phi = 0°$). Although these formulae could explain the obtained results shown in Figs. 4.27(a) and 4.27(b) qualitatively, especially for the local maximum values at $\theta = 0°$ for TM(1, 0) and at $90°$ for TM(2, 0), it seems to be far from sufficient to qualitatively understand the radiation patterns. Note that in the MSA theory, we did not take into account the influence of the surrounding structure, (*e.g.*, the Bi-2212 ground plane underlaying the mesa), which may vary the radiation characteristics in an important manner. Hence, it seems necessary to dispose of reliable tools to be able to describe these phenomena. One of the most effective theories is the geometrical theory of diffraction [94], which includes a method that gives accurate results with a simple formulation.

First, we assume a Bi-2212 mesa lying on a finite ground plane, as sketched in Figs. 4.28(a) and 4.28(b). The radiation is assumed to stem from the point Q_1. If this was not the case, for example, when the radiating source is modeled by arrayed mesas, we had to consider as many radiation sources as there are in the model. Then, L is the distance from the origin Q_1 to the edge of the Bi-2212 ground plane. This distance must be sufficient to have at the radiation point, a radiated field which behaves locally as a plane wave. Many experiments have shown that correct results are obtained for relatively small values of L ($L \approx 0.5\lambda$), but it is possible that this limit value varies with the type of antenna.

We are now looking at the E plane, and we consider that in this plane, the original radiation pattern from Q_1 is given by the MSA model. There are three rays which reach an observation point located at an infinite distance as shown in Fig. 4.28(b).

— R_1 is the direct ray: it will be linked to an incident field $\boldsymbol{E}_1$,

— R_2 and R_3 are two rays which are diffracted by the edges of the Bi-2212 ground plane. They will be respectively linked to the diffracted fields $\boldsymbol{E}_2(\theta)$, $\boldsymbol{E}_3(\theta)$.

We can then write the total field in the E plane in the form:

$$\boldsymbol{E}(\theta) = \boldsymbol{E}_1(\theta) + \boldsymbol{E}_2(\theta) + \boldsymbol{E}_3(\theta). \tag{4.60}$$

Since each vector has only one component in the direction of $\hat{\boldsymbol{e}}_\theta = \boldsymbol{U}_\theta$, where $\hat{\boldsymbol{e}}_\theta$ is a unit vector, the vector addition Eq. (4.60) is converted into a scalar addition:

$$\boldsymbol{E}(\theta) = [E_1(\theta) + E_2(\theta) + E_3(\theta)]\,\boldsymbol{U}_\theta, \tag{4.61}$$

where we have to determine each component $E_i(\theta)$; $i = 1, 2, 3$.

$\boldsymbol{E}_1$ is given by the radiation pattern in the E plane, and when the observation point is located at a great distance r, we have

$$\boldsymbol{E}_1(\theta) = F_{mp}^E(\theta)\,\frac{e^{-jkr}}{\sqrt{r}}\,\boldsymbol{U}_\theta, \tag{4.62}$$
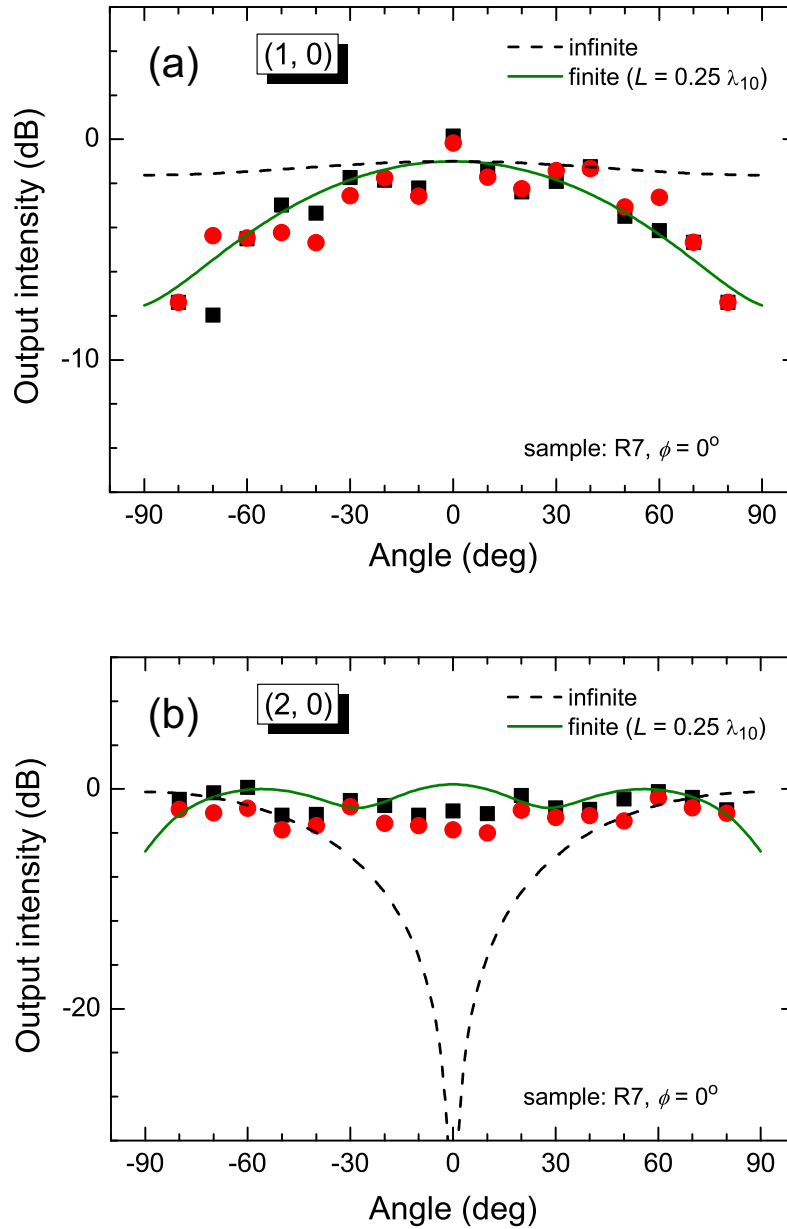
Figure 4.27: Radiation pattern for the rectangular TM(1 0) and TM(2, 0) modes in the E plane. The green solid and black dashed lines represent the calculated radiation patterns with a finite Bi-2212 ground plane ($L = 0.25\lambda_{10}$) and an infinite ground plane, respectively.
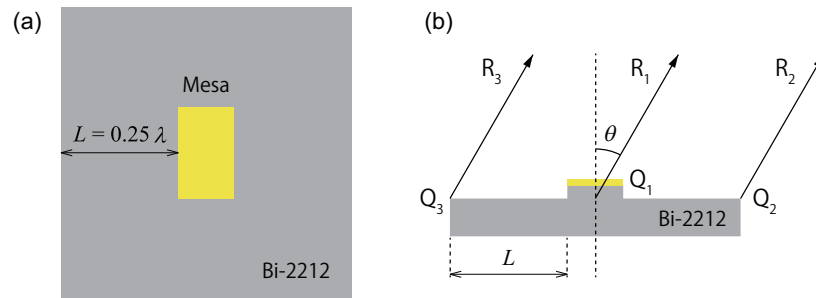
Figure 4.28: (a) Top view of the Bi-2212 mesa on a finite ground plane. (b) Incident (R_1) and diffracted (R_2, R_3) rays going to infinity.
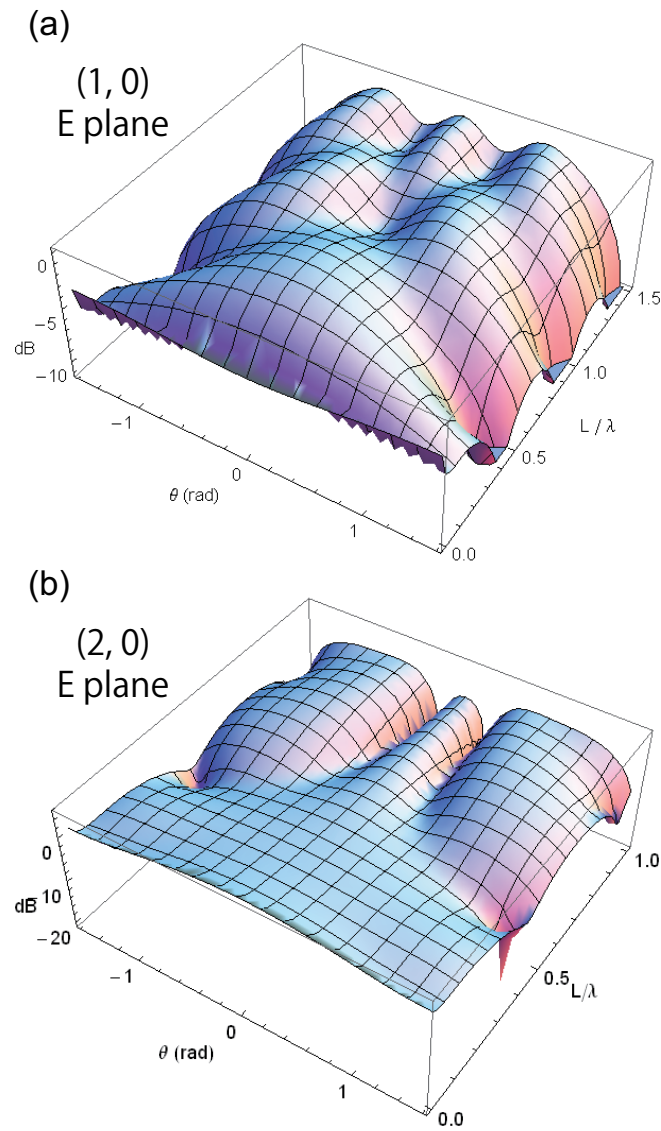
Figure 4.29: Three-dimensional plots of the calculated radiation patterns in the E plane with $\varepsilon = 17.6$ and $L = 0.25\lambda_{10}$.

where $F_{mp}^E(\theta)$ represents the radiation patterns of the mesa on an infinite ground plane. For the TM(1, 0) and TM(2, 0) modes, $F_{mp}^E(\theta)$ can be given from the MSA model (see Eq. (4.54)) in the form:

$$F_{10}^E(\theta) = \cos\left\{\frac{kw}{2}\sin\theta\right\} \tag{4.63}$$

and

$$F_{20}^E(\theta) = \sin\left\{\frac{kw}{2}\sin\theta\right\}. \tag{4.64}$$

Namely, the dashed lines in Figs. 4.27(a) and 4.27(b) represent $F_{10}^E(\theta)$ and $F_{20}^E(\theta)$ with $\varepsilon = 17.6$, respectively.

Since $\boldsymbol{E}_2(\theta)$ and $\boldsymbol{E}_3(\theta)$ are established in an identical manner, then it suffices to present the resolution of $\boldsymbol{E}_2(\theta)$. The incident field at the point Q_2 has the following value:

$$E_2(Q_2) = F_{mp}^E\left(\frac{\pi}{2}\right)\frac{e^{-jkL}}{\sqrt{L}}. \tag{4.65}$$

Using Sommerfeld solution and the method developed by Kouyoumjian and Pathak [95] to obtain a uniform solution in the vicinity of the geometrical optics boundaries, we obtain the diffracted field in the form:

$$\begin{aligned}E_2(\theta) = &-F_{mp}^E\left(\frac{\pi}{2}\right)\frac{e^{-jkL}}{\sqrt{L}}\\&\times \tilde{K}_-\left\{\sqrt{2kL'}\cos\frac{\phi_2}{2}\right\}\sqrt{L'}\frac{e^{-jk(r-L\sin\theta)}}{\sqrt{r-L\sin\theta}},\end{aligned} \tag{4.66}$$

with

$$L' = \frac{(r - L\sin\theta)L}{(r - L\sin\theta) + L} \qquad \text{and} \qquad \phi_2 = \frac{\pi}{2} + \theta \tag{4.67}$$

and

$$\tilde{K}_-(x) = \operatorname{Sgn}(x)\, e^{\,j(x^2+\pi/4)}\int_{|x|}^{\infty} e^{-jt^2}\,dt. \tag{4.68}$$

The observation point is located at a great distance r compared with L, we can do the approximation $L' = L$ and obtain

$$\begin{aligned}E_2(\theta) = &-F_{mp}^E\left(\frac{\pi}{2}\right)\, e^{-jkL(1-\sin\theta)}\\&\times \tilde{K}_-\left\{\sqrt{2kL}\cos\left(\frac{\pi}{4}+\frac{\theta}{2}\right)\right\}\frac{e^{-jkr}}{\sqrt{r}}.\end{aligned} \tag{4.69}$$

The other edge diffraction may be studied in an identical manner by collecting these three partial results, and we finally obtain the radiated field from the mesa on a finite Bi-2212

ground plane in the form:

$$E(\theta) = E_{mp}^E(\theta) = \left\{ F_{mp}^E(\theta) - F_{mp}^E\left(\frac{\pi}{2}\right) \right.$$

$$\times \left[e^{-jkL(1-\sin\theta)} \tilde{K}_- \left\{ \sqrt{2kL} \cos\left(\frac{\pi}{4} + \frac{\theta}{2}\right) \right\} + \right. \tag{4.70}$$

$$\left. \left. e^{-jkL(1+\sin\theta)} \tilde{K}_- \left\{ \sqrt{2kL} \cos\left(\frac{\pi}{4} + \frac{\theta}{2}\right) \right\} \right] \right\} \frac{e^{-jkr}}{\sqrt{r}}.$$

Figures 4.29(a) and 4.29(b) show the three-dimensional plots of the calculated radiation patterns $E_{10}(\theta)$ and $E_{20}(\theta)$ in the E plane, respectively.

Two green lines shown in Figs. 4.27(a) and 4.27(b) indicate the calculated radiation intensity by taking into account the influence of the finite Bi-2212 ground plane. Concerning the application of Eq. (4.70), we have searched the value of $L = 0.25\lambda_{10}$ which allowed to retrieve the experimental results with the best agreement. This value is in good agreement with the real value of $0.2\lambda_{10}$, but does not correspond exactly to it and often differs from a small fraction of wavelength (about $0.1\lambda_{10}$). We think that this small discrepancy is due to the following:

— the MSA theory is a very simple model which does not take into account the position of the feed point or dielectric losses,

— we do not take into account the influence of the groove formed around the mesa,

— the theoretical model is made in two dimensions, but the physical problem is evidently in three dimensions.

However, the maximum difference between theoretical and experimental results is very small (about 0.5 dB). Hence, we think that the proposed analysis is a good approximation, and that it gives a good idea of the fundamental phenomena of diffraction at the edges of the Bi-2212 ground plane.

4.5   Conclusions

In summary, we investigated the geometrical cavity resonance effect on the THz radiation from disk, square, and rectangular Bi-2212 mesas with various sizes. A new fabrication technique for making the groove-type sample using the focused ion beam milling was developed.

As expected from the MSA model, the mesa-shape dependence of the radiation spectra clearly demonstrates that the TM$(1, 1)$ and TM$(1, 0)$ cavity resonance modes are favorably excited for the disk and rectangular (square) mesas. More importantly, the second harmonic radiation seen in the radiation spectrum is easily distinguishable from those of the nearest higher-order cavity modes. This experimental fact implies that the higher harmonic radiation may arise from the non-linearity of the intrinsic Josephson effect.

The higher-order cavity resonances were also clearly observed from a nearly-square mesa by scanning the bias current at fixed T. This strongly suggests that the primary mechanism of the radiation is nothing but the intrinsic Josephson effect, because the radiation frequency always satisfies the Josephson relation, even if the radiation takes place at an off-cavity frequency due to the low Q.

From the spatial radiation pattern measurement, we observed the anisotropic pattern depending strongly on the excited TM mode. Then, we analyzed the data by introducing the dual-source mechanism [15, 59, 60] and the geometrical theory of diffraction [94], which enables us to take into account the influence of the Bi-2212 ground plane. In conclusion, it was revealed that the radiation pattern can be easily modified by the surrounding structure, such as electrodes, evaporated metal layer, Bi-2212 ground plane, *etc.*, because of the diffracted rays at their edges. Further studies using the mesa samples designed to systematically investigate the influence of the Bi-2212 ground plane will provide more detailed information about the diffraction effect.

Chapter 5

Tunable radiation from internal IVC branches

5.1   Introduction

The layered high transition temperature superconductor $Bi_2Sr_2CaCu_2O_{8+\delta}$ behaves as a stack of intrinsic Josephson junctions [1]. In Bi-2212, each of the intrinsic junctions is naturally identical, as they are evenly spaced with two junctions per unit cell c-axis length. Recently, continuous, coherent electromagnetic radiation was induced by applying a voltage across the stack of ~ 1000 junctions present in small mesas milled out of single crystalline $Bi_2Sr_2CaCu_2O_{8+\delta}$ [5]. Most workers have thought that the enhancement of the radiation intensity by the excitation of an internal cavity transverse magnetic mode, which is introduced in the last chapter, was so strong that the radiation from the AC Josephson current source alone was too weak to observe. However, recently the contributions to the radiation intensity from the AC Josephson current source alone and that enhanced by resonance with an internal electromagnetic cavity source were found to be comparable in magnitude [14]. Thus, this created a great deal of controversy.

In this chapter, we show clear evidence that the mesas can emit radiation at many frequencies, without strong interaction with an internal electromagnetic cavity resonance. Such a broadband tunability of the radiation frequency comes from the variation of the resistive states unique to the weakly-coupled intrinsic Josephson junction system, as described earlier in this chapter. More importantly, the resulting radiation is considerably tunable over a broad range of frequencies, allowing for the construction of a powerful device that could fill the terahertz gap.

5.2   Theoretical formulation

5.2.1   Phase dynamics of a single Josephson junction

RCSJ equivalent circuit

A Josephson tunnel junction which consists of two superconductors separated by a thin barrier layer exhibits hysteretic current-voltage (*I*-*V*) characteristics (IVCs). Namely, there exist two bias states; $V = 0$ and $V \neq 0$ at fixed I below the critical current I_c. On the other hand, point-contact or bridge-type junctions don't show the hysteresis but single-valued IVCs when the junction temperatures are not extremely lower than the transition temperatures (T_c's).

McCumber [96, 97], Stewart [98], and Johnson [99] individually pointed out that the weakly-linked junction can be equivalently described by the simple electrical circuit consisting of the resistance R, capacitance C, and the oscillation source as presented in Fig. 5.1 (resistively- and capacitively-shunted junction (RCSJ) model). Here, we consider the current-biased junction, because the junction impedance is sufficiently lower than that of the electric current source. Then, the equation that guarantees the current conservation for the RCSJ circuit is given in the form:

$$I = C\frac{dV(t)}{dt} + \frac{V(t)}{R} + I_c \sin\varphi(t), \tag{5.1}$$

where $CdV(t)/dt$ is the displacement current, $V(t)/R$ the Ohmic current, and $I_c \sin\varphi(t)$ the Josephson current. As Josephson predicted in 1962 [19], the junction voltage $V(t)$ is proportional to the time derivative of the superconducting phase difference $\varphi(t)$:

$$\frac{\partial\varphi(t)}{\partial t} = \frac{2eV(t)}{\hbar}. \qquad \text{(Josephson relation)} \tag{5.2}$$

Here, we should note that Eq. (5.1) can be applied only when $\varphi(t)$ is spatially uniform inside the junction. Then, Eq. (5.1) can be transformed into the following equation for φ:

$$I = \frac{\hbar}{2e}C\frac{d^2\varphi(t)}{dt^2} + \frac{\hbar}{2e}\frac{1}{R}\frac{d\varphi(t)}{dt} + I_c \sin\varphi(t). \tag{5.3}$$

In order to simplify Eq. (5.3), we introduce some non-dimensional parameters as follows [99]:

$$\tau = \omega_J t, \tag{5.4}$$

$$\beta = \frac{1}{\omega_J}\frac{1}{RC}, \tag{5.5}$$

and then, the normalized junction voltage $V(t)$ is given by

$$\eta(\tau) = \beta\frac{d\varphi}{d\tau} = \frac{V}{RI_c}, \tag{5.6}$$

where

$$\omega_J = \sqrt{\frac{2e}{\hbar}\frac{I_c}{C}} \qquad (5.7)$$

is the Josephson plasma frequency. By using these parameters, Eq. (5.3) can be transformed into the following equation:

$$\frac{I}{I_c} = \frac{d^2\varphi}{d\tau^2} + \beta\frac{d\varphi}{d\tau} + \sin\varphi. \qquad (5.8)$$

The point we should notice here is that we cannot solve this equation analytically except in the particular case that the second derivative in the right-hand side of Eq. (5.8) is zero or if $\beta = 0$.
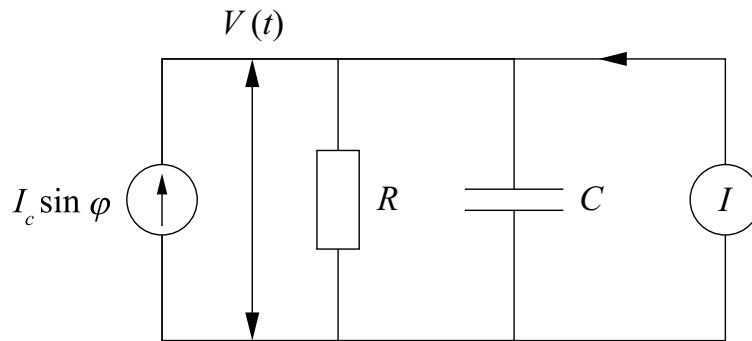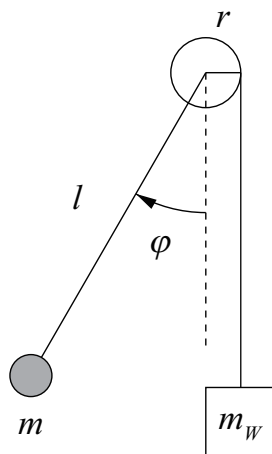

Figure 5.1: RCSJ equivalent circuit.

Figure 5.2: Mechanical model.

Mechanical model

Figure 5.2 presents the schematic view of the pendulum with damping. In Fig. 5.2, m, l, and φ represent the mass of the particle, the length of the string, and the angle between the string and the vertical line, respectively. The Newtonian equation for the pendulum is expressed in the form:

$$\tau_{\mathrm{T}} = M_{\mathrm{I}}\frac{d^2\varphi}{dt^2}, \tag{5.9}$$

where M_{I} denotes the moment of inertia. The total torque τ_{T} has three components: external torque ($\tau_a = m_W r g$), restoring torque ($-mgl\sin\varphi$) due to the gravity, and damping torque ($-D_{\mathrm{f}}\left(d\varphi/dt\right)$) due to friction. g and D_{f} represent the gravitational acceleration and damping coefficient, respectively. Then, we can obtain the concrete Newtonian equation in the form:

$$\tau_a = M_{\mathrm{I}}\frac{d^2\varphi}{dt^2} + D_{\mathrm{f}}\frac{d\varphi}{dt} + mgl\sin\varphi. \tag{5.10}$$

This equation has the same form as Eq. (5.3), suggesting that the mechanical model with a pendulum with a damping mechanism can be used for analyzing the dynamics of the superconducting phase difference of the Josephson junction. Such a theoretical analogy was first proposed by Anderson in 1963 [100].

Eq. (5.10) can be again transformed by using some non-dimensional parameters as follows:

$$\frac{\tau_a}{mgl} = \frac{d^2\varphi}{d\tau^2} + \beta_M\frac{d\varphi}{d\tau} + \sin\varphi, \tag{5.11}$$

where

$$\tau = \omega_M t, \tag{5.12}$$

$$\beta_M = \frac{D_{\mathrm{f}}}{\sqrt{M_{\mathrm{I}}mgl}}, \tag{5.13}$$

and

$$\omega_M = \sqrt{\frac{mgl}{M_{\mathrm{I}}}}. \tag{5.14}$$

If we assume $m \simeq 5$ g, $l = 9$ cm, $M \simeq m \times l^2$ as typical values, then $\omega_M \simeq 10$ s^{-1} can be calculated, and is approximately 10^9 smaller than ω_J ($\sim$GHz). This suggests that we can directly observe the time evolution of the non-linear oscillating behavior of the pendulum in some suitable demonstration experiments.

Current-voltage characteristic

When the parallel capacitance C is large enough to shunt the high-frequency AC Josephson current at the Josephson frequency $f_J = (2e/h)V$, the influence of the AC Josephson

effect on the DC IVC is very small. The condition for such an underdamped junction is empirically expressed as $\beta < 1.0$.

Figure 5.3(a) presents the IVC for a current-biased underdamped junction shown in the inset of Fig. 5.3(a). The bistable state in the range of $0 < I/I_c < 1$ gives rise to a quasiparticle IVC branch. From the analogy of the damping pendulum used in the mechanical model, on the zero-voltage branch ($V = 0$) the junction is pinned in the vicinity of the equilibrium position under the external torque, while on the quasiparticle branch ($V \neq 0$) the junction is rotating at a finite velocity given by the Josephson relation (5.2). Two right schematics in Fig. 5.3(a) represent the pinned (upper) and rotating (lower) states at bias points A, and B (C), respectively, as indicated in the left IVC.

As we increase the external DC current I from zero, the junction switches from the zero-voltage state (pinned mode) to the resistive state (rotating mode) at $I/I_c = 1$ discontinuously. Then, in the resistive state, the junction keeps on rotating unless the current I/I_c falls below the specific hysteresis parameter of $\alpha_c(\beta)$. Stewart pointed out that, in the case of the underdamped junction with $\beta < 0.2$, the hysteresis parameter $\alpha_c(\beta)$ can be approximately expressed as [98]:

$$\alpha_c(\beta) \simeq \frac{4}{\pi}\beta. \tag{5.15}$$

Figures 5.3(b) and 5.3(c) show the time evolution of the superconducting phase difference φ and its time derivative ($d\varphi/dt$) obtained by numerically calculating the differential equation (5.8) by using the fourth-order Runge-Kutta method with $\beta = 0.2$. In our calculation, the initial condition for φ is set to be $\varphi_0 = 0.1$, while $(d\varphi/dt)|_{t=0}$ is given the values from -0.1 to 0.6 in steps of 0.1 as shown in Fig. 5.3(c). The external DC current is set to be $I/I_c = 0.5$ at bias points A and B, and $I/I_c = 1.0$ at bias point C. We should note that the measurable DC voltage V corresponds to the time average of $d\varphi/dt$ in the equilibrium state.

In the limit of $\beta \to 0$, the approximate relation becomes exact. Then, the specific voltage V_m as a function of β can be theoretically estimated [99] as follows:

$$V_m(\beta) \leq RI_c\alpha_c(\beta). \tag{5.16}$$

By using Eq. (5.15), the above equation can be expressed as

$$V_m(\beta) \leq \frac{4}{\pi}\frac{\hbar}{2e}\omega_J, \tag{5.17}$$

where we use ω_J instead of β (see Eq. (5.5)). Fulton observed the ω_J dependence of the switching voltage V_m by using a tunnel junction [101]. Pedersen also measured the switching voltage of a tunnel junction consisting of Sn-SnO$_x$-Sn by changing β near to T_c [102]. They individually succeeded in obtaining ω_J-value and confirmed the relational expression of $V_m = (k\hbar/2e)\,\omega_J$, where $k \sim 1$ is the constant value of the first order of approximation.

In the above RCSJ model, we assumed that the Josephson current $I_c \sin\varphi$ can be considered separately from the quasiparticle tunnel current through the parallel R. In general, the
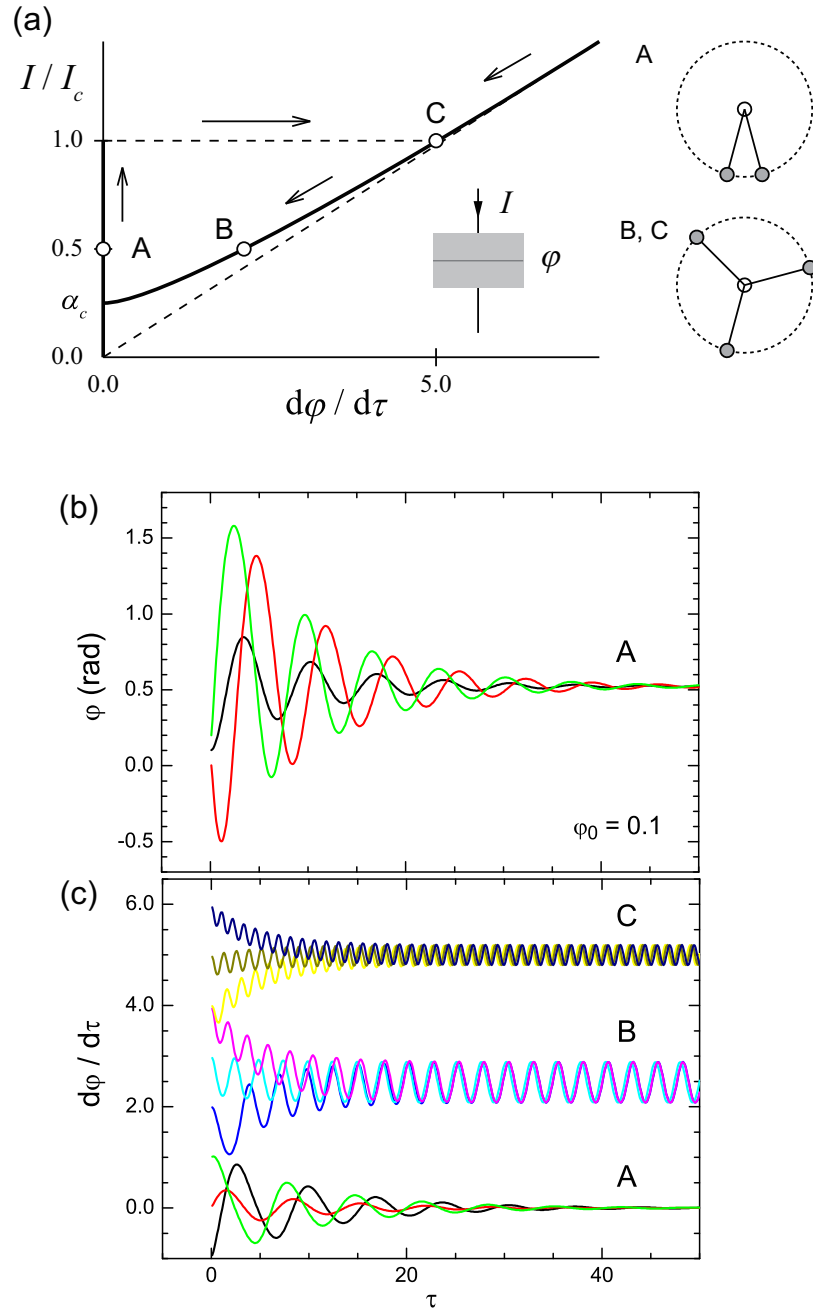
Figure 5.3: (a) Current-voltage characteristic (IVC) of the underdamped Josephson junction. The inset shows the schematic view of the Josephson tunnel junction. (b) and (c) Time evolution of the superconductive phase difference φ and its time derivative ($d\varphi/dt$) calculated by the fourth-order Runge-Kutta method with initial conditions $\varphi(0) = \varphi_0 = 0.1$ and $(d\varphi/dt)|_{t=0} = -0.1, 0, 0.1, \cdots, 0.6$.

microscopic expression regarding $I(t)$ that contains both superconducting and quasiparticle components can be written either as [103]:

$$I(t) = \lim_{\eta \to 0^+} \left\{ e^{\eta t} e^{\frac{-j\varphi(t)}{2}} \int_{-\infty}^{+\infty} dt' e^{-\eta t'} \left[e^{j\varphi(t-t')} S(t') + e^{\frac{-j\varphi(t-t')}{2}} R'(t') \right] \right\}. \quad (5.18)$$

or equivalently as,

$$I[\varphi(t)] = \int_0^\infty dt' \left[S(t') \sin \frac{\varphi(t-t') - \varphi(t)}{2} - R'(t') \sin \frac{\varphi(t-t') + \varphi(t)}{2} \right], \quad (5.19)$$

where $S(t)$ and $R'(t)$ represent the damping functions. The superconducting phase φ of the current-biased junction should obey the following differential equation:

$$I_{\text{DC}} = \frac{\hbar}{2e} C \frac{d^2\varphi}{dt^2} + I(\varphi), \quad (5.20)$$

where I_{DC} is the external DC current. Although we have taken into account the thermal fluctuation for calculating the actual IVCs in order to solve Eq. (5.20), we leave out the detailed explanation because of space limitations. (For references, see [103–106].)

5.2.2 Non-linear phase dynamics of the intrinsic junction system

Intrinsic Josephson effect

A series of high-T_c cuprate superconductors have been energetically discovered in previous works, which revealed that there exist superconducting CuO_2 double layers and an inserted block layer in the unit cell of their crystal structures. Such an anisotropic layered structure has been also considered to act as a natural stack of the atomic-scale Josephson junctions. In the case of $Bi_2Sr_2CaCu_2O_{8+\delta}$ (Bi-2212), each intrinsic junction is separated by a 1.533 nm interval, which corresponds to a half c-axial length of the unit cell.

A multiply-branched c-axis IVC of Bi-2212 shown in Fig. 5.4 is a convincing evidence to demonstrate the intrinsic Josephson effect [1]. After the first report of the intrinsic Josephson effect, many subsequent studies have been made to clarify that each branch is equally spaced by the uniform gap voltage and that the total number of branches is exactly equal to the number of intrinsic junctions in the stack. Such experimental facts are likely to be interpreted that the junction with a small I_c can preferentially switch from the zero-voltage state to the resistive state as being similar to the conventional multi-layered junction. That is, it could be said that the origin of the multiple IVC branches is the variation in the junction characteristics inevitably caused by the fabrication process, the non-uniformity of the single crystal, and so on. However, the non-linear phase dynamics of the intrinsic system based on the capacitively-coupled junctions will further provide a correct interpretation of the multi-stability of the system, as discussed in the following section.

Coupling mechanism

Since the junction size discussed here is sufficiently small, we can neglect the influence of the inductive coupling caused by the magnetic fields produced by the Josephson current and supercurrent [107]. Figures 5.5(a) and 5.5(b) display the schematic views of the stacks of multi-layered conventional junctions and intrinsic junctions, respectively. The point we should notice is that the thickness of the intrinsic superconducting layer s, for example $s \sim 0.3$ nm for Bi-2212, is comparable with the electric screening length μ of typically 0.2 nm. This suggests that the charge imbalance at the surface of the superconducting layer cannot be eliminated, causing capacitive coupling to the neighboring junctions. Such a charge fluctuation along the c-axis actually gives rise to the collective excitation of the longitudinal Josephson plasma mode [108]. Although the microscopic theory of the capacitively-coupled junction was developed by Koyama et $al.$ [109], in this chapter, we will introduce the phenomenological theory [35] based on classical electromagnetism because of space limitations.

Let us first introduce the Lagrangian that describes the superconducting phase dynamics of the one-dimensional intrinsic junction array in the form:

$$L = \sum_{l} \left\{ \frac{s}{8\pi\mu^2} \left(A_0^l + \frac{\hbar}{2e} \frac{\partial \varphi_{l+1,l}}{\partial t} \right)^2 - \frac{\hbar}{2e} I_c (1 - \cos \varphi_{l+1,l}) + \frac{\varepsilon D}{8\pi} E_{l+1,l}^2 \right\},$$

(5.21)

where s and D are the thicknesses of the superconducting and insulating layers, respectively. ε is a dielectric constant of Bi-2212. $E_{l+1,l}$ represents the electric field produced between the $(l+1)$-th and l-th superconducting layers. $\varphi_{l+1,l}$ is the gauge-invariant superconducting phase difference. The Lagrangian (5.21) consists of three components: the charging energy in the superconducting layer, the Josephson binding energy, and the electric field energy. The charge density in the l-th superconducting layer can be then expressed in the form:

$$\rho_l = -\frac{1}{s} \frac{\partial L}{\partial A_0^l} = -\frac{1}{4\pi u^2} \left(A_0^l + \frac{\hbar}{2e} \frac{\partial \varphi_{l+1,l}}{\partial t} \right).$$

(5.22)

The Lagrangian (5.21) leads to the Maxwell equations

$$E_{l+1,l} - E_{l,l-1} = \frac{4\pi s}{\varepsilon} \rho_l$$

(5.23)

$$I_c \sin \varphi_{l+1,l} + \frac{\varepsilon}{4\pi} \frac{\partial E_{l+1,l}}{\partial t} = 0.$$

(5.24)

By combining the time derivative of $\varphi_{l+1,l}$ and Eq. (5.22), we can obtain the relation between the electric field and the phase difference in the form:

$$\frac{\hbar}{2ec} \frac{\partial \varphi_{l+1,l}}{\partial t} = D E_{l+1,l} - 4\pi\mu^2 (\rho_{l+1} - \rho_l). \qquad \text{(Josephson relation)}$$

(5.25)

This equation suggests that even the universal Josephson relation has to be altered due to the capacitive coupling between neighboring junctions, which is represented by the first term on the right-hand side of the Lagrangian (5.21).
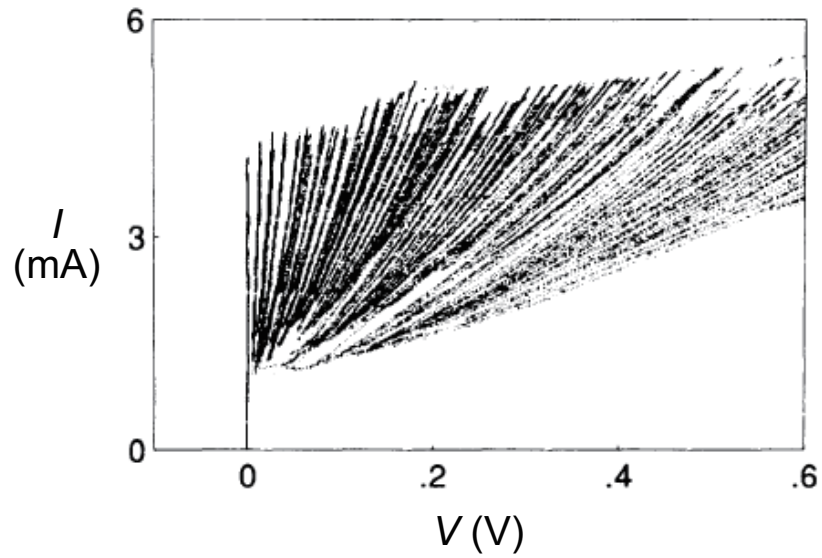
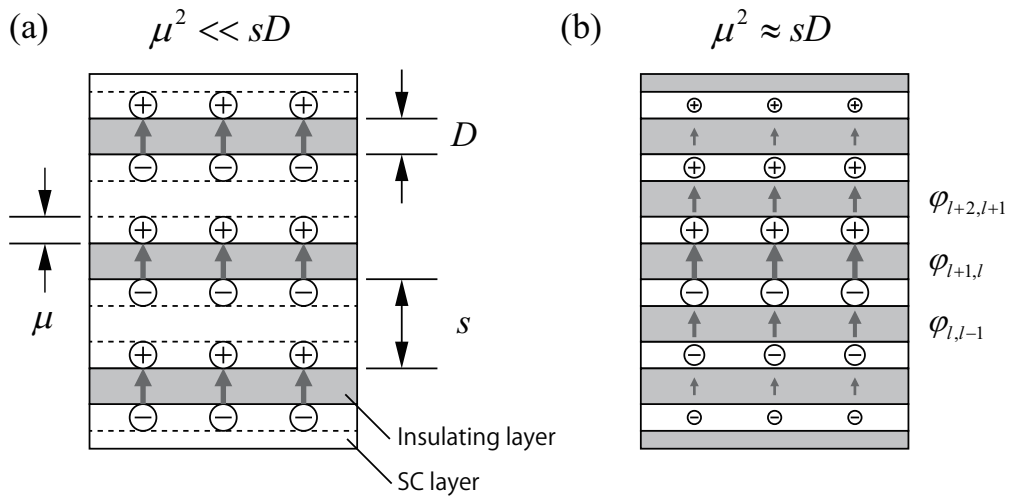Figure 5.4: c-axis multiple IVC branches of Bi-2212. (copied from [1])

Figure 5.5: Stacks of Josephson junctions: (a) conventional multi-layered junctions and (b) intrinsic junctions.

From Eqs. (5.23), (5.25), and linearized Eq. (5.24), we obtain

$$\frac{\varepsilon \lambda_c^2}{c} \frac{\partial^2 E_{l+1,l}}{\partial t^2} - \frac{\varepsilon \mu^2}{sD} (E_{l+2,l+1} + E_{l,l-1} - 2E_{l+1,l}) + E_{l+1,l} = 0. \tag{5.26}$$

This leads to plane wave solutions [108, 110] with the dispersion relation given by

$$\omega = \omega_{\mathrm{p}} \sqrt{1 + 2\alpha(1 - \cos k_z(s + D))}, \tag{5.27}$$

where $\omega_{\mathrm{p}} = c/\sqrt{\varepsilon}\lambda_c$ and $\alpha = \varepsilon \mu^2/sD$. Tachiki *et al.* pointed out the existence of the longitudinal Josephson plasma mode along the c-axis that has the plasma frequency gap ω_{p} [111]. Soon after their theoretical prediction, this novel Josephson plasma mode was experimentally confirmed by the microwave absorption experiments [112, 113].

Multiple current-voltage characteristic branch

By combining Eqs. (5.23), (5.25), and Eq. (5.8) in order to eliminate $E_{l+1,l}$, we obtain the following equation that describes the gauge-invariant phase dynamics of the intrinsic Josephson junction system:

$$\frac{1}{\omega_{\mathrm{p}}^2} \frac{\partial^2 \varphi_{l+1,l}}{\partial t^2} + \frac{\beta}{\omega_{\mathrm{p}}} \frac{\partial \varphi_{l+1,l}}{\partial t} + \sin \varphi_{l+1,l} =$$

$$\alpha \left(\sin \varphi_{l+2,l+1} - 2 \sin \varphi_{l+1,l} + \sin \varphi_{l,l-1} \right) + \frac{I}{I_c}, \tag{5.28}$$

where β is the damping parameter. This equation equivalently describes the non-linear dynamics of the coupled pendulum with the finite coupling parameter α, as shown in Fig. 5.6(a). It should be noted that this model reduces to that of the isolated pendulum in the limit of $\alpha \to 0$ (see Eq. (5.8)).

We can then obtain the multiply-branched IVCs of the intrinsic system by numerically calculating Eq. (5.28) under some proper initial conditions. Figures 5.6(b) and 5.6(c) show the schematic diagrams of the IVCs for weakly- ($\alpha \sim 0.1$) and strongly-coupled ($\alpha > 1.0$) junctions, respectively. The multiple IVC branches for the weakly-coupled system shown in Fig. 5.6(b) implies that each junction can individually switch into the rotating mode [1], whereas in the case of the strongly-coupled system shown in Fig. 5.6(c), there exists no multiple branch but several small steps on the return branch [114, 115]. Figure 5.7 shows the material dependence of the α-values for various high-T_c compounds [116, 117].

Figure 5.8(a) shows the numerically-calculated IVC branches for ten weakly-coupled intrinsic junctions under the periodic boundary condition with $\alpha = 0.1$ and $\beta = 0.2$ as typical values of Bi-2212 [35]. As we increase the bias current I/I_c from zero, the whole stack of intrinsic junctions simultaneously switches into the resistive state A at $I/I_c = 1$. Then, with decreasing I/I_c, the hysteresis IVC curve can be observed. The discontinuous behaviors in the lower current region indicate the instability of the rotating mode. In Figs. 5.8(b) and 5.8(c), we display the time evolution of the Josephson current $\sin \varphi_{l+1,l}$ for each individual junction at bias points B, C, and D, where some parts of the junctions are locally rotating
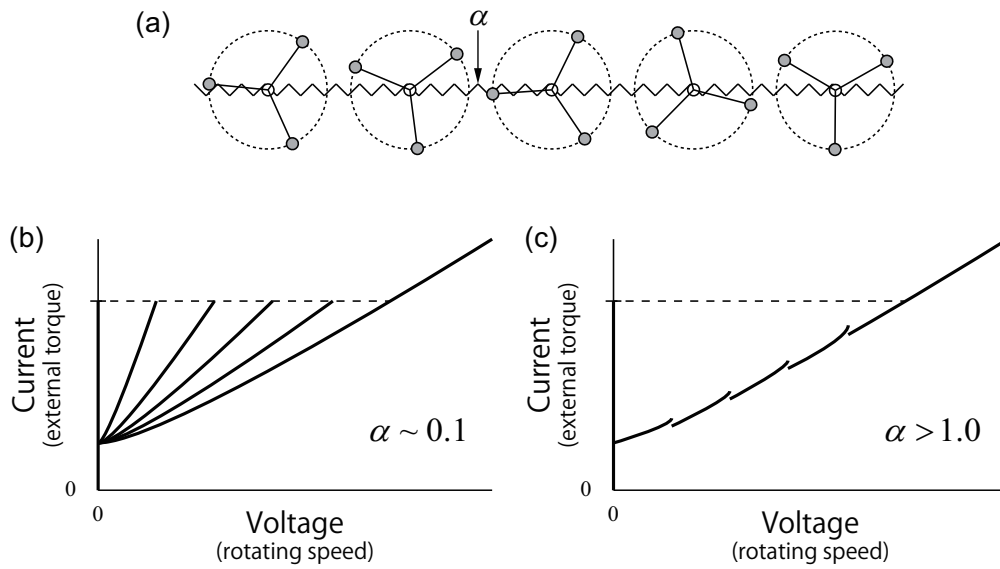
Figure 5.6: (a) Schematic view of the coupled pendulum with the coupling constant α. (b), (c) Multiple IVC branches for weakly- and strongly-coupled systems.
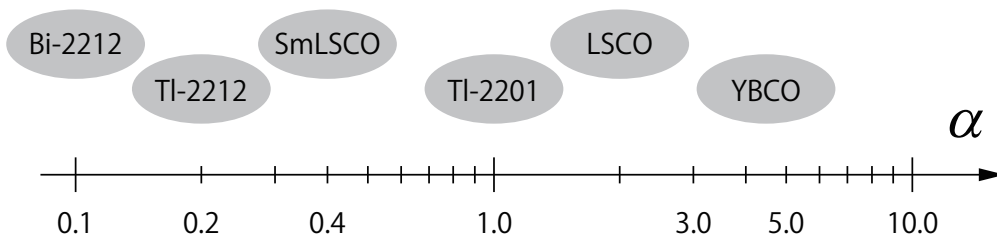

Figure 5.7: Material dependence of the coupling parameter α.

as indicated by the zigzag behaviors of $\sin \varphi_{l+1,l}$. Other junctions that oscillate with small amplitudes are pinned in the vicinity of the equilibrium position.

As a result of the repeated numerical simulation, it is also revealed that the system can switch into the various rotating modes which reflect the variety of the multi-stability of the intrinsic system. Figure 5.9(a) shows the simulation result with different current steps. The calculation result implies that in this narrow region there exist several bifurcation points depending strongly on the initial condition. Hence, in order to see all IVC branches, we performed the calculation many times with changing the current step and increasing the current as indicated by the arrow in Fig. 5.9(a). The obtained IVC branches displayed in Fig. 5.9(b) are composed of equally-spaced branches and the number of branches is equal to the number of junctions. These results indicate that Eq. (5.28) reproduce the multiple IVC branches without any inhomogeneities of the junction parameters. Concerning the stability of the localized rotating modes, this was studied by Takeno *et al.* in the context of the stability of localized whirling motions in coupled rotator models [118]. They showed that the bounded character of the trigonometric functions in the coupling terms is essential for the stability.

To understand the origin of the step-like transitions in the current decreasing process, it is necessary to note that the total driving torque on the right hand side in Eq. (5.28) is composed of two components, *i.e.*, the external current I/I_c and the Josephson currents at neighboring junction sites, $-\alpha\{\sin \varphi_{l+2,l+1} + \sin \varphi_{l,l-1}\}$, when the onsite term, $\sin \varphi_{l+1,l}$ is transposed to the left-hand side. Let us now consider the case in which both of the nearest neighbor $(l \pm 1)$-th junctions are in the pinned or rotating mode. In the former case, the total driving torque is very small, since the Josephson current shows tiny oscillations around the stable position. Thus, the total torque is almost equal to I/I_c. On the other hand, in the latter case, the minimum of the instantaneous driving current is given by $(I/I_c - 2\alpha)$, implying that the total torque is able to be instantaneously smaller than I/I_c. Hence, the switching into the pinned state is more likely to take place in the latter configuration than in the former one. From this point of view, one can conclude that the IVC branch switching in the low current region is caused by the capacitive coupling between neighboring junctions due to the inevasible charge fluctuation along the c-axis.

Non-linear phase dynamics of the intrinsic system and THz radiation

In the general lattice dynamics, there are two types of localized lattice motion: one is the localization due to the randomness which associated with the translation symmetry breaking of the lattice, especially in such a low-dimensional system. The other is the localization caused by the discreteness and non-linearity of the lattice system. The important point in the latter case is that such discreteness and non-linearity can give rise to the peculiar localized motion without having any randomness even in the perfect lattice system. During the last 30 years, spatiotemporal dynamics in non-linear lattice systems with many degrees of freedom has gained great interest because of their complicated spatiotemporal patterns and possible applications in many fields, such as turbulence, neural networks, biology, secure telecommu-
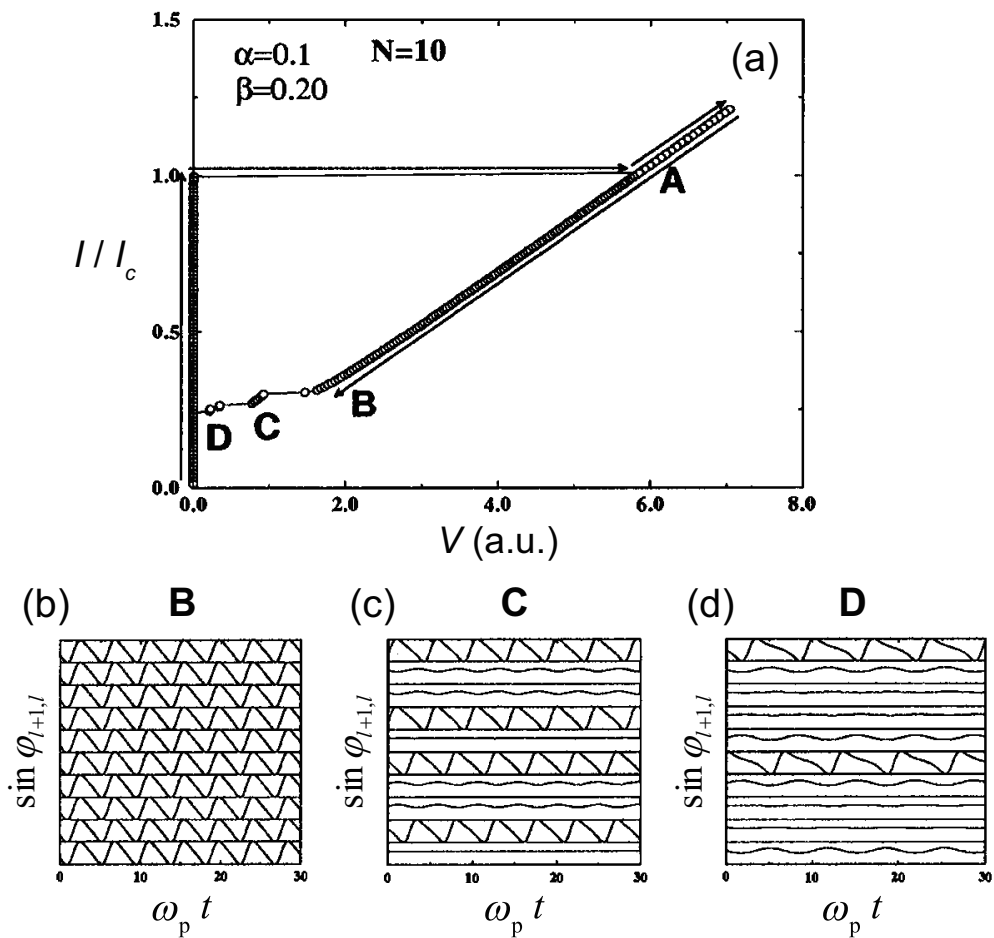
Figure 5.8: (a) IVC curve. Solid arrows indicate the scan direction of the external current. Time evolution of Josephson current $\sin \varphi_{l+1,l}$ at bias point (b) B, (c) C, and (d) D, respectively. (copied from [35])
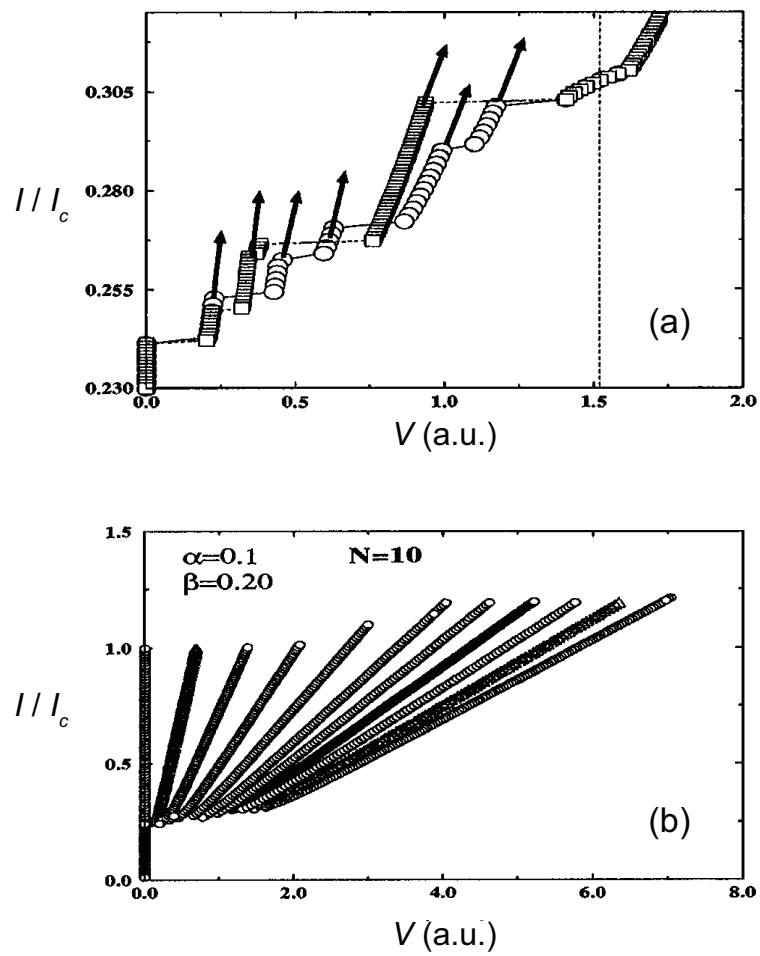
Figure 5.9: (a) The enlarged view of the IVC curve. (b) Multiple IVC branches obtained by the repeated numerical calculations. (copied from [35])

nications, spatiotemporal control of chaos, stochastic resonances, Josephson-junction lattice, *etc.* Recently, the damped dynamics of this model with harmonic coupling were numerically, theoretically, and experimentally investigated in relating to the fluxon dynamics of one-dimensional Josephson-junction arrays [119]. However, even today, it is still difficult to experimentally observe the localized non-linear lattice motion, because, in the actual system, the spatiotemporal scale of such localized motions caused by the coupling between neighboring (and at best next neighboring) lattices is typically in atomic scale, making it impossible to experimentally detect their non-linear motions.

A stack of intrinsic Josephson junctions naturally forming in the high-T_c cuprate superconductors can have a variety of coupling strengths represented by the coupling constant α, which ranges from 0.1 to 5.0 depending on the compound, as shown in Fig. 5.7. Furthermore, the atomic-scale intrinsic junction system is perfectly uniform as long as we have high-quality single crystals, such as Bi-2212. Actually, these days, a single crystal of Bi-2212 is relatively easy to obtain by various sorts of crystal growth techniques. Hence, it can be said that the stack of intrinsic Josephson junctions is an exceptional system to investigate the non-linear dynamics of the localized rotating lattice motion. In fact, in previous works especially on the Josephson vortex dynamics and on the Josephson plasma excitation in the intrinsic system, a lot of important results have been produced to reveal the non-linear phase dynamics of the intrinsic system. However, we still have some outstanding issues to discuss, because most experiments have the many-body problem that leads to the complicated picture of the intrinsic system.

With this background, we propose the terahertz (THz) radiation experiment as a tool to study the non-linear phase dynamics of the intrinsic junction system. In particular, we can excite each junction individually by scanning the multiple IVC branches, and can directly survey the quasi-stable state of the system by detecting the THz waves from the localized rotating junctions. Also, the emitted THz waves actually contain much important information about the coherence of the intrinsic system.

5.3 Experimental results

5.3.1 Radiation from the outermost branch

The hysteresis IVC loop indicated by arrows in Fig. 5.10(a) is typical of the outermost IVC branch of the intrinsic Josephson junction system. At the largest jump from $V = 0.25$ to 0.85 V, all of the $N_{\max}$ junctions switch into the resistive state simultaneously. Here, the number of the intrinsic junctions stacking in the mesa $N_{\max}$ can be estimated from the mesa height t; for example, $N_{\max} \sim 850$ for R1.

In the high-bias region, R1 is inevitably Joule heated at a rate of 16 mW. This huge power dissipation may cause the negative differential resistance between $I = 7$ and 25 mA, since the c-axis quasiparticle resistance R has a strong bath temperature T dependence as shown in Fig. 4.8. On the return region of the IVC loop near $I = 5$ mA, we observed several small
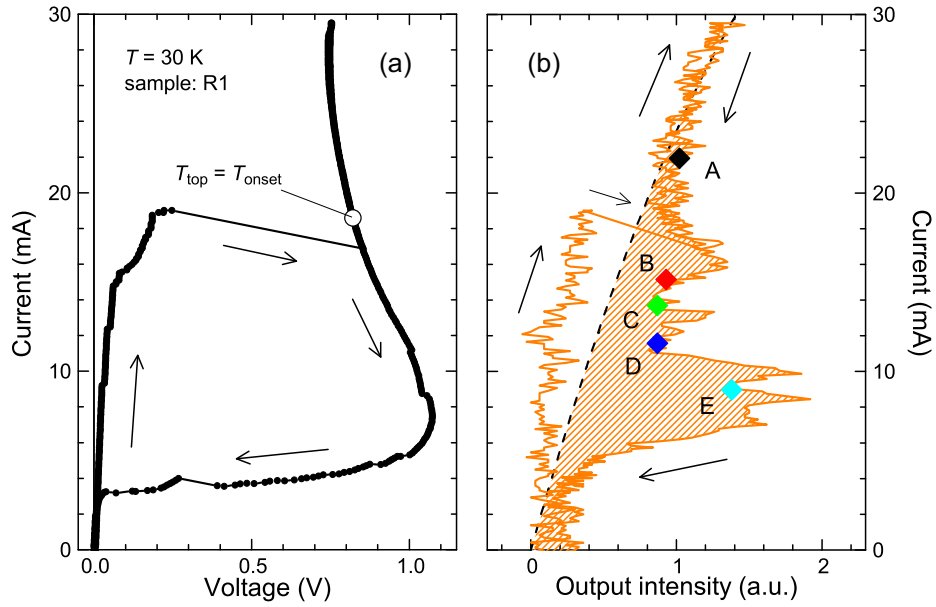
Figure 5.10: (a) Outermost IVC curve for R1 at $T = 30$ K. The open circle represents $T_{\text{top}} = T_{\text{onset}}$. (b) Current I on the same scale as in Fig. 5.10(a) versus the radiation intensity.
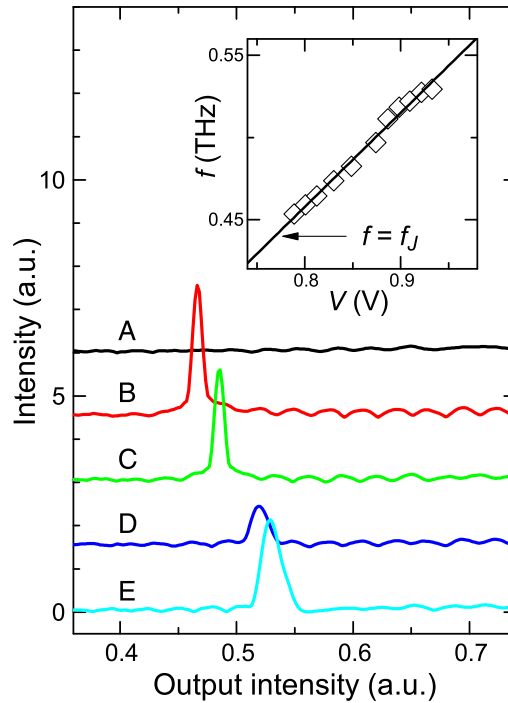

Figure 5.11: (b) Radiation spectra at bias points A–E indicated in Fig. 5.10(a) measured by the FT-IR spectrometer.

steps, indicating that some of the intrinsic junctions make the transition from the resistive (rotating) to the zero-voltage (pinned) state.

Figure 5.10(b) shows the radiation output intensity versus I on the same scale as in Fig. 5.10(a). The dashed curve indicates the expected drift due to thermal radiation from the sample and its holder. Soon after the largest jump in the IVC loop, intense radiation of electromagnetic waves was clearly observed. Since for R1, $T_c = 81.1$ K with a width $\delta T_c = 6.6$ K, R1 makes the transition to the superconducting state below $T_{\text{top}} = T_{\text{onset}} = 84.4$ K as indicated by the open circle in Fig. 5.10(a), where T_{top} is the spatial average of the temperature on the mesa top.

Figure 5.11 shows the radiation spectra at bias points A–E indicated in Fig. 5.10(b) measured by the FT-IR spectrometer. Each spectrum is offset for clarity. The narrow and intense peaks in the radiation spectra of B–E have maxima varying from 0.47 to 0.53 THz. The detector resolution-limited widths of the B and C peaks are too narrow to arise from synchronization by an internal TM cavity. Such f tunability of up to 40% on the outermost IVC branch was found previously by varying both V and T [17,73,74]. The inset of Fig. 5.11 shows that the Josephson relation for a stack of N_{max} junctions; $f = f_J = (2e/h)V/N_{\text{max}}$, is excellently obeyed as indicated in the inset of Fig. 5.11.

5.3.2 Radiation from the internal branch

We found that radiation also occurs at many bias points even in the inner region of the multiply-branched IVCs, where the number of rotating junctions N is fixed but different for each branch. In Figs. 5.12(b) and 5.13(b), the radiation frequencies f are plotted as color-scaled symbols on the high-bias regions for R1 at $T = 35.0$ K and R2 at $T = 52.5$ K, respectively, while Figs 5.12(a) and 5.13(a) show the full IVCs. For R1, all of the IVC branches shown in Fig. 5.12(b) bend backwards with increasing current, indicative of Joule heating. However, R2 is less susceptible to heating effects, and its IVC branches shown in Fig. 5.13(a) are monotonic. The radiation spectra were obtained at as many bias points as possible. At the bias points denoted by open diamonds, no emission was detected.

5.4 Discussion

5.4.1 Intrinsic Josephson effect

By repeated measurements of the radiation from a particular IVC branch with fixed N, we confirmed that f satisfies the Josephson relation: $f = f_J = (2e/h)V/N$. In Figs. 5.14 and 5.15, we replotted the emission data from the full IVCs of R1 and R2 shown in Figs. 5.12(b) and 5.13(b) in terms of $f(V)$, representing the data from each branch in terms of unique symbols and colors. By fits of the data for a particular branch to the Josephson relation with $N = N_{\text{fit}}$, the experimental best-fit value N_{fit} for each branch was determined. Three examples each for R1 and R2 are indicated by the dashed lines in Figs. 5.14 and 5.15,

Figure 5.12: (a) Full IVC branches for R1 at $T = 35.0$ K. (b) Multiple branches in the high-bias region of Fig. 5.12(a) and THz radiation at the color-coded frequencies.
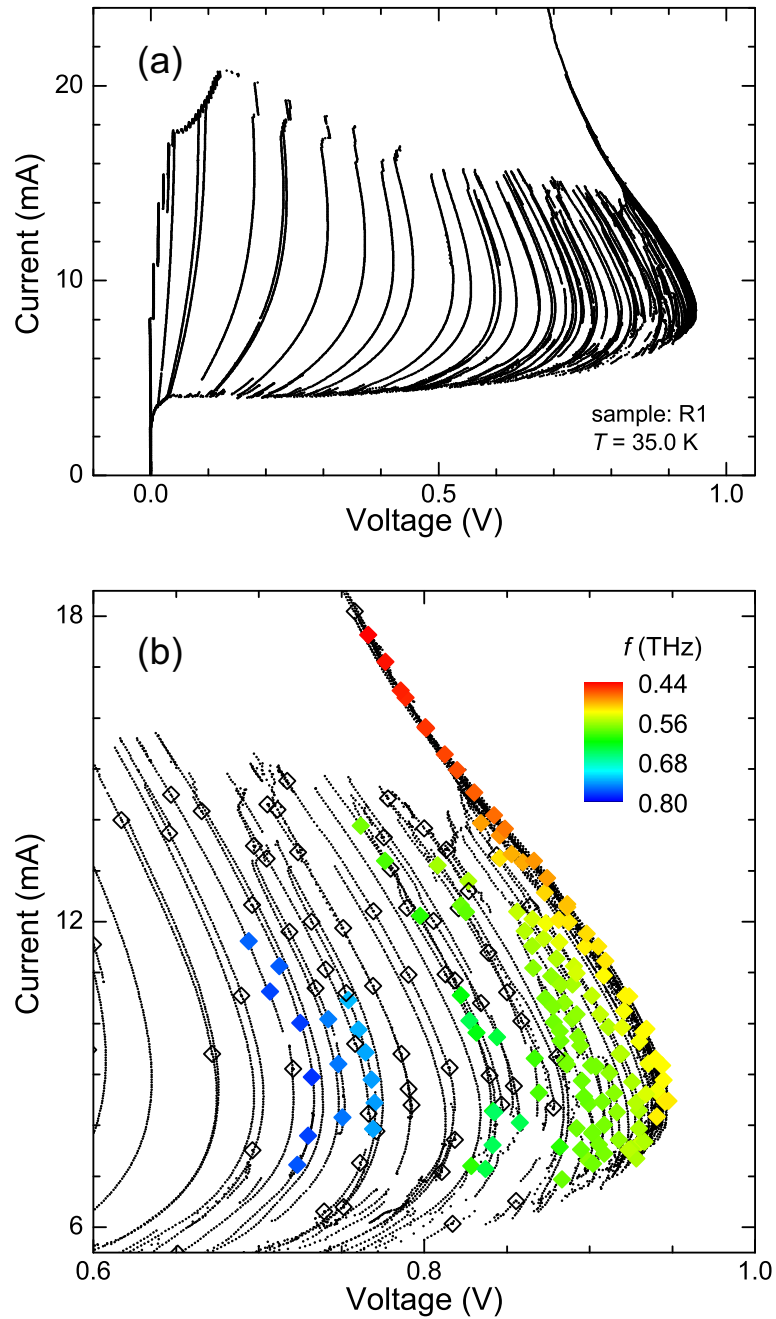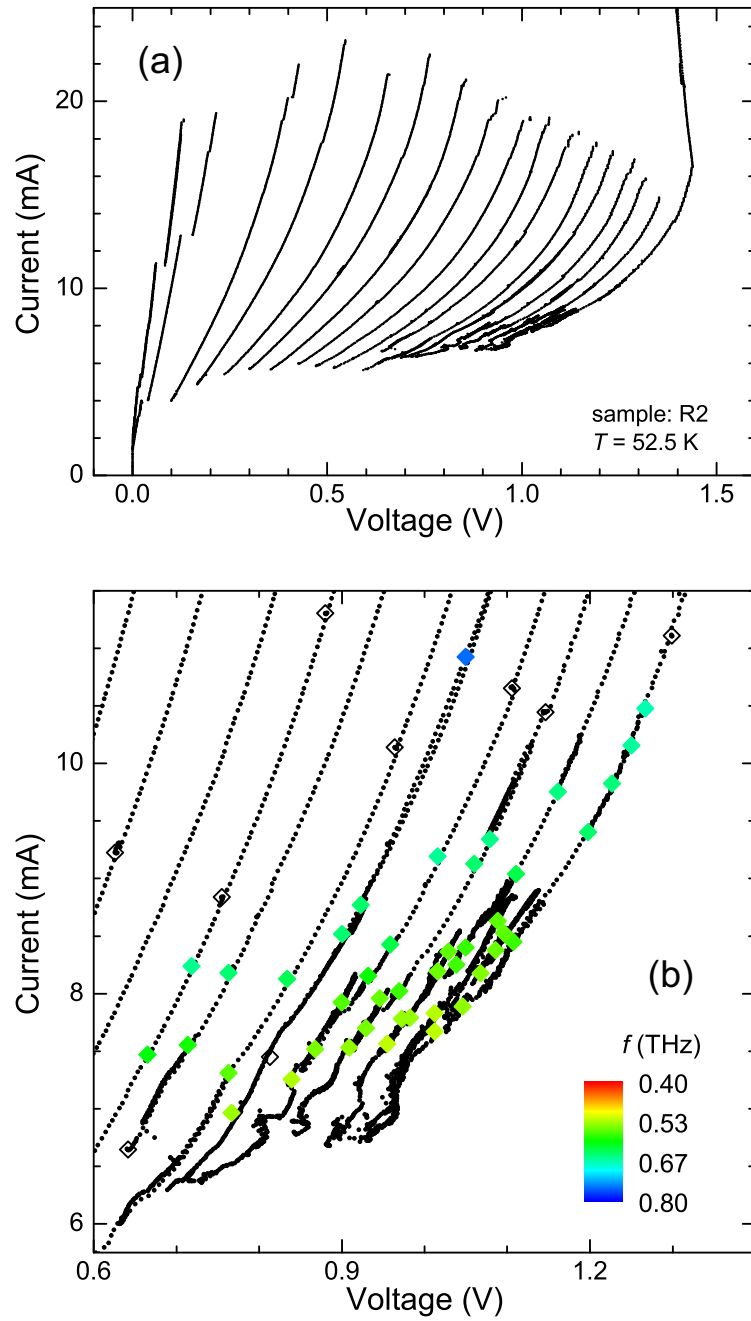
Figure 5.13: (a) Full IVC branches for R2 at $T = 52.5$ K. (b) Multiple branches in the high-bias region of Fig. 5.13(a) and THz radiation at the color-coded frequencies.

respectively. In the insets in Figs. 5.14 and 5.15, the entire emission data from the full branches of R1 and R2 are plotted as $f(V/N)$. For both R1 and R2, the Josephson relation $f = f_J$ represented by each dashed line, is excellently obeyed.

The spectrum peak intensities versus observed frequency f from R1 and R2 are presented in Figs. 5.16 and 5.17 on a semi-logarithmic scale. The calculated cavity resonance frequencies $f = f_{mp}^r$ from the geometrical conditions of the rectangular mesas are also shown at the top of these figures. For R1, no radiation was found for $f < 0.40$ THz, excluding the expected cavity resonance frequencies of $f_{01}^r = 0.255$ and $f_{10}^r = 0.357$ THz. Moreover, the spectrum observed in Fig. 5.16 is almost completely unrelated to any of the internal cavity modes. For example, the strongest intensity observed for 0.575 THz at $V = 0.894$ V and $I = 9.56$ mA, and $N_{\text{fit}} = 753$, is far from the two nearest cavity resonance frequencies. If $N_{\text{max}} = 851$, there are $\sim 4.3 \times 10^{130}$ ways to have $N_{\text{fit}} = 753$ of the N_{max} junctions in the resistive state, each of which could in principle lead to a different radiation intensity. Hence, multiply cycling through the IVCs led to a large variation in peak intensity at that (I, V) point. More importantly, the radiation spectrum in Fig. 5.16 is continuous from 0.44 THz $< f < 0.78$ THz, except for a gap between 0.66 and 0.73 THz. The gap may be due to some experimental difficulty in accessing the appropriate branches. This widely continuous spectrum independent of internal cavity resonances implies that f is broadly tunable.

The peak intensity spectrum of R2 shown in Fig. 5.17 also suggests that the R2 radiation is broadly tunable, with the f range of 0.43 THz $< f < 0.76$ THz and a small gap between 0.67 and 0.75 THz. For R2, the f range from 0.43 to 0.55 THz is below the range of the lowest cavity resonance frequency f_{01}^r. Unlike the peak intensity spectrum of R1 shown in Fig. 5.16, the largest intensity at 0.565 THz is close to this f_{10}^r range. In this case, the synchronization of the N resistive junctions could be aided by the excitation of this internal cavity mode. Although these sharp differences between the radiation conditions from bias points located at the outermost or an internal branch are not yet well understood, these experimental facts clearly show that the primary mechanism of the radiation is definitely the intrinsic Josephson effect, and that the internal TM cavity resonance produced by the geometrical shape of the mesa is at best of minor importance for the radiation.

As other results, Fig. 5.18(a) shows a map of the radiation obtained from nearly-square mesa S2 at the filled diamond points, where the radiation frequency f is color-coded. The spectrum peak intensities versus f from R3 and S2 are presented in Figs. 5.18(b) on a semi-logarithmic scale. As can be expected from the above argument regarding R1 and R2, the observed frequencies naturally increase as the radiation points shift into the internal IVC branch regions. By performing similar experiments with other samples, we also found that the range of the tunable frequencies Δf depends significantly upon the sample; $\Delta f = 0.29$–0.42 THz at $T = 15$ K for sample R3, $\Delta f = 0.49$–0.68 THz at $T = 35$ K for sample S2, and $\Delta f = 0.42$–0.57 THz at $T = 30$ K for sample D3, respectively. T's in these measurements were set to the optimum value in order to produce the maximum output intensity. It is interesting to investigate the T dependence of Δf further, since the important parameter V/N varies considerably, depending on the thermal conditions of the radiating mesa.

5.4.2 Comparison between stand-alone and groove-type mesas

Since R2 is the first mesa studied in which Au layers were on the top and bottom of the mesa, *i.e.*, stand-alone type mesa, its novel properties require further discussion. First, we note that the overall tunability range for R2 is given by a single branch, as indicated in Fig. 5.15. The high frequency end of these data corresponds to the extreme far-right point in Fig. 5.17. This point was very weak in intensity, and suggests that similar tunability of the other branches might also be occurring, but their intensities may have been too low.

We remark that even though the overall range of the radiation from R2 is broadly tunable, the radiation intensity appears to be greatly enhanced by the cavity resonances. It should be noted that such enhancement was also observed from R1 by using the collecting optical system as discussed in the last chapter (see Fig. 4.24). In the R2 case, the stand-alone geometry and the absence of the underlaying Bi-2212 ground plane may allow for a much higher output intensity, as predicted by Klemm [15, 59, 60]. Also, the boundary condition for R2 is likely to be at least somewhat consistent with those of a standard rectangular mesa, since the intense radiation occurred at $f = f_{10}^r$. The other samples we studied were mainly groove-type mesas prepared by making a groove around the mesa by using the focused ion beam milling, with the resulting Bi-2212 mesa sitting upon a Bi-2212 ground plane and surrounded by Bi-2212 mesas of large extent and the same height t. Since the groove width is only about 10 times larger than t, comparable to or smaller than the emission wavelengths, it is very likely that the electromagnetic boundary conditions are very different than for stand-alone mesa R2. This large differences in the geometries could account for the differences in the observed radiation features.

5.4.3 Self-heating effect

Figures 5.14 and 5.15 clearly demonstrate that f is slightly tunable on each branch with fixed N as indicated by a fixed symbol and color. In Figs. 5.19(a) and 5.19(b), we replotted the data from each R1 and R2 branch as $f(N_{\mathrm{fit}})$, respectively. It is worthwhile noticing that the f values from lower branch-number radiation from R1 could exceed 1 THz. Although the overall tunability of R1 and R2 is nearly the same as indicated by the vertical bars for each fixed N_{fit}, R1 and R2 display rather different aspects of tunability. Namely, for R1, this range is primarily due to the f dependence on the IVC branch number N, whereas for R2, the tunability is greatest on a single branch.

Such a sharp contrast of the f tunability can be understood by considering the mechanism of the tunable radiation in the internal IVC branches. Figure 5.20 shows 5 IVC branches for a $N_{\mathrm{max}} = 5$ junction system. In the ideal case, each branch should be uniformly separated by the constant gap voltage V_g at fixed T; for example, $V_g = 25$ mV at 4 K for Bi-2212 [93], as indicated by dotted 5 lines in Fig. 5.20. However, since the actual Bi-2212 mesa is inevitably Joule heated especially in the high-bias region, the gap voltage V_g decreases down to ~ 1 mV ($\Leftrightarrow 0.483$ THz) as the number of the resistive junction N increases, producing the non-uniform IVC branches as indicated by solid 5 lines in Fig. 5.20. Thus, the radiation
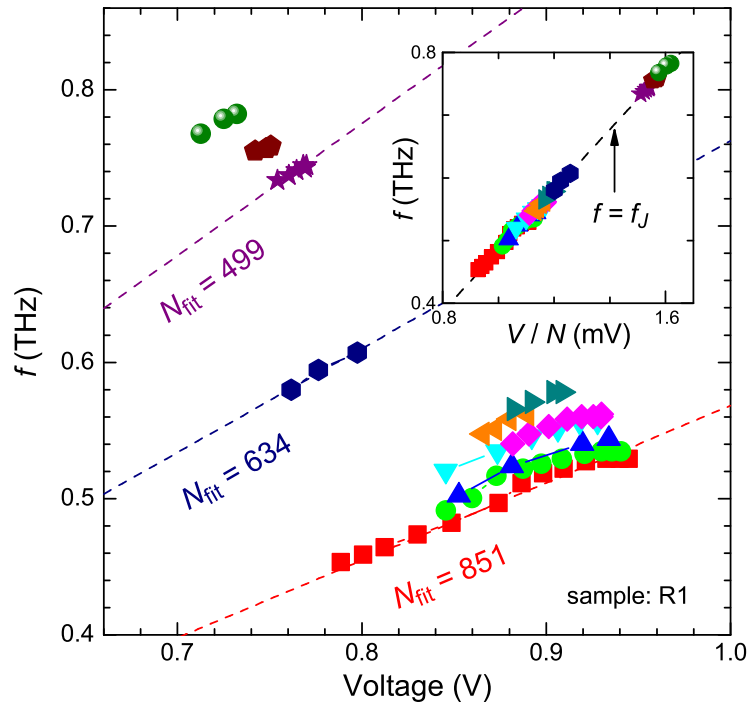
Figure 5.14: $f(V)$ plots for 11 IVC branches for R1. Dashed lines represents the Josephson relation: $f = f_J = (2e/h)V/N_{\text{fit}}$ with $N_{\text{fit}} = 499$, 634, and 851. The inset shows $f(V/N)$.
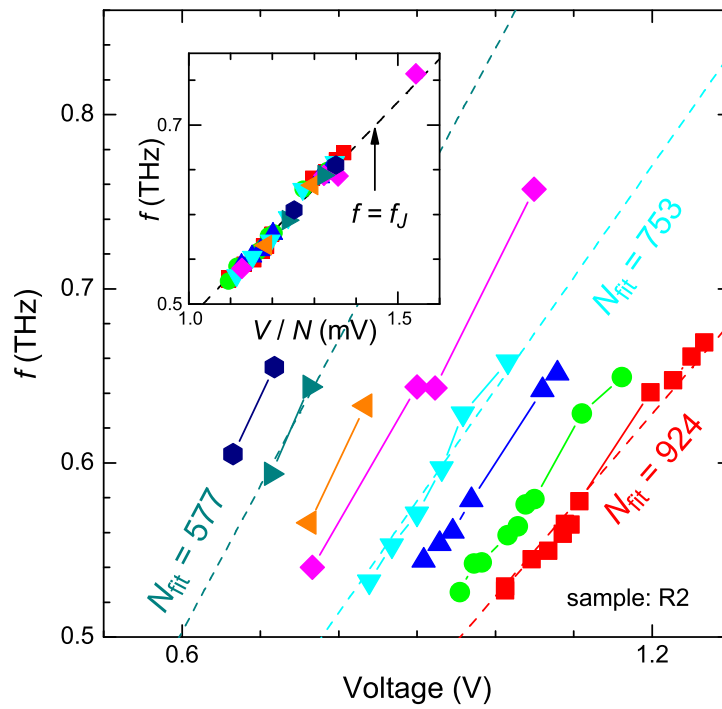

Figure 5.15: $f(V)$ plots for 8 IVC branches for R2. Dashed lines represents the Josephson relation: $f = f_J = (2e/h)V/N_{\text{fit}}$ with $N_{\text{fit}} = 577$, 753, and 924. The inset shows $f(V/N)$.

Figure 5.16: Peak intensity on a logarithmic scale versus f for R1. N-values are color-coded. Calculated f_{mp}^r ranges are given at the top.
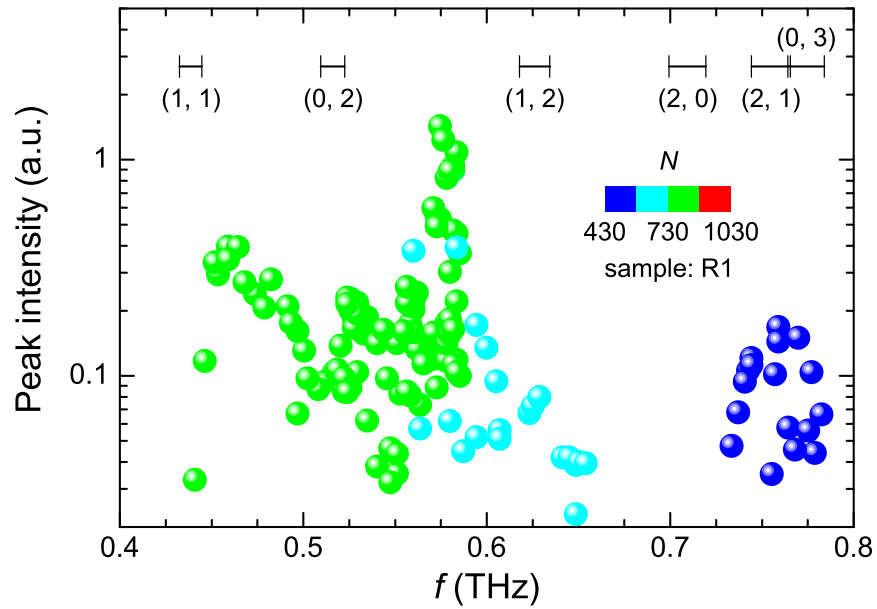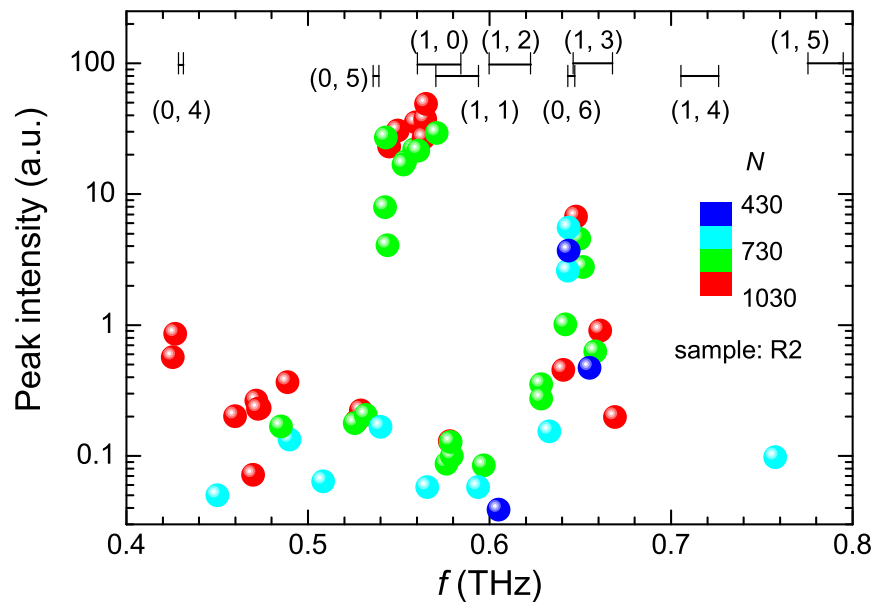

Figure 5.17: Peak intensity on a logarithmic scale versus f for R2. N-values are color-coded. Calculated f_{mp}^r ranges are given at the top.
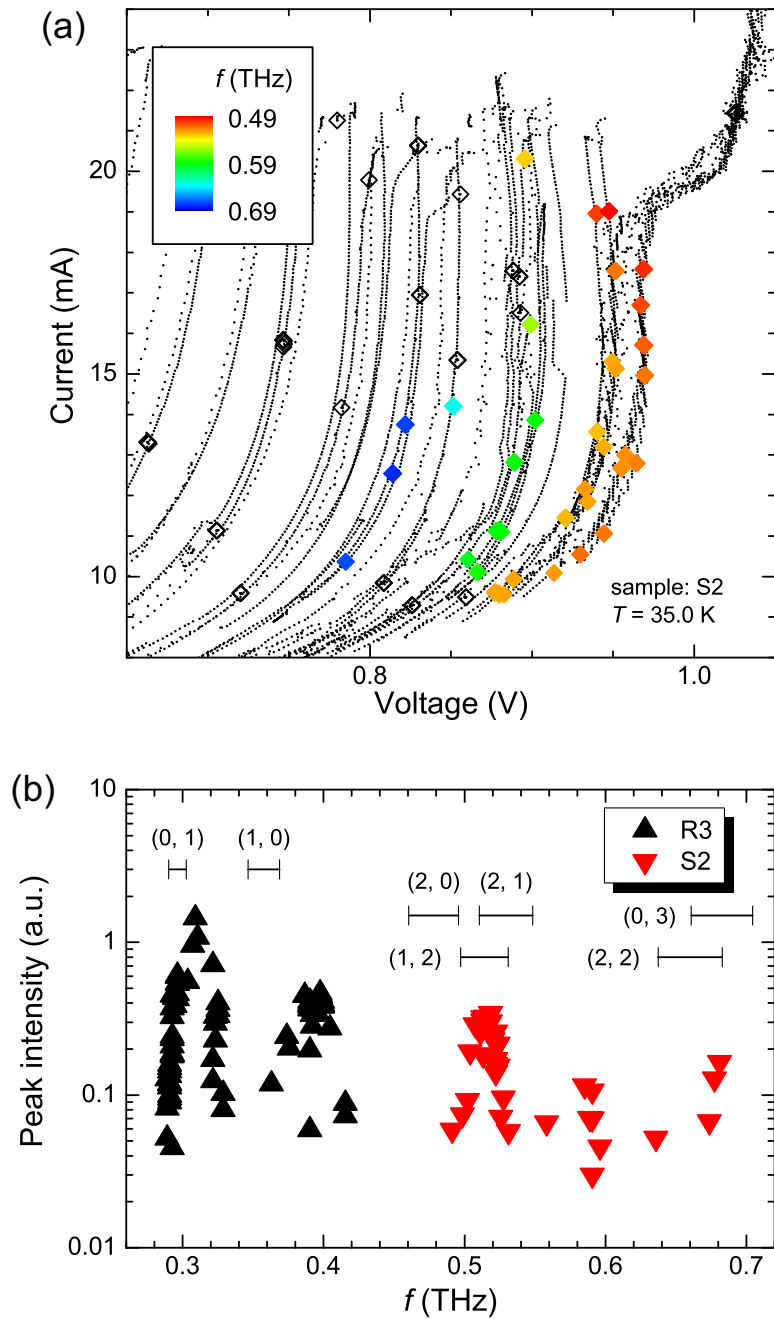
Figure 5.18: (a) Multiple IVC branches in the high-bias region and THz radiation at the color-coded frequencies for S2. (b) Peak intensities on a logarithmic scale versus f for R3 and S2. Calculated f_{mp}^r ranges are given at the top.

frequency f should, naturally, decrease as N increases as demonstrated in Figs. 5.19(a) and 5.19(b), because the radiation frequency f is always proportional to the voltage per resistive junction (V/N) according to the Josephson relation $f = f_J = (2e/h)V/N$. Since $V_g(I,V,T)$ is likely to depend strongly on the thermal condition of the mesa, the f tunability has also the strong sample dependence. In addition, the critical (switching) current I_c for each branch may be reduced as N increases, as indicated in Fig. 5.20. This is consistent with the experimentally-obtained IVCs shown in Figs. 5.12(a) and 5.13(a).
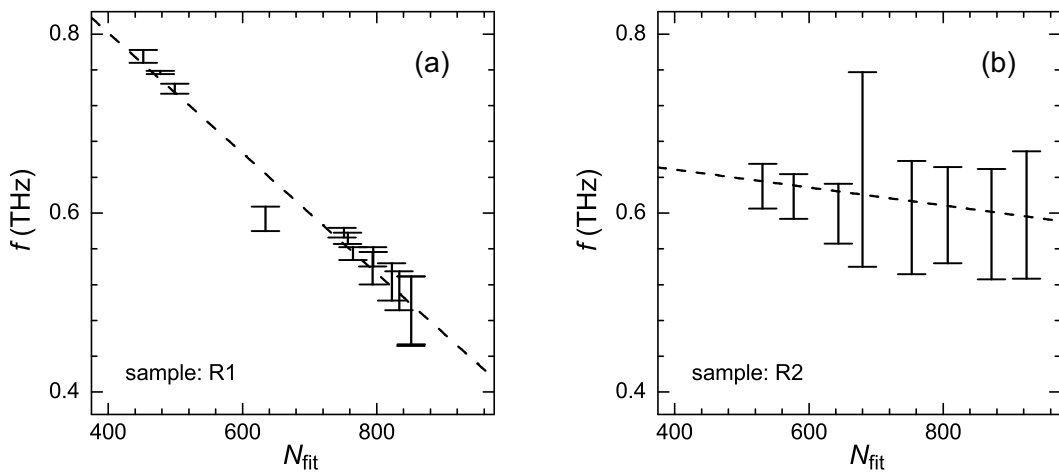

Figure 5.19: $f(N_{\text{fit}})$ ranges for (a) R1 and (b) R2, with dashed eye guides.
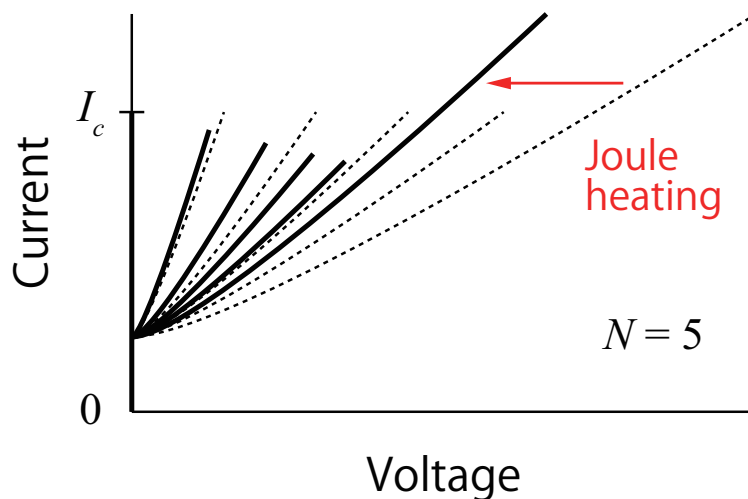

Figure 5.20: IVC branches for a $N = 5$ intrinsic junction system.

5.5 Conclusion

Many previous studies have revealed that there exist superconducting CuO_2 double layers and an inserted block layer in the unit cell of the high-T_c superconductor such as Bi-2212. Such an anisotropic layered structure is considered to act as a natural stack of the atomic-scale Josephson junctions [19], which is often called the intrinsic Josephson junction [1]. The point is that the thickness of the intrinsic superconducting CuO_2 layer is comparable with the electric screening length. This implies that the charge imbalance at the surface of the superconducting layer cannot be neglected, causing the capacitive coupling to the neighboring junctions [108]. Such a charge fluctuation along the c-axis actually gives rise to the collective excitation of the longitudinal Josephson plasma mode [112, 113]. We could obtain the IVCs of the intrinsic junction system by numerically calculating Eq. (5.28) under some proper initial conditions. The multiply-branched IVC for the weakly-coupled system with $\alpha \sim 0.1$ suggests that each junction can individually switch from the pinned mode to the rotating mode, whereas in the case of the strongly-coupled system with $\alpha > 1.0$, there exist no multiple branch but several small steps on the outermost branch.

Since the atomic-scale intrinsic Josephson junctions is perfectly uniform and has a variety of coupling strengths, the stack of intrinsic junctions is an exceptional system to investigate the non-linear dynamics of the lattice motion. In fact, in previous works, especially on the Josephson vortex dynamics and on the Josephson plasma excitation in the intrinsic system, a lot of important results have been produced to reveal the non-linear phase dynamics of the intrinsic system. With this background, we proposed the THz radiation experiment as a tool to study the non-linear phase dynamics of the intrinsic junction system. In particular, we could excite each junction individually by scanning the multiple IVC branches, and could directly survey the quasi-stable state of the system by detecting the THz waves from the localized rotating junctions.

To determine whether the excitation of an internal cavity TM mode was an essential feature to generate the coherent THz wave from the Bi-2212 mesa, we examined the internal IVC branches together with detecting the THz radiation. As a result, we found these internal IVC branches to radiate over a broad frequency range, and that the obtained radiation frequencies exactly satisfy the Josephson relation for a locally rotating junction. Hence, we concluded that the primary mechanism of the radiation is the intrinsic Josephson effect, and that the internal electromagnetic cavity resonance produced by the geometrical shape of the radiating mesa is at best of minor importance. We then propose that a high-power device can be constructed by surrounding the mesa with an external, tunable high-Q electromagnetic cavity. By examining yet lower internal branches, it ought to be possible to increase the upper f limit into the 1–10 THz range.

Chapter 6

THz imaging

6.1 Introduction

6.1.1 Overview of THz sources

The terahertz (THz) electromagnetic wave with a frequency span of 0.1–10 THz (1 THz = 10^{12} THz) is known to be the most unique area in all electromagnetic spectra, since it is simply unavailable due to lack of compact and convenient radiation sources [6]. Today, THz technology is finding use in an increasing wide variety of applications: information and communication technology, biology and medical sciences, non-destructive evaluation, homeland security, quality control of food and agricultural products, global environmental monitoring, and ultrafast computing among others. Hence, in recent years, much effort has been put in to develop the useful and powerful THz sources, in particular, in the field of semiconductors and laser technologies.

Figure 6.1 shows the continuous wave (CW) radiation intensity as a function of the frequency. The THz radiation using laser, either pulsed or CW falls into two general categories. The first involves generating an ultrafast photocurrent in a photoconductive switch or semiconductor using electric-field carrier acceleration or the photo-Dember effect. In the second category, THz waves are generated by non-linear optical effects such as optical rectification difference-frequency generation, or optical parametric oscillation.

The quantum cascade laser (QCL) that generates the 70-THz CW was first developed in 1994 [120], and subsequent works have demonstrated the lasing frequency down to 4.4 THz [121]. It was also reported that the lasing frequency can be reduced down to 1.39 THz by applying an external magnetic field [122]. The maximum CW radiation power from QCLs working at ∼ 10 THz is in the tens of milliwatts as shown in Fig. 6.1. Recently, Kumar *et al.* succeeded in realizing a 1.8 THz QCL at a heat-sink temperature of 163 K (∼1.9 $\hbar\omega/k_B$) [123], which is significantly greater than the empirical temperature limit of $\hbar\omega/k_B$. The current research objects are to reduce the threshold currents and lasing frequency and to increase the operational temperature and the range of tunable frequencies. To achieve these goals, new designs of structures, gratings, and waveguides are being studied intensively.
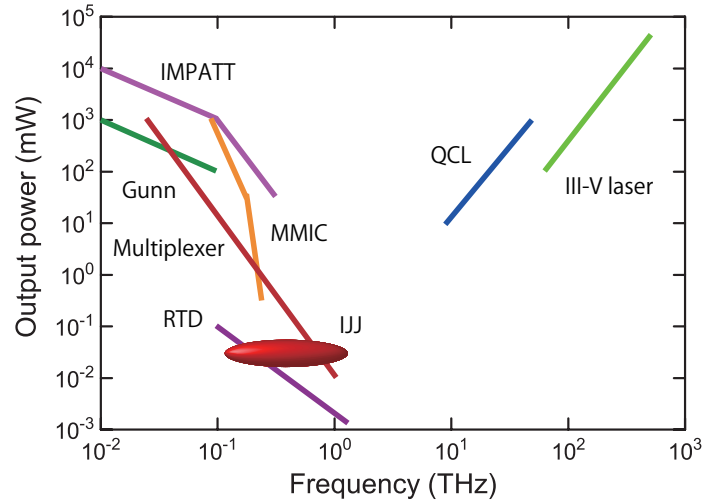
Figure 6.1: Output power as a function of frequency for impact ionization avalanche transit-time (IMPATT) diode, microwave monolithic integrated circuit (MMIC), high-T_c intrinsic Josephson junction (IJJ) oscillator, Gunn diode, multiplexer, RTD, QCL, and III-V laser.

Other candidates of the useful THz source device, such as the uni-traveling-carrier photodiodes [124] have been developed in the past few decades. Recently, graphene and carbon nanotubes have also been reported to be good candidates for the THz wave generator [125, 126]. The resonant tunneling diode (RTD) is also one of the potential candidates of the CW THz source device that works at room temperature [127, 128]. Recently, the output power up to 10 µW and 1.04 THz as fundamental radiation using InGaAs/AlAs RTD with slot antennas were reported [129, 130]. In order to further improve the radiation efficiency, a novel RTD structure composed of a graded emitter and thin barriers with an optimized offset slot antenna for making use of the large negative differential conductance has been demonstrated [131].

6.1.2   Imaging with THz waves

Since THz waves have a property to penetrate through various objects, such as plastics, paper, ceramics, semiconductors, liquids, proteins *etc.*, similar to radio waves, they can be used for imaging of various cm-by-cm wide substances [132], where the spatial resolution is actually determined by the wavelength of the THz wave, typically ~1 mm. Also, since the irradiation damage to these soft objects is known to be negligibly small in contrast to the X-ray, in fact there is much demand for the nondestructive and noninvasive imaging techniques in the field of the material inspection, medical diagnostic, security check, environmental monitoring. Moreover, measuring the absorption spectrum in the THz region, where various molecular vibration modes of organic and high-molecular compounds dominant the EM wave absorption, one can identify the chemical substances both qualitatively and quantitatively. To realize these applications, compact, solid-state, and reliable THz source devices are strongly desired in spite of their technical difficulties.

Practical THz imaging experiments using the THz time-domain spectroscopy (THz-TDS) technique have come a long way since the first demonstration of free-space THz transmitters and detectors a few decades ago [133]. In particular, it has proved to be a powerful tool for spectroscopic measurement of far-infrared properties of materials such as dielectrics and semi-conductors [134], superconductors [135], liquids [136], and gases [137]. Unlike in traditional FT-IR spectroscopy, in which a blackbody radiation source and a bolometer are used, both the generation and the detection are optically gated in THz-TDS. This offers extraordinary noise rejection; for example, signal-to-noise ratios as high as 10,000:1 were achieved [138]. Furthermore, by using the THz-TDS technique, we can measure both the amplitude and the phase of the THz waveform because the detection is coherent, allowing one to extract the full complex dielectric constant of the material under investigation without having to resort to the Kramers–Kronig relations. Together with the ability to collimate and focus THz waves down to the diffraction limit of a few sub-millimeters at the sample [139], imaging of chemical compositions should be possible with reasonable spatial resolution. However, acquisition of THz waveforms has required lock-in detection and low-pass filtering with a 100–300 ms time constant per data point. With resulting acquisition times of a few minutes for a single THz waveform at each image point, imaging with THz transients has so far been impractical.

Recently, the THz imaging system based on a backward-wave oscillator as the CW radiation source was demonstrated [140]. The backward-wave oscillator can generate the continuous, linearly polarized, essentially monochromatic THz wave at a radiation frequency around 0.6 THz. The maximum output power is approximately 15 mW in this range of frequency. Figure 6.2(a) shows the THz image of the card box containing metallic objects; a 5-yen coin, a screw, and a paper clip, while Fig. 6.2(b) shows the THz image of a fresh plant leaf that reflects its vein structures. The image size of Fig. 6.2(b) of 138×138 pixels corresponds to a total acquisition time of ∼10 min. These application examples presented here give an idea of the large extent of the possibilities: real-time nondestructive testing, biological and medical imaging, and measurement of physical properties of substances. The only practical disadvantages of using the backward-wave oscillator may be, however, the limited tunability and incoherence of the emitted THz waves.
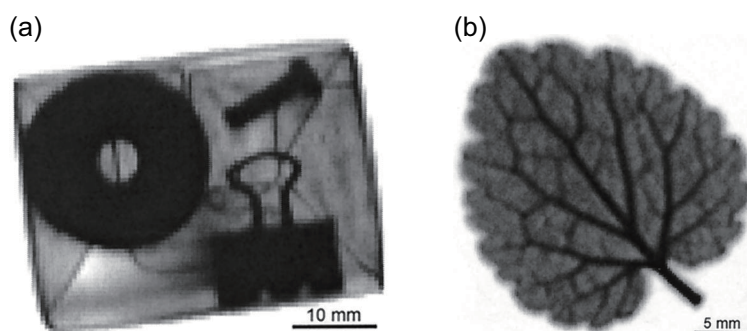
(a)   (b)

Figure 6.2: THz images of (a) metallic objects placed inside a card box and (b) a fresh leaf. (copied from [140])

A widely tunable THz parametric oscillator (TPO) [141] is also a good candidate of the THz source for the imaging purpose. Kawase *et al.* demonstrated the spectroscopic experiment [142] by using the spectroscopic imaging system based on the Q-switched Nd:YAG laser and the TPO [143]. Figure 6.3(a) shows the paper envelope containing three 10×10-mm^2 polyethylene bags, in which there were three drugs: MDMA (left), aspirin (center) as a reference, and methamphetamine (right). In Fig. 6.3(b), the transmission images at discrete frequencies from 1.3 to 2.0 THz are presented with a logarithmic gray scale. From the information contained in such multispectral images and previously recorded absorption spectra of the drugs, we can isolate and extract the drugs as shown in Fig. 6.3(c). More importantly, we can identify them even in cases in which the target is a mixture of multiple drugs or when different drugs are arranged in layers.
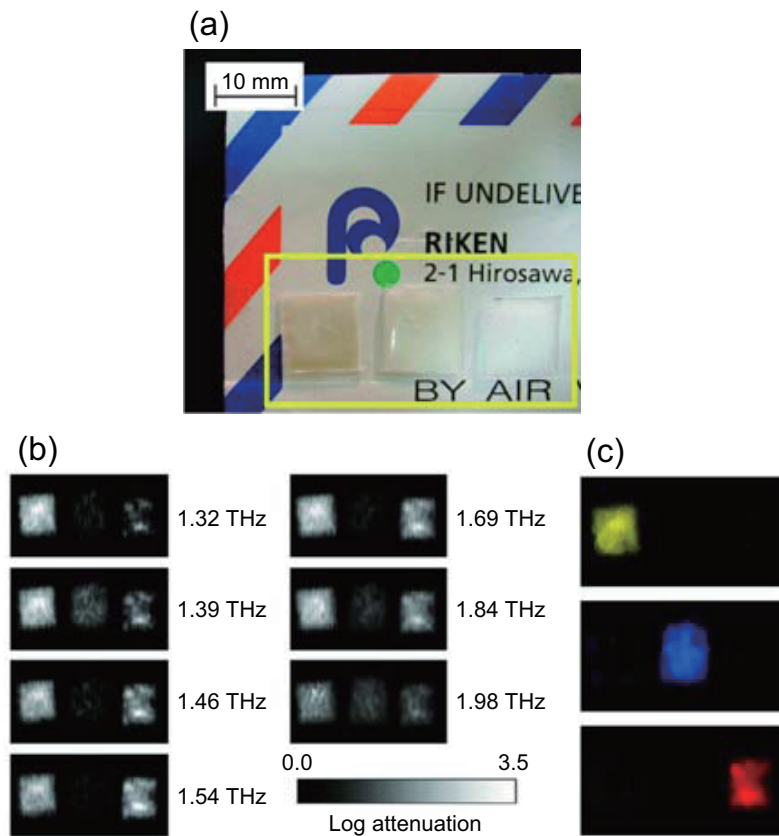

Figure 6.3: (a) Airmail envelope containing three polyethylene bags, in which three drugs; MDMA (left), aspirin (center), and methamphetamine (right), are placed. (b) Multispectral THz images of Fig. 6.3(a) at seven frequencies between 1.32 and 1.98 THz. (c) Spatial patterns of MDMA (yellow), aspirin (blue), and methamphetamine (red) extracted from Fig. 6.3(b). (copied from [132])

6.1.3 Purpose: Construction of the THz imaging system

In 2007, we have discovered a remarkable phenomenon that the high transition temperature (T_c) superconducting $Bi_2Sr_2CaCu_2O_{8+\delta}$ (Bi-2212) compound generates intense and coherent electromagnetic waves in a THz frequency region [5]. This compound is known as the intrinsic Josephson junction (IJJ) system [1], where the insulating Bi_2O_2 planes are sandwiched by CuO_2 double planes responsible for superconductivity. Since the distance between CuO_2 planes is only 1.533 nm and the superconducting coupling is extremely small, this system is known to behave as a multi-stack of IJJ's. As previous chapters have shown, the THz electromagnetic wave can be generated by injecting DC current into a mesa structure, which is nano-engineered either by a focused ion beam or ion etching technique, in a rectangular shape of 45–100 µm in width, 300–400 µm in length and 1–2 µm in thickness, respectively [5]. According to previous studies, the radiation frequency f obeys two necessary conditions: One is the Josephson relation [19] given by $f = f_J = (2e/h)V/N$, where e is the elementary charge, h Planck's constant, V the voltage, and N the number of the resistive IJJ's, implying that applying 1 mV produces the 0.4836 THz AC current. Another is the cavity resonance condition: in the case of the rectangular TM(1, 0) mode, it can be written as $f_{10}^r = c_0/2\sqrt{\varepsilon}w$, where c_0 is the speed of light in vacuum, ε the dielectric constant of Bi-2212, and w the width of the mesa.

Previous studies also found that the present IJJ's can be used for a THz source device, which emits continuous and microwatt power electromagnetic waves at tunable frequencies between 0.3–1.0 THz with the spectral linewidth of ∼0.5 GHz [12], and can be operated in the power modulation mode at 500 kHz [13]. These device characteristics enable us to accumulate the data for an individual measurement point at high resolution in a few milliseconds or less. In addition, the solid-state IJJ device is extremely small in size and its output power is stable enough during operation. Therefore, in this chapter, we demonstrate the THz imaging experiment by using the IJJ devices as THz sources in order to promote effective use of the present IJJ device for various potential applications.

6.2 Experimental

6.2.1 System configuration

The IJJ THz oscillation devices were assembled in a He-flow cryostat with two off-axis parabolic mirrors, scan stage and fast hot-electron (HE) bolometer as seen in Fig. 6.4. Two off-axis parabolic mirrors with focal lengths of 152.4 mm and 220 mm and diameters of 75 mm are set to collimate and focus the THz waves at the sample position. The image object is fixed on the 2D scan stage (SIGMA KOKI Co., SGAMH26-200) and scanned in X (horizontal) and Z (vertical) direction at the variable speed below 130 mm/s. The practical maximum speed may be 80 mm/s, which corresponds to a 5-ms time constant per data point when the measurement step is set to sub-millimeter distances by considering the diffraction limit. Although the IJJ device can be modulated much faster [13], in the present setup the

maximum scan speed only depends on the minimum time constant of the lock-in amplifier (EG&G instruments Co., 7265). Nevertheless, the actual imaging has been performed at the speed of 32 mm/s in order to obtain sufficient data points. Before starting every scan, the optical path presented is precisely adjusted by using the visible light from a light-emitting diode attached to the source position. A high-speed InSb HE bolometer (QMC Instruments Ltd., QFI/2BI) placed right behind the scan stage is used for measuring the output intensity of the THz waves passing the sample. The current-voltage (*I-V*) characteristics (IVCs) of the IJJ device and the bolometer output are simultaneously monitored by two oscilloscopes (OSCs). A lower left photograph in Fig. 6.4 shows the top views of the actual imaging system used in this study.
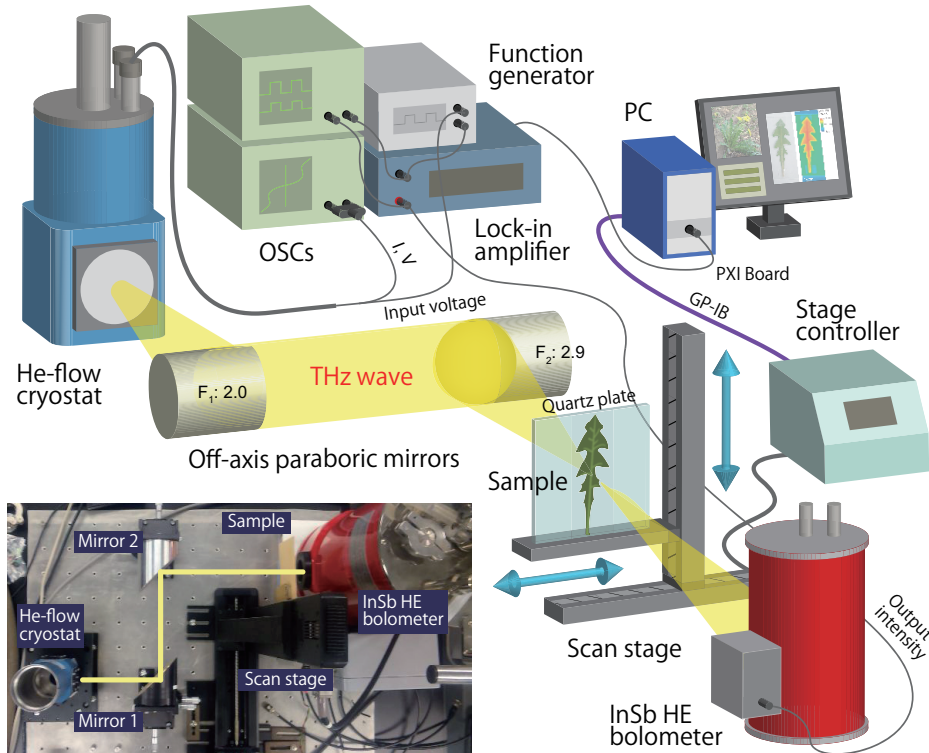

Figure 6.4: Schematic diagram of the THz imaging system. The left lower photo presents the top view of the actual system.

6.2.2   Device characteristics

The terrace-type IJJ oscillation device used is schematically presented in Fig. 3.2(b). The dimensions of the mesa structure ($62 \times 400 \times 1.9$ µm^3) were measured by the atomic force microscope. A solid curve shown in Fig. 6.5(a) represents the IVC in the high-bias region above 1.0 V, while the inset of Fig. 6.5(a) shows an overall hysteresis loop typical of the outermost IVC branch of an IJJ system [1]. This curve was obtained by the cyclic DC

current scan. The finite voltage below $I = 13.8$ mA at $V \sim 0$ V, where N_{max} IJJ's are in the zero-voltage state, is caused by the contact resistance due to the two-terminal measurement.

During IVC measurements, we also monitored the output voltage from the HE bolometer as shown in Fig. 6.5(b). In this particular device, two radiation peaks (one at higher current with lower intensity and the other at lower current with higher intensity) were clearly observed. The maximum bolometer output of 13.7 mV at $V = 1.618$ V and $I = 11.5$ mA corresponds to approximately 0.2 µW according to the calibration of the sensitivity of the bolometer. Note that the total output power from the device should be evaluated separately by measuring the spatial radiation patterns [14, 40], since the solid angle of the detector window is only 3.2×10^{-3} sr. The radiation spectrum measured at 11.5 mA by the FT-IR spectrometer (JASCO Co., FARIS-1) is shown in the inset of Fig. 6.5(b), where a sharp emission peak at $f = 0.54$ THz is clearly observed. Using the AC Josephson relation with the contact resistance of 13 Ω, the number of resistive IJJ's can be estimated to be $N = 1320$, which is in good agreement with $N_{\mathrm{max}} \sim 1240$ given by the mesa height of 1.9 µm.
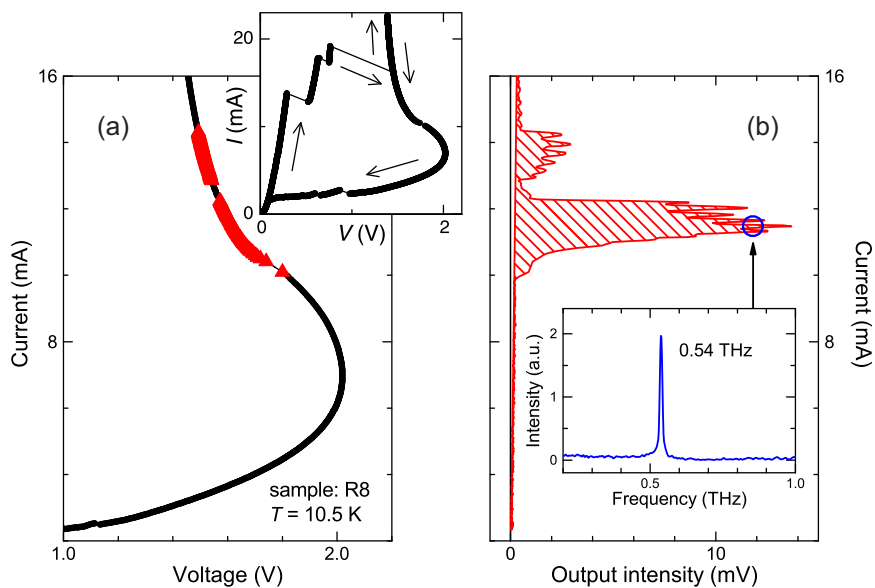

Figure 6.5: (a) IVCs of the IJJ device at $T = 10.5$ K. The right inset shows the overall IVC. (b) The current on the vertical axis common to Fig. 6.5(a) versus the output intensity. The inset shows the FT-IR radiation spectrum at 1.618 V.

6.2.3 Imaging procedures

The actual imaging measurement has been performed with the following procedure: In order to do lock-in detection, the pulse modulated THz wave was generated from the IJJ device by applying an additional square wave with a small amplitude (≤ 50 mV) at 10 kHz on the constant DC offset voltage using the function generator (Hewlett-Packard Co., 33120A). The lock-in detection using such an electronic modulation technique after optimization of

the HE bolometer noise performance by operating at about 10 kHz frequency is much better than the other methods such as used of an optical chopper, since the far-infrared background noise due to the ambient spurious radiation can be removed from the signal. The maximum intensity was then obtained by adjusting the offset level of the DC voltage and stabilized well to minimize the power fluctuations by adjusting the amplitude of the square wave. The imaging data are accumulated by simultaneous measurement of the sample positions (X, Z) and the bolometer output voltage. The output voltage is acquired by an AD converter installed in the PXI bus system (National Instruments Co.) through the analog output channel of the lock-in amplifier. Scanning parameters such as speed, step, and measurement area can be set by a homemade LabVIEW (National Instruments Co.) program. The obtained data are directly stored in the hard-disk drive and are simultaneously displayed on the PC screen in real time. The data set are stored in a ready-to-use spreadsheet file format for the convenience of the analysis.

6.3   Experimental results and discussion

6.3.1   THz images of various objects

As test examples, THz images of various objects are shown: two Japanese coins, a thin razor blade, and knives placed inside paper envelopes in Figs. 6.6, 6.7, and 6.8, a fresh plant leaf of a dandelion in Fig. 6.9, a student ID card in Fig. 6.10, a watermarked picture of a Japanese ten-thousand-yen bill in Fig. 6.11, a floppy disk in Fig. 6.12, and a thin slice of pork meat in Fig. 6.13. In these measurements, the radiation frequency was set to $f = 0.54$ THz as shown in the inset of Fig. 6.5(b). The image objects were scanned in X and Z directions at the speed of 32 mm/s by the scan stage. The screen size, for example, of the THz image shown in Fig. 6.6 is 330×250 pixels corresponding to the measurement step of 0.2×0.2 mm^2, which was appropriately set in terms of the required spatial resolution. It took about 20 minutes to complete the data acquisition for one THz image. Note that the constancy of the bolometer output in the green area shown in Fig. 6.6, where there is no absorbing object, guarantees the time stability of the source device. The expected signal-to-noise (S/N) ratio in these measurements exceeds 130:1, since the noise level is 0.1 mV in comparison to the maximum bolometer output of 13.7 mV as shown in Fig. 6.5(b).

Here, all features of the transmission image associated with metallic, paper, plastic, and biological objects can be clearly seen. Especially, a hole of the 5-yen coin in Fig. 6.6 is very vividly seen, which has the diameter of 5 mm exactly. The estimated spatial resolution of approximately 1 mm or less is comparable with the expected Rayleigh limit. From Figs. 6.6, 6.7, and 6.8, calculated transmittance of one sheet of paper is 79%, and it is clear that the metallic objects are not transparent at all.

It is interesting to note that several interference fringe-like patterns in the deeper blue area in Fig. 6.6 are clearly observed. To understand this peculiar phenomenon, we consider the interference effect of the incident THz wave: The THz wave with the wavelength $\lambda =$
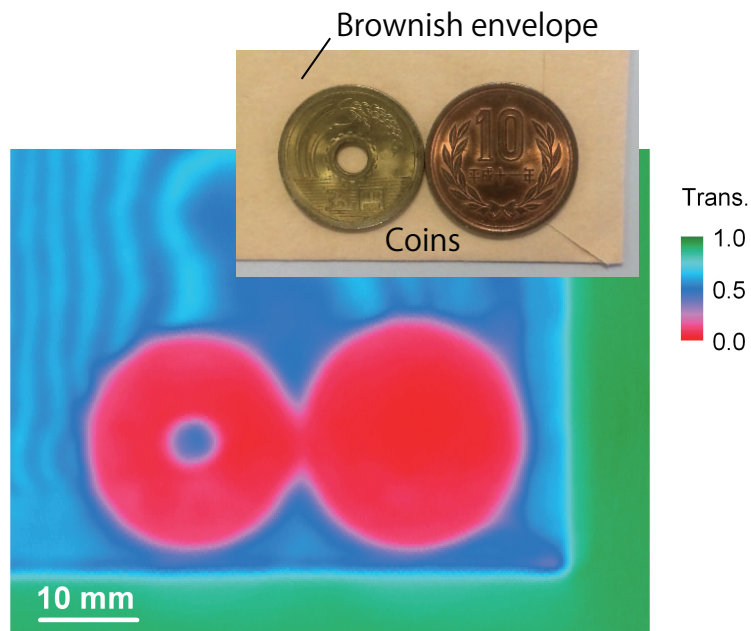
Figure 6.6: THz image of 5-yen (left) and 10-yen (right) Japanese coins placed inside a brownish paper envelope. The optical image is presented beside the THz image.
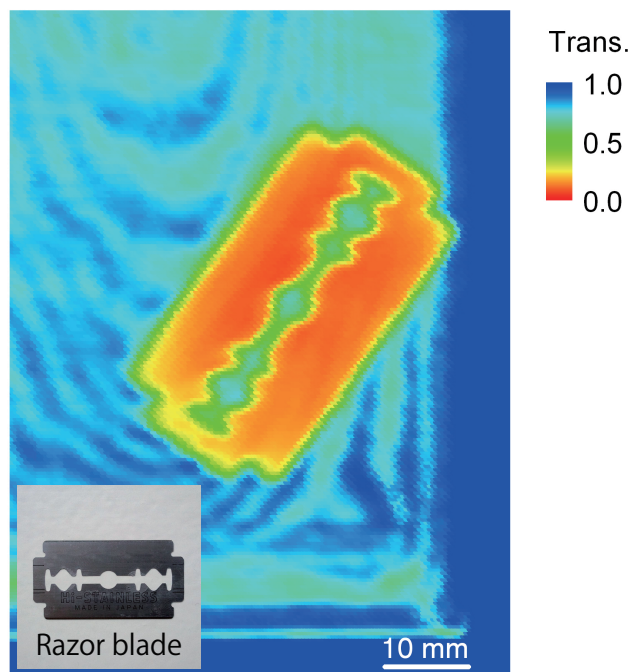

Figure 6.7: THz image of a razor blade placed inside a brownish paper envelope. The optical image is presented beside the THz image.
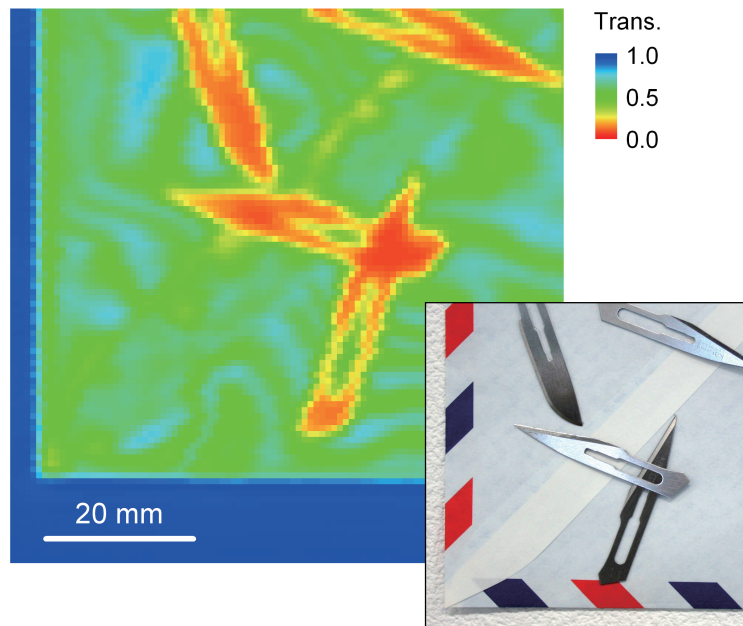
Figure 6.8: THz image of thin knives placed inside a brownish envelope. The optical image is presented beside the THz image.
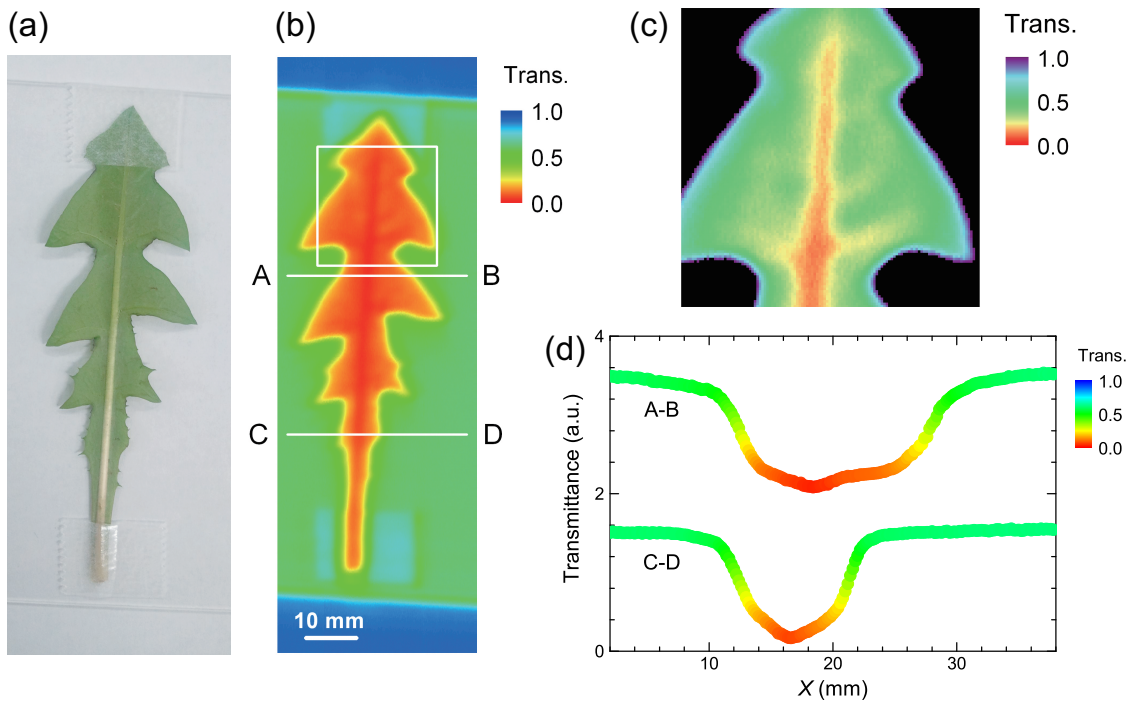

Figure 6.9: (a) Optical and (b) THz images of a fresh leaf of a dandelion. (c) Enlarged THz image of Fig. 6.9(b) that clearly shows the water vein structures. (d) Profile data at lines A–B and C–D indicated in Fig. 6.9(b) offset by 2 a.u. for clarity.
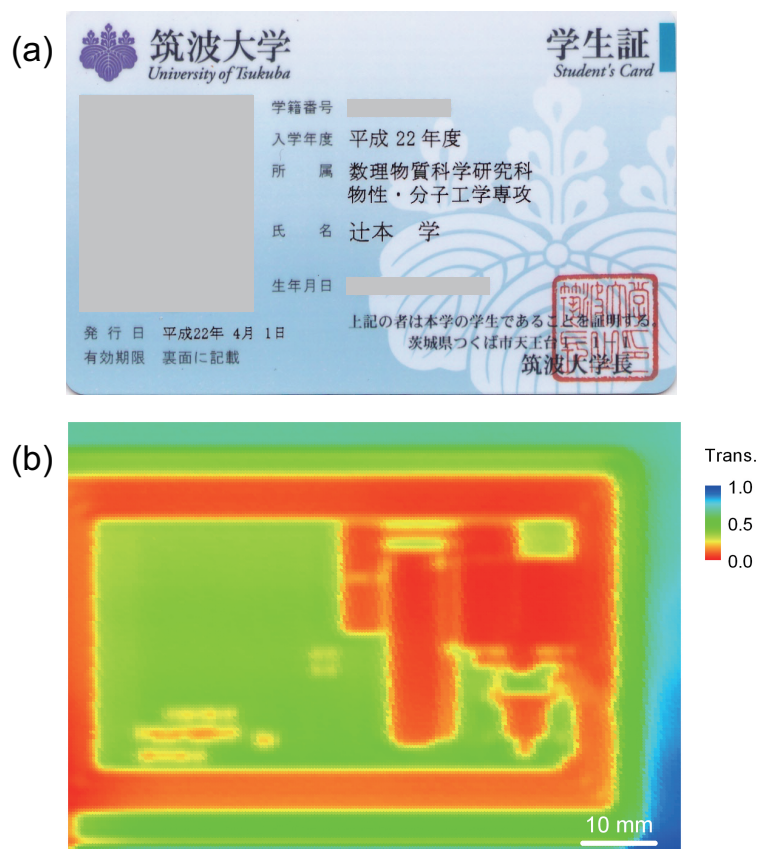
Figure 6.10: (a) Optical and (b) THz images of a student ID card. We can see through an integrated circuit inside a card.
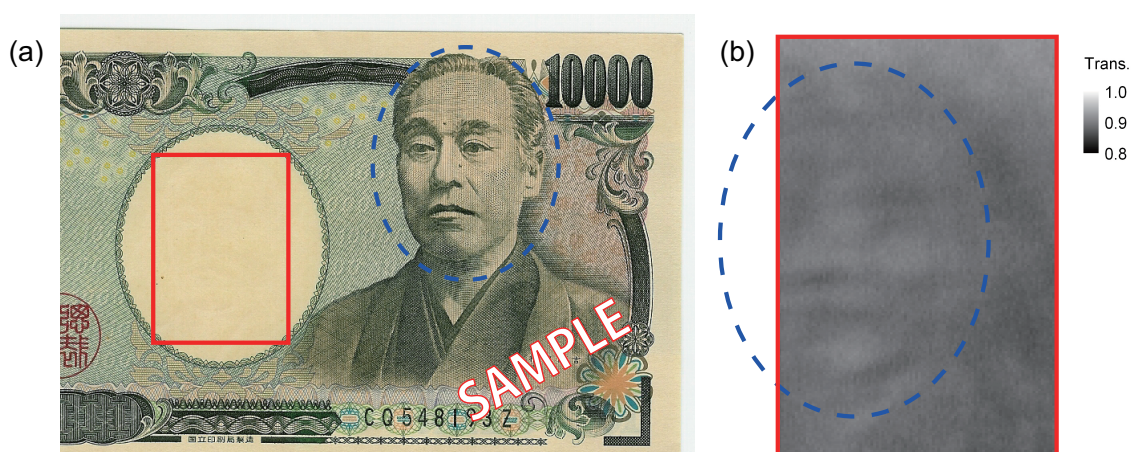

Figure 6.11: (a) A photo of Japanese ten-thousand-yen bill and (b) a THz image of its watermarked picture. We can see through the face of Fukuzawa Yukichi on the circled area in Fig. 6.11(b).
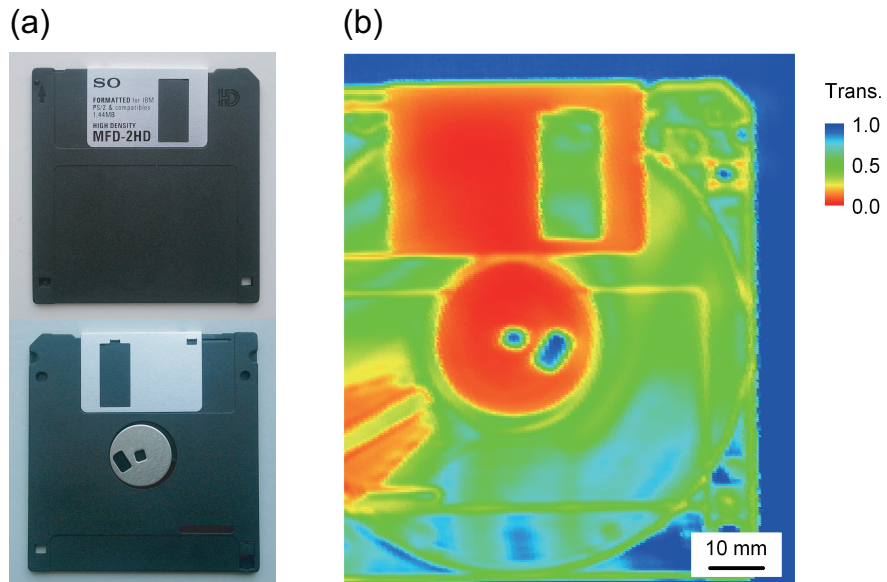
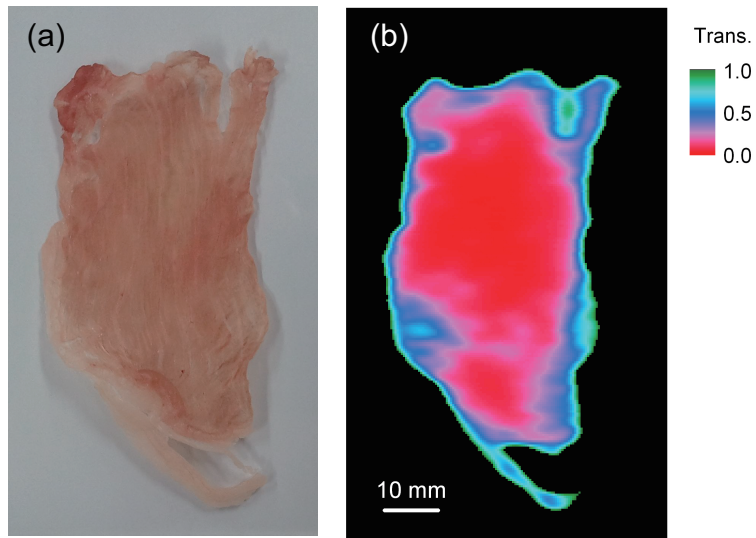Figure 6.12: (a) Optical and (b) THz images of a floppy disk.

Figure 6.13: (a) Optical and (b) THz images of a thin slice of pork meat.

$c_0/f \approx 0.56$ mm is likely to be multiply reflected at the inner walls of the envelope and interfered with itself. If so, the interference condition can be expressed as $2d_m = (\lambda/2) \times 2m$, where d_m is the interspace distance of the inner walls and m is an integer. Hence, the distance between two neighboring fringes can be expressed as $d_{m+1} - d_m = \lambda/2 = 0.279$ mm. Since the thickness of the Japanese coins shown in Fig. 6.6 is 1.5 mm, at least $1.5/0.279 \sim 5$–6 fringes are expected to appear around the coins. This simple estimation agrees with the experimental results. Note that the interference effect is unique for the monochromatic THz waves generated from the IJJ device, whose linewidth of approximately 0.5 GHz was separately obtained by a mixing technique [12].

6.3.2 Absorption experiment for liquid samples

The beautiful interference fringe patterns shown in Figs. 6.6, 6.7, and 6.8 encouraged us to construct a compact wavemeter to calibrate the wavelength of the THz waves. Actually, as demonstrated in Fig. 3.9, we have developed the interferometer system based on the wedge-shaped quartz cell and confirmed that the calibrated radiation frequency f is in good agreement with the value separately measured by using the FT-IR spectrometer.
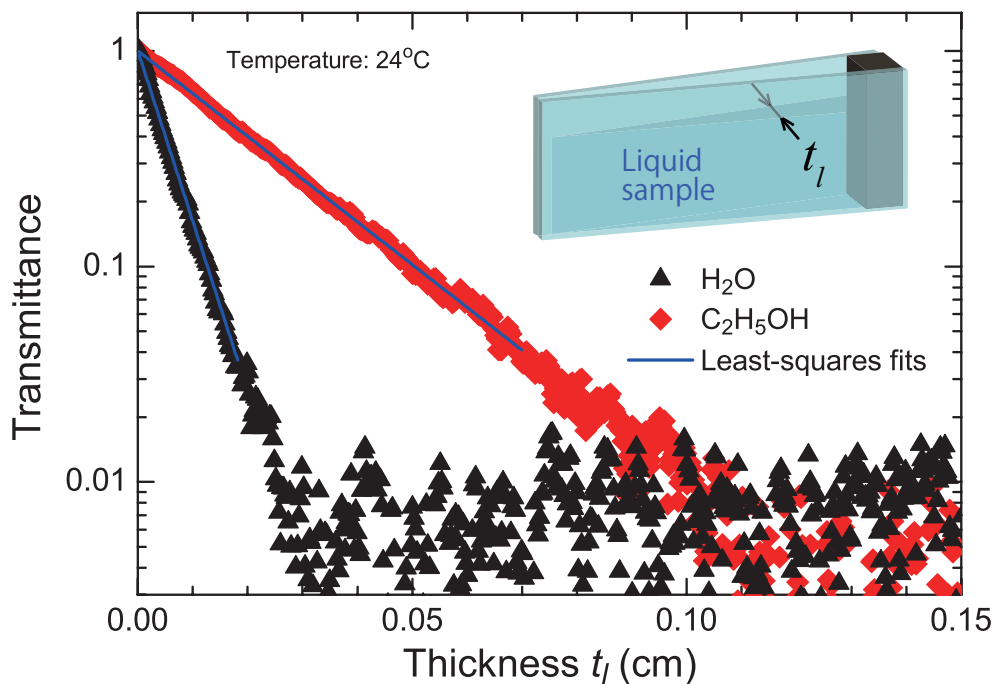

Figure 6.14: Transmittance of the THz wave passing through distilled water (H_2O) and 99.5% pure ethanol (C_2H_5OH) as a function of sample thickness t_l at $f = 0.618$ THz. Two solid lines indicate the theoretical fitting expressed as $e^{-\alpha_l \cdot t_l}$. Insets show the schematic view of the quartz cell containing the liquid sample.

A wedge-shaped quartz cell containing a liquid sample enables us to measure the absorption coefficient of polar liquids, *e.g.*, water solutions. The inset of Fig. 6.14 presents the schematic view of the quartz cell, while Fig. 6.14 shows the transmittance of the THz wave at $f = 0.618$ THz passing through the distilled water (H_2O) and 99.5% pure ethanol (C_2H_5OH) at room temperature of 24°C as a function of sample thickness t_l. Two solid lines in Fig. 6.14 are the best fit curves expressed as $\exp\{-\alpha_l \cdot t_l\}$, where $\alpha_l = 181.8\pm1.5$ cm^{-1} for H_2O and 45.7 ± 0.1 cm^{-1} for C_2H_5OH are the obtained absorption coefficients. In fact, as demonstrated in Fig. 6.14, these α_l-values were obtained with great accuracy ($R^2 \simeq 0.996$). Especially for H_2O, the α_l-value is in good agreement with $\alpha_l \sim 180$, which has been previously obtained by the THz time-domain reflection spectroscopy [144,145] and transmission measurements [146].

Although the large α_l-value above 100 cm^{-1} has made conventional transmission spectroscopy of liquid samples difficult due to the uncertainty of the sample thickness [144–146], our simple method using a wedge-shaped quartz cell provides a useful technique for measuring the α_l-value very precisely. The noticeable advantages of using our technique are as follows:

— Parameter-free measurement with simple absorption factor $\exp\{-\alpha_l \cdot t_l\}$, where t_l can be accurately calibrated by the known radiation frequency.

— High accuracy measurement with the large S/N ratio due to the high spectral intensity.

— High frequency resolution, which is actually determined by the linewidth of the THz wave, typically $\sim$0.5 GHz for the present IJJ device [12].

— Easy sample exchange, small amount of the liquid sample ($\leq$0.01 cc), and short measurement time (*e.g.*, a few seconds for one scan).

By measuring the absorption spectra of liquid water in the THz region, where quantum effects are negligible ($kT = 208$ cm^{-1}), it is possible to investigate the intermolecular interactions due to permanent and induced dipole moments in the hydrogen bonded network of water molecules [147]. Our technique can also be applied to many other practical applications, such as substance identification, microanalysis of impurities, in-situ observation of phase transitions, structure and dynamical analyses of large molecules, ions, and biological molecules in various solutions.

6.3.3   Absorption experiment for powder samples

We also performed the absorption experiment for various powder samples by using the transmission imaging system. Figures 6.15(a) and 6.15(b) present the THz and optical images of four different powder samples; salt (upper left), sugar (upper right), flour (lower left), and curry powder (lower right). A small amount of each powder was sprinkled on a thin quartz plate with thickness of 1 mm and fixed by using a 15×15-mm^2 double-sided tape. Then, the quartz plate was scanned in both X and Z directions at the speed of 32 mm/s by using the scan stage shown in Fig. 6.4. For the imaging, the radiation frequency of $f = 0.54$ THz was set by adjusting the input bias current as shown in Fig. 6.5. From the

transmission image shown in Fig. 6.15(a), we can calculate the effective absorptance A_p of each powder by subtracting the background absorptance of the quartz plate and the tape. Table 6.1 is a summary of A_p for eight powder samples. It is interesting to note that even commonly-available powders such as salt, sugar, and so on, have a wide variety of A_p almost independent of their visible colors. This variety of A_p may reflect the fact that the THz wave is sensitive to only the intermolecular vibrations or hydrogen bonds of the large molecule.

If we consider that W, ρ, and S denote the weight and density of the powder, and the area of the double-sided tape, respectively, the sample thickness t_p is given by $t_p = W/\rho S$. Then, the absorption coefficient of the powder α_p can be expressed as $\alpha_p = (-1/t_p)\ln(1 - A_p)$, because the transmittance $(1 - A_p)$ should be equal to $\exp\{-\alpha_p \cdot t_p\}$. Although we did not estimate the α_p-value for each powder in the present demonstration experiment, it may be reasonable to say that the α_p-value also has a wide range of values as A_p shown in Table 6.1.
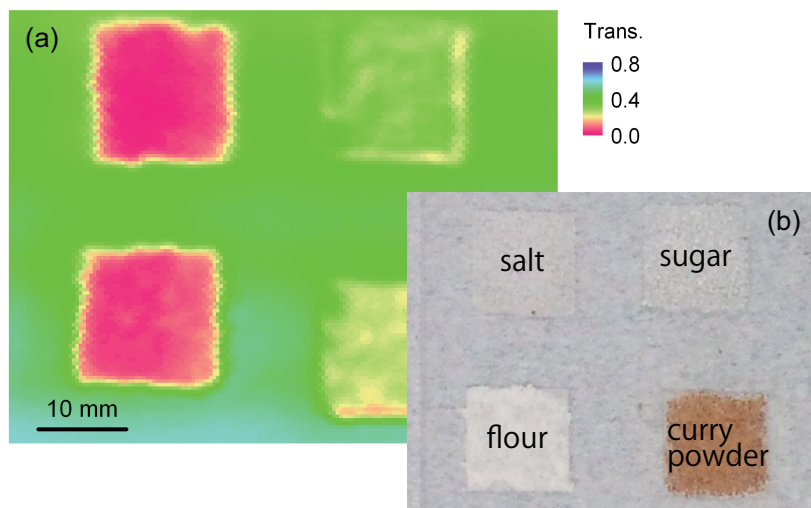

Figure 6.15: (a) THz and (b) optical images of four powder samples at $f = 0.54$ THz.

Table 6.1: Absorptance A_p of powder samples.

Powder	A_p (%)
Salt	82
Sugar	10
Pepper	72
Flour	82
Curry	41
Instant soup	< 1
Coffee	9
Stomach medicine	86

It is worthwhile mentioning that it takes only a few seconds to obtain one α_p-value, enabling us to use the present system for various applications. Furthermore, since the radiation frequency f is broadly tunable, we can even identify the substance of the powder sample from the spectroscopic measurement of $\alpha_p(f)$ [142]. Note that in the practical application, the environmental temperature and humidity have to be controlled, because the THz wave is easily absorbed by the atmospheric moisture.

6.4   Conclusion

We have demonstrated the THz imaging by using high-T_c superconducting THz source devices, which emit the continuous and monochromatic THz electromagnetic wave around 0.6 THz with the spectral linewidth of 0.5 GHz. As test examples, THz images of various objects were presented. Using a handmade interferometer quartz cell, we then investigated the interference patters to calibrate the radiation frequency. From a least-square analysis with a sinusoidal function, the radiation frequency was calculated with the relative accuracy of 0.1%. By injecting the distilled water and 99.5% pure ethanol into the quartz cell and measuring the sample thickness dependence of the transmittance of the THz wave, the absorption coefficients of liquids were simply measured. The estimated errors of the obtained coefficients are ≤0.8%. Also, we measured the absorptance of various powder samples. These demonstration experiments encourage us to make use of our imaging system for many other practical applications.

Chapter 7

Summary

The author's Ph.D. research on the intense, continuous, and coherent terahertz (THz) radiation from the high-temperature superconductor $Bi_2Sr_2CaCu_2O_{8+\delta}$ (Bi-2212) has been described in the preceding chapters. Entire experimental approaches to understanding the fundamental mechanism of this fascinating phenomenon have been performed by the author and many co-workers during the course of the Doctoral Program in the Graduate School of Pure and Applied Sciences at the University of Tsukuba, from April 2008 to March 2013. This interesting subject has been suddenly in the spotlight at the beginning of the author's graduate study, while a lot of meaningful suggestions concerning the Josephson radiation have been made for over thirty years since the first prediction of the Josephson effect in 1962. Here, the author does strongly emphasize the originality and significance of this subject because it has potential for further developments not only in the field of the superconducting technology but also in various fields of science and technology.

The summary for each chapter is in the following:

Chapter 2 This thesis started with the introduction of research backgrounds on THz radiation from a stack of intrinsic Josephson junctions in single crystalline Bi-2212 in Chapter 2. Both the Josephson effect and the cavity resonance effect important to generate the THz wave were described. Then, two recent topics of research on the frequency tunability and on the thermal non-equilibrium state were introduced.

Chapter 3 In Chapter 3, sample preparation techniques and the experimental setup were described. The focused ion beam milling technique is superior to other fabrication methods such as the photolithography technique in easily designing the geometrical mesa shape. In this study, we prepared more than ten mesa samples with different geometries and dimensions in order to investigate both the size and shape dependence of the radiation feature. The cross-sectional profile measured by the atomic force microscope is considerably slanted and rounded at the edges, resulting in a trapezoidal shape.

Chapter 4 In Chapter 4, we investigated the cavity resonance effect on the THz radiation
from the disk, square, and rectangular Bi-2212 mesas with changing the mesa sizes.
As expected from the microstrip antenna theory, the mesa-shape dependence of the
far-infrared radiation spectra clearly demonstrates that TM(1, 1) and TM(1, 0) cavity
modes are favorably excited for disk and rectangular mesas, respectively. More im-
portantly, the second harmonic radiation is clearly distinguishable from those of the
nearest higher-order cavity modes. We assumed that this higher harmonic radiation
arises from the non-linearity of the Josephson effect.

The higher-order cavity resonances were also clearly observed from a nearly-square
mesa by scanning the bias current at fixed bath temperature. This strongly suggests
that the primary mechanism of the radiation is nothing but the intrinsic Josephson
effect, because the obtained frequencies always satisfy the Josephson relation, even if
the radiation takes place at the off-cavity frequency due to the low cavity Q.

From the spatial radiation pattern measurement, we observed the anisotropic pattern
depending strongly on the excited TM mode. Then, we analyzed the data by using the
dual-source model and the geometrical theory of diffraction, which enables us to take
into account the influence of the Bi-2212 ground plane. In conclusion, it was revealed
that the radiation pattern can be considerably modified by the surrounding structure,
such as electrodes, evaporated metal layer, Bi-2212 ground plane, *etc.*, because of the
diffracted rays at their edges. Further studies using the mesa samples designed to
systematically investigate the influence of the Bi-2212 ground plane will provide more
detailed information about the diffraction effect.

Chapter 5 Since the atomic-scale intrinsic Josephson junctions are perfectly uniform, but
have a variety of coupling strengths depending on the compound, the stack of intrinsic
junctions is an exceptional system to investigate the non-linear dynamics of the lattice
motion. With this background, we investigated the THz radiation which takes place
in the inner region of the multiply-branched current-voltage characteristics in order to
study the non-linear phase dynamics of the intrinsic junction system in Chapter 5. To
determine whether the excitation of an internal cavity mode was an essential feature
to generate the THz wave, we examined the internal current-voltage characteristic
branches together with detecting the radiation. We found these internal branches
to radiate over a broad frequency range, and revealed that the obtained frequencies
exactly satisfy the Josephson relation. We then propose that a high-power THz source
device can be constructed by surrounding the mesa with an external, tunable high Q
electromagnetic cavity.

Chapter 6 In Chapter 6, we demonstrated the transmission THz imaging by using high-temperature superconducting THz source devices. As test examples, THz images of various objects were presented. Using a handmade interferometer quartz cell, we investigated the interference patterns to calibrate the radiation frequency. From a least-squares analysis with a sinusoidal function, the radiation frequency was calculated with a relative accuracy of 0.1%. By injecting distilled water and 99.5% pure ethanol into the quartz cell and measuring the sample thickness dependence of the transmittance, the absorption coefficients of liquids were measured with high accuracy. Also, we measured the absorptance of various powder samples. These demonstration experiments encourage us to make use of our imaging system for various applications.

Acknowledgments

Bibliography

[1] R. Kleiner, F. Steinmeyer, G. Kunkel, and P. Müller, Phys. Rev. Lett. **68**, 2394 (1992).

[2] R. Kleiner and P. Müller, Phys. Rev. B **49**, 1327 (1994).

[3] P. Müller, Adv. Solid State Phys. **34**, 1 (1995).

[4] A. A. Yurgens, Supercond. Sci. Technol. **13**, R85 (2000).

[5] L. Ozyuzer, A. E. Koshelev, C. Kurter, N. Gopalsami, Q. Li, M. Tachiki, K. Kadowaki, T. Yamamoto, H. Minami, H. Yamaguchi, T. Tachiki, K. E. Gray, W.-K. Kwok, and U. Welp, Science **318**, 1291 (2007).

[6] M. Tonouchi, Nat. Photonics **1**, 97 (2007).

[7] M. Tsujimoto, K. Yamaki, T. Yamamoto, H. Minami, and K. Kadowaki, Physica C **470**, S804 (2010).

[8] M. Tsujimoto, K. Yamaki, K. Deguchi, T. Yamamoto, T. Kashiwagi, H. Minami, M. Tachiki, K. Kadowaki, and R. A. Klemm, Phys. Rev. Lett **105**, 037005 (2010).

[9] M. Tsujimoto, T. Yamamoto, K. Delfanazari, R. Nakayama, T. Kitamura, M. Sawamura, T. Kashiwagi, H. Minami, M. Tachiki, K. Kadowaki, and R. A. Klemm, Phys. Rev. Lett. **108**, 107006 (2012).

[10] M. Tsujimoto, H. Minami, K. Delfanazari, M. Sawamura, R. Nakayama, T. Kitamura, T. Yamamoto, T. Kashiwagi, T. Hattori, and K. Kadowaki, J. Appl. Phys. **111**, 123111 (2012).

[11] M. Tsujimoto, T. Yamamoto, K. Delfanazari, R. Nakayama, N. Orita, T. Koike, K. Deguchi, T. Kashiwagi, H. Minami, and K. Kadowaki, J. Phys.: Conf. Ser. **400** 022127 (2012).

[12] T. Kashiwagi, M. Tsujimoto, T. Yamamoto, H. Minami, K. Yamaki, K. Delfanazari, K. Deguchi, N. Orita, T. Koike, R. Nakayama, T. Kitamura, M. Sawamura, S. Hagino, K. Ishida, K. Ivanović, H. Asai, M. Tachiki, R. A. Klemm, and K. Kadowaki, Jpn. J. Appl. Phys. **51**, 010113 (2012).

[13] H. Minami, M. Tsujimoto, T. Kashiwagi, T. Yamamoto, and K. Kadowaki, IEICE Trans. Electron. **95-C**, 347 (2012).

[14] K. Kadowaki, M. Tsujimoto, K. Yamaki, T. Yamamoto, T. Kashiwagi, H. Minami, M. Tachiki, and R. A. Klemm, J. Phys. Soc. Jpn. Lett. **79**, 023703 (2010).

[15] R. A. Klemm, E. R. LaBerge, D. R. Morley, T. Kashiwagi, M. Tsujimoto, and K. Kadowaki, J. Phys.: Condens. Matter **23**, 025701 (2011).

[16] K. Yamaki, M. Tsujimoto, T. Yamamoto, A. Furukawa, T. Kashiwagi, H. Minami, and K. Kadowaki, Opt. Express **19**, 3193 (2011).

[17] T. Kashiwagi, K. Yamaki, M. Tsujimoto, K. Deguchi, N. Orita, T. Koike, R. Nakayama, H. Minami, T. Yamamoto, R. A. Klemm, M. Tachiki, and K. Kadowaki, J. Phys. Soc. Jpn. **80**, 094709 (2011).

[18] K. Delfanazari, H. Asai, M. Tsujimoto, T. Kashiwagi, T. Kitamura, T. Yamamoto, M. Sawamura, K. Ishida, C. Watanabe, S. Sekimoto, H. Minami, M. Tachiki, R. A. Klemm, T. Hattori, and K. Kadowaki, Opt. Express **21**, 2171 (2013).

[19] B. D. Josephson, Phys. Lett. **1**, 251 (1962).

[20] A. K. Jain, K. K. Likhareva, J. E. Lukens, and J. E. Sauvageau, Phys. Rep. **109**, 309 (1984).

[21] M. Darula, T. Doderer, and S. Beuven, Supercond. Sci. Technol. **12**, R1 (1999).

[22] P. Barbara, A. B. Cawthorne, S. V. Shitov, and C. J. Lobb, Phys. Rev. Lett. **82**, 1963 (1999).

[23] T. Koyama and M. Tachiki, Solid State Commun. **96**, 367 (1995).

[24] M. Tachiki, M. Iizuka, K. Minami, S. Tejima, and H. Nakamura, Phys. Rev. B **71**, 134515 (2005).

[25] L. N. Bulaevskii, A. E. Koshelev, J. Supercond. Novel Magnetism **19**, 349 (2006).

[26] A. Irie, Y. Hirai, and G. Oya, Appl. Phys. Lett. **72**, 2159 (1998).

[27] V. M. Krasnov, N. Mros, A. Yurgens, and D. Winkler, Phys. Rev. B **59**, 8463 (1999).

[28] S. M. Kim, H. B. Wang, T. Hatano, S. Urayama, S. Kawakami, M. Nagao, Y. Takano, and T. Yamashita, Phys. Rev. B **72**, 140504 (2005).

[29] H. B. Wang, S. Urayama, S. M. Kim, S. Arisawa, T. Hatano, and B. Y. Zhu, Appl. Phys. Lett. **89**, 252506 (2006).

[30] K. Kadowaki, I. Kakeya, T. Yamamoto, T. Yamazaki, M. Kohri, Y. Kubo, Physica C **437-438**, 111 (2006).

[31] M.-H. Bae, H.-J. Lee, and J.-H. Choi, Phys. Rev. Lett. **98**, 027002 (2007).

[32] S. Madsen, G. Fillatrella, and N. F. Pedersen, Eur. Phys. J. B **40**, 209 (2004).

[33] I. E. Batov, X. Y. Jin, S. V. Shitov, Y. Koval, P. Müller,, and A. V. Ustinov, Appl. Phys. Lett. **88**, 262504 (2006).

[34] M. B. Gaifullin, M. Matsuda, N. Chikumoto, J. Shimoyama, and K. Kishio, Phys. Rev. Lett. **84**, 2945 (2000).

[35] M. Machida, T. Koyama, and M. Tachiki, Phys. Rev. Lett. **83**, 4618 (1999).

[36] K. Kadowaki, H. Yamaguchi, K. Kawamata, T. Yamamoto, H. Minami, I. Kakeya, U. Welp, L. Ozyuzer, A. Koshelev, C. Kurter, K. E. Gray, and W.-K. Kwok, Physica C **468**, 634 (2007).

[37] L. Ozyuzer, Y. Simsek, H. Koseoglu, F. Turkoglu, C. Kurter, U. Welp, A. E. Koshelev, K. E. Gray, W.-K. Kwok, T. Yamamoto, K. Kadowaki, Y. Koval, H. B. Wang, and P. Müller, Supercond. Sci. Technol. **22**, 114009 (2009).

[38] K. E. Gray, L. Ozyuzer, A. E. Koshelev, C. Kurter, K. Kadowaki, T. Yamamoto, H. Minami, H. Yamaguchi, M. Tachiki, W.-K. Kwok, and U. Welp, IEEE Trans. Appl. Supercond. **19**, 886 (2009).

[39] C. Kurter, K. E. Gray, J. F. Zasadzinski, L. Ozyuzer, A. E. Koshelev, Q. Li, T. Yamamoto, K. Kadowaki, W.-K. Kwok, M. Tachiki, and U. Welp, IEEE Trans. Appl. Supercond. **19**, 428 (2009).

[40] H. Minami, I. Kakeya, H. Yamaguchi, T. Yamamoto,, and K. Kadowaki, Appl. Phys. Lett. **95**, 232511 (2009).

[41] D. Oikawa, A. Irie, and K. Yamaki, IEEE Trans. Appl. Supercond. **23**, 1500604 (2013).

[42] L. N. Bulaevskii, and A. E. Koshelev, Phys. Rev. Lett. **99**, 057002 (2007).

[43] A. E. Koshelev, and L. N. Bulaevskii, Phys. Rev. B **77**, 014530 (2008).

[44] A. E. Koshelev, Phys. Rev. B **78**, 174509 (2008).

[45] S. Lin, X. Hu,, and M. Tachiki, Phys. Rev. B **77**, 014507 (2008)

[46] S. Lin, and X. Hu, Phys. Rev. Lett. **100**, 247006 (2008).

[47] X. Hu, and S. Lin, Phys. Rev. B **78**, 134510 (2008).

[48] Y. Nonomura, Phys. Rev. B **80**, 140506 (2009).

[49] X. Hu and S. Lin, Phys. Rev. B **80**, 064516 (2009).

[50] N. F. Pedersen, and S. Madsen, IEEE Trans. Appl. Supercond. **19**, 726 (2009).

[51] V. M. Krasnov, Phys. Rev. Lett. **103**, 227002 (2009).

[52] A. Grib and P. Seidel, Phys. Status Solidi (RRL) **3**, 302 (2009).

[53] M. Tachiki, S. Fukuya, and T. Koyama, Phys. Rev. Lett. **102**, 127002 (2009).

[54] T. Koyama, H. Matsumoto, M. Machida, and K. Kadowaki, Phys. Rev. B **79**, 104522 (2009).

[55] S. Lin and X. Hu, Phys. Rev. B **79**, 104507 (2009).

[56] A. L. Rakhmanov, S. E. Savel'ev, and Franco Nori, Phys. Rev. B **79**, 184504 (2009).

[57] X. Hu and S. Lin, Supercond. Sci. Technol. **23**, 053001 (2010).

[58] Y. Nonomura, J. Supercond. Nov. Magn. **23**, 601 (2010).

[59] R. A. Klemm and K. Kadowaki, J. Supercond. Nov. Magn. **23** 613 (2010).

[60] R. A. Klemm and K. Kadowaki, J. Phys.: Condens. Matter **22**, 375701 (2010).

[61] S. Savel'ev, V. A. Yampol'skii, A. L. Rakhmanov, and F. Nori, Rep. Prog. Phys. **73**, 026501 (2010).

[62] S. Lin and X. Hu, Phys. Rev. B **82**, 020504(R) (2010).

[63] S. Lin and X. Hu, J. Supercond. Nov. Magn. **23** 1025 (2010).

[64] A. E. Koshelev, Phys. Rev. B **82**, 174512 (2010).

[65] M. Tachiki, K. Ivanović, and K. Kadowaki, Phys. Rev. B **83**, 014508 (2011).

[66] V. M. Krasnov, Phys. Rev. B **83**, 174517 (2011).

[67] S. Lin and X. Hu, J. Nanosci. Nanotechno. **11**, 2916 (2011).

[68] H. Asai, M. Tachiki, and K. Kadowaki, Phys. Rev. B **85**, 064521 (2012).

[69] H. Asai, M. Tachiki, and K. Kadowaki, Appl. Phys. Lett. **101**, 112602 (2012).

[70] S. Lin and X. Hu, Phys. Rev. B **86**, 054506 (2012).

[71] H. Asai, M. Tachiki, and K. Kadowaki, Physica C, in press (2013), DOI: 10.1016/j.physc.2012.12.005.

[72] F. Liu, S. Lin, and X. Hu, Supercond. Sci. Technol. **26**, 025003 (2013).

[73] H. B. Wang, S. Guénon, B. Gross, J. Yuan, Z. G. Jiang, Y. Y. Zhong, M. Grünzweig, A. Iishi, P. H. Wu, T. Hatano, D. Koelle, and R. Kleiner, Phys. Rev. Lett. **105**, 057002 (2010).

[74] T. M. Benseman, A. E. Koshelev, K. E. Gray, W.-K. Kwok, and U. Welp, Phys. Rev. B **84**, 064523 (2011).

[75] T. Jacobs, S. Sridhar, Q. Li, G. D. Gu and N. Koshizuka, Phys. Rev. Lett. **75**, 4516 (1995).

[76] W. Anukool, S. Barakat, C. Panagopoulos, and J. R. Cooper, Phys. Rev. B **80**, 024516 (2009).

[77] H. Minami, N. Orita, T. Koike, T. Yamamoto, and K. Kadowaki, Physica C **470**, S822 (2010).

[78] H. B. Wang, S. Guénon, J. Yuan, A. Iishi, S. Arisawa, T. Hatano, T. Yamashita, D. Koelle, and R. Kleiner, Phys. Rev. Lett. **102**, 017006 (2009).

[79] W. J. Skocpol, M. R. Beasley, and M. Tinkham, J. Appl. Phys. **45**, 4054 (1974).

[80] R. Eichele, L. Freytag, H. Seifert, R. P. Huebener, and John R. Clem, J. of Low Temp. Phys. **52**, 449 (1983).

[81] D. Doenitz, R. Kleiner, D. Koelle, T. Scherer, and K. F. Schuster, Appl. Phys. Lett. **90**, 252512 (2007).

[82] S. Guénon, M. Grünzweig, B. Gross, J. Yuan, Z. G. Jiang, Y. Y. Zhong, M. Y. Li, A. Iishi, P. H. Wu, T. Hatano, R. G. Mints, E. Goldobin, D. Koelle, H. B. Wang, and R. Kleiner, Phys. Rev. B **82**, 214506 (2010).

[83] M. Li, J. Yuan, N. Kinev, J. Li, B. Gross, S. Guénon, A. Ishii, K. Hirata, T. Hatano, D. Koelle, R. Kleiner, V. P. Koshelets, H. Wang, and P. Wu, Phys. Rev. **86**, 060505 (2012).

[84] I. Kakeya, Y. Omukai, T. Yamamoto, K. Kadowaki, and M. Suzuki, Appl. Phys. Lett. **100**, 242603 (2012).

[85] H. Maeda, Y. Tanaka, M. Fukutomi, and T. Asano, Jpn. J. Appl. Phys. **27**, L209 (1988).

[86] M. J. V. Menken, A. J. M. Winkelmen, and A. A. Menovsky, J. Crystal Growth **113**, 9 (1991).

[87] T. Mochiku, and K. Kadowaki, Physica C **235-240**, 523 (1994).

[88] T. Watanabe, T. Fujii, and A. Matsuda, Phys. Rev. Lett. **79**, 2113 (1997).

[89] T. Yasuda, M. Tonouchi,, and S. Takano, Physica C **289**, 109 (1997).

[90] J. C. Fenton, P. J. Thomas, G. Yang, and C. E. Gough, Appl. Phys. Lett. **80**, 2535 (2002).

[91] N. Orita, H. Minami, T. Koike, T. Yamamoto, and K. Kadowaki, Physica C **470**, S786 (2010).

[92] S. Tajima, G. D. Gu, S. Miyamoto, A. Odagawa, and N. Koshizuka, Phys. Rev. B **48**, 16164 (1993).

[93] A. Yurgens, D. Winkler, N. V. Zavaritsky, and T. Claeson, Phys. Rev. B **53**, R8887 (1996).

[94] P. Vaudon, T. Aubreton, P. Dufrane, and B. Jecko, Ann. Télécommun. **48**, 319 (1993).

[95] R. G. Kouyoumjian and P. H. Pathak, Proc. IEEE **62**, 1448 (1974).

[96] D. E. McCumber, J. Appl. Phys. **39**, 2503 (1968).

[97] D. E. McCumber, J. Appl. Phys. **39**, 3113 (1968).

[98] W. C. Stewart, Appl. Phys. Lett. **12**, 277 (1968).

[99] W. J. Johnson, Ph.D. Thesis, University of Wisconsin (1968).

[100] P. W. Anderson, In *Lectures on the Manybody Problem*, Ravello 1963 (E. R. Caiamiello, Ed.). Vol. 2, Academic, pp.113 (1964).

[101] T. A. Fulton and R. C. Dynes, Solid State Comm. **12**, 57 (1973).

[102] N. F. Pedersen, J. Mygind, O. H. Søerensen, and B. Dueholm, LT 15, 1232 (1978).

[103] A. Barone and G. Paternò, *Physics and Applications of the Josephson Effect*, John Wiley & Sons, Inc., New York, U.S.A. (1982).

[104] K. K. Likharer, *Dynamics of Josephson Junctions and Circuits*, Gordon and Breach Science Pub., Philadelphia (1986).

[105] L. Solymar, *Superconductive Tunnelling and Applications*, Chapman and Hall LTD., London (1972).

[106] T. Van Duzer and C. W. Turner, *Principles of Superconductive Devices and Circuits (2nd Edition)*, Prentice Hall PTR (1998).

[107] S. Sakai, P. Bodin, and N. F. Pedersen, J. Appl. Phys. **73**, 2411 (1993).

[108] T. Koyama, and M. Tachiki, Phys. Rev. B **54**, 16183 (1996).

[109] T. Koyama, J. Phys. Soc. Jpn. **68**, 3062 (1999).

[110] Y. Machida, T. Koyama, and M. Tachiki, Physica C **300**, 55 (1998).

[111] M. Tachiki, T. Koyama, and S. Takahashi, Phys. Rev. B **50**, 7065 (1994).

[112] Y. Matsuda, M. B. Gaifullin, K. Kumagai, K. Kadowaki,, and T. Mochiku, Phys. Rev. Lett. **75**, 4512 (1995).

[113] I. Kakeya, K. Kindo, K. Kadowaki, S. Takahashi, and T. Mochiku, Phys. Rev. B **57**, 3108 (1998).

[114] Y. Uematsu, K. Nakajima, T. Yamashita, I. Tanaka,, and H. Kojima, Appl. Phys. Lett. **73**, 2820 (1998).

[115] Y. Uematsua, N. Sasaki, Y. Mizugaki, K. Nakajima, T. Yamashita, S. Watauchi, and I. Tanaka, Physica C **362**, 290 (2001).

[116] M. Machida and T. Koyama, Phys. Rev. B **70**, 024523 (2004).

[117] Ch. Helm, Phys. Rev. Lett. **89**, 057003 (2002).

[118] S. Takeno and M. Peyard, Physica D **92**, 140 (1996).

[119] S. Watanabe, H. Zant, S. Strogatz, and T. Orlando, Physica D **97**, 429 (1996).

[120] J. Faist, F. Capasso, D. L. Sivco, C. Sirtori, A. L. Hutchinson, and A. Y. Cho, Science **264,** 553 (1994).

[121] R. Köhler, A. Tredicucci, F. Beltram, H. E. Beere, E. H. Linfield, A. G. Davies, D. A. Ritchie, R. C. Iotti, and F. Rossi, Nature **417**, 156 (2002).

[122] G. Scalari, C. Walther, J. Faist, H. Beere, and D. Ritchie, Appl. Phys. Lett. **88**, 141102 (2006).

[123] S. Kumar, C. W. I. Chan, Q. Hu and J. L. Reno, Nature Phys. **7**, 166 (2011).

[124] H. Ito, F. Nakajima, T. Furuta, and T. Ishibashi, Semicond. Sci. Technol. **20,** S191 (2005).

[125] O. V. Kibis, M. R. da Costa, and M. E. Portnoi, Nano Lett. **7,** 3414 (2007).

[126] N. L. Rangel and J. M. Seminario, J. Phys. Chem. A **112,** 13699 (2008).

[127] E. R. Brown, J. R. Söderström, C. D. Parker, L. J. Mahoney, K. M. Molvar, and T. C. McGill, Appl. Phys. Lett. **58,** 2291 (1991).

[128] M. Reddy, S. C. Martin, A. C. Molnar, R. E. Muller, R. P. Smith, P. H. Siegel, M. J. Mondry, M. J. W. Rodwell, H. Kroemer, and S. J. Allen, Jr., IEEE Electron Device Lett. **18** 218 (1997).

[129] M. Asada, S. Suzuki, and N. Kishimoto, Jpn. J. Appl. Phys. **47** 4375 (2008).

[130] S. Suzuki, M. Asada, A. Teranishi, H. Sugiyama, and H. Yokoyama, Appl. Phys. Lett. **97** 242102 (2010).

[131] M. Shiraishi, H. Shibayama, K. Ishigaki, S. Suzuki, M. Asada, H. Sugiyama, and H. Yokoyama, Appl. Phys. Express **4** 064101 (2011).

[132] K. Kawase, Optics and Photonics News Oct. p.38 (2004).

[133] P. R. Smith, D. H. Auston, and M. C. Nuss, IEEE J. Quantum Electron. **24**, 255 (1988).

[134] D. Grischkowsky, S. Keiding, M. van. Exter, and C. Fattinger, J. Opt. Soc. Am. B **7**, 2006 (1990).

[135] M. C. Nuss, P. M. Mankiewich, M. L. O'Malley, E. H. Westerwick, and P. B. Littlewood, Phys. Rev. Lett. **66**, 3305 (1991).

[136] J. E. Pedersen and S. Keiding, IEEE J. Quantum Electron. **28**, 2518 (1992).

[137] H. Harde and D. Grischkowsky, J. Opt. Soc. Am. B **8**, 1642 (1991).

[138] M. van. Exter and D. Grischkowsky, IEEE Microwave Theory Technol. **38**, 1684 (1990).

[139] M. C. Nuss, K. W. Goossen, J. P. Gordon, P. M. Mankiewich, M. L. O'Malley, and M. Bhushan, J. Appl. Phys. **70**, 2238 (1991).

[140] A. Dobroiu, M. Yamashita, Y. N. Ohshima, Y. Morita, C. Otani, and K. Kawase, Appl. Opt. **43**, 5637 (2004).

[141] K. Kawase, J. Shikata, and H. Ito, J. Phys. D: Appl. Phys. **35**, R1 (2002).

[142] K. Kawase, Y. Ogawa, and Y. Watanabe, Opt. Express **11**, 2549 (2003).

[143] Y. Watanabe, K. Kawase, T. Ikari, H. Ito, Y. Ishikawa, and H. Minamide, Appl. Phys. Lett **83**, 800 (2003).

[144] C. Rønne, L. Thrane, P-O. Åstrand, A. Wallqvist, K. V. Mikkelsen, and S. R. Keiding, J. Chem. Phys. **107**, 5319 (1997).

[145] U. Møller, D. G. Cooke, K. Tanaka, and P. U. Jepsen, J. Opt. Soc. Am. B **26**, A113 (2009).

[146] J. T. Kindt and C. A. Schmuttenmaer, J. Phys. Chem. **100**, 10373 (1996).

[147] A. Luzar and D. Chandler, Nature **379**, 55 (1996).

ver.130226